THE UNIVERSITY of ADELAIDE

Development of High-Performance Cathodic Catalysts for Non-Aqueous Lithium-Oxygen Batteries

Qi Bi

A thesis submitted for the degree of Doctor of Philosophy

School of Chemical Engineering and Advanced Materials

The University of Adelaide

April 2020

Table of Contents

Abstract

Lithium-oxygen (Li-O_2) batteries have attracted intensive attention in last decade, due to its high theoretical energy densities and environmental benignity that satisfy the need for large energy storage systems including electric vehicles. However, they are still in their infancy and several challenges remain to be addressed immediately. In addition to the degradation of anode and electrolyte, one of the biggest challenges is the structure and catalytic design for oxygen electrode to achieve high capacity and long cycle life.

In this thesis, size-controlled polystyrene (PS) spheres were introduced to a polydopamine derived N-doped reduced graphene (N-rGO) to explore the impact of the pore size of carbon oxygen electrodes to the performance of Li-O_2 batteries. The battery containing N-rGO with 170 nm pores revealed a high specific capacity of 16777 mA h g^{-1}, which is one of the highest among the reported carbon-based Li-O_2 batteries. Field emission scanning electron microscope (FESEM) of cathode morphologies before and after discharge/charge showed that the N-rGO with 170 nm pores could hold most discharge products at a cut-off capacity of 1000 mA h g^{-1} without deformation to achieve a long stable cycle life.

Furthermore, cobalt sulfides with controlled phases being synthesized via thermal decomposition of $Co(TU)_4(NO_3)_2$ were studied as the bi-functional catalysts towards both ORR and OER of Li-O_2 batteries in order to improve specific capacity and cycling life. A dual-phase cobalt sulfide prepared at 900 °C (CoS-900) contains both Co_9S_8 and CoS exhibited excellent ORR and OER catalytic activities with a low overvoltage (1.25 V) for Li-O_2 batteries. The designated CoS-900@NG cathode achieved large discharge capacity at 7410 mA h g^{-1} with 100% charge capacity recovery as well as a super long cycle life at 108 cycles for Li-O_2 battery. The excellent Li-O_2 batteries performance can be attributed to the generation of both crystalline and amorphous film-like Li_2O_2 that effectively improve ORR/OER kinetics of Li-O_2 batteries.

Finally, Co_9S_8 nanoparticles were anchored to N, S co-doped graphene to form leave-like Co_9S_8/N, S-GO composites through hydrothermal treatment. The composite was further

optimized by adjusting cobalt sulfide precursor amount to achieve an improvement of battery performance. As a result, the Li-O_2 battery with Co_9S_8/N, S-GO composite can achieve a 100 % recoverable high discharge capacity at 4884 mA h g^{-1} and a stable cycle life.

The thesis systematically explored the relationship between the structures of oxygen electrode and electrochemical performance of Li-O_2 batteries, including surface structure, heteroatom doping and cobalt sulphide hybridization. The outcomes provide new perspectives for the future development of high-performance Li-O_2 batteries by strategically designing ORR/OER catalysts.

Thesis Declaration

I certify that this work contains no material which has been accepted for the award of any other degree or diploma in my name, in any university or other tertiary institution and, to the best of my knowledge and belief, contains no material previously published or written by another person, except where due reference has been made in the text. In addition, I certify that no part of this work will, in the future, be used in a submission in my name, for any other degree or diploma in any university or other tertiary institution without the prior approval of the University of Adelaide and where applicable, any partner institution responsible for the joint-award of this degree.

I acknowledge that copyright of published works contained within this thesis resides with the copyright holder(s) of those works.

I also give permission for the digital version of my thesis to be made available on the web, via the University's digital research repository, the Library Search and also through web search engines, unless permission has been granted by the University to restrict access for a period of time.

I acknowledge the support I have received for my research through the provision of an Australian Government Research Training Program Scholarship.

Qi Bi

24/10/2019

Acknowledgements

I would fist like to extend my utmost gratitude to my principle supervisor, Professor Sheng Dai for his guidance and help throughout my Ph.D. candidature. My gratitude also goes to my co-supervisors Professor Haihui Wang and Professor Shizhang Qiao for their support when my principle supervisor was away. This thesis could not have completed without them.

I would like to thank Hongbin Chen and Dr Guoxue Liu for their help on the fabrication of Li-O_2 batteries, Professor Gunther Andersson and Dr Yanting Yin for their help on the evaluation of XPS, Dr Konggang Qu for his suggestions on N-doped graphene, Professor Lei Zhang, Dr Dongdong Li, and Dr Heng Wang for their advice on the research. This work was a very new area for me, and without their help, the research in this area would have never been pursued.

I would also express my gratefulness towards my colleagues in the University of Adelaide for their continuous help throughout my candidature. They are Dr Aabhash Shrestha, Dr Yusak Hartanto, Dr Xiaolin Cui, Hesamoddin Rabiee, Xuesi Wang, Wanxia, Zhao, BingYang Zhang, Dr Seonho Yun, Yongqiang Zhao, Dr Qiuhong Hu, Jason Peak, Dr Diana Tran, Dr Yao Zheng, Dr Yan Jiao, and Ken Neubauer, Dr Ashley Slattery, Lyn Waterhouse from Adelaide Microscopy. In addition, I would like to thank Professor Haihui Wang's group at South China University of Technology for their assistance for my research.

My appreciation goes to my friends, I could not have been through the darkness without the company from you.

My special thanks go to my dearest aunty Manli Huang for giving me a home at Melbourne, where I can always fly to when I need support from family.

Finally, I give my sincerest thankfulness to my beloved parents, you are the reason for who I am. I love you.

Chapter 1 Introduction

1.1 Background

With the consumption of fossil fuels, energy and environmental problems are among the most important concerns in the 21st century. To eliminate the release of a large quantity of CO_2 and other greenhouse gases (GHG) during the combustion of fossil fuels, sustainable energy generated from natural resources, such as solar or wind is increasing demanded globally. However, such sustainable energy is fluctuant and not as steady as fossil fuels due to weather conditions. In addition, along with the expanding market of electrification of transportation, large-scale energy storage devices that can counterbalance the variability of sustainable energy as well as provide enough power to electric vehicles (EVs) are attracting extensive interests than at any time in the past.

Traditionally rechargeable lithium-ion batteries (LIBs) are widely used for energy storage because of their long-cycling life (> 5000 cycles) and high-energy efficiency (> 90%) [1]. However, the current energy density of LIB is calculated to be between 100 – 200 W h kg^{-1} which is hard to meet the needs for renewable energy and EVs [1]. Various alternatives such as Li-O_2, Li-S, Mg-air and Al-air batteries have been intensively studied as the next generation storage systems over the past 10 years. Among them, Li-O_2 batteries give the highest theoretical mass energy density at 3582 W h kg^{-1} (aqueous electrolytes), and 3505 W h kg^{-1} (non-aqueous electrolytes) [2]. While still under research and development, Li-O_2 batteries have the potential to enable an electronic car to achieve a driving distance for more than 550 km in one charge with the cost less than 150 US$ kW h^{-1}. The driving distance is around 3 times more than that of current electric car powered by LIBs [3].

1.2 Aim and Objectives

Despite the excellent theoretical performance, the implementation of Li-O_2 batteries are still hindered by their low energy efficiency, poor cycling retention, and safety concerns with the

use of metallic Li-metal anode. In a typical non-aqueous Li-O_2 battery, Li_2O_2 is formed through the oxygen reduction reaction (ORR) process and deposited on the cathode during discharge, and Li_2O_2 decomposed into lithium ion and oxygen through the oxygen evolution reaction (OER) during charge [4-7]. It has been found that the generation of unwanted by-products and the accumulation of dissolvable discharge products are the major reasons to cause seriously decay of electrochemical performance by hindering the reversible redox reaction (ORR/OER) [4]. As both ORR and OER take place on the oxygen cathode of Li-O_2 batteries, the development of electrocatalytic cathode materials that facilitate ORR/OER process with limit by-products formation is crucial to improve the performance of Li-O_2 batteries. The efficiency of ORR/OER are found to be associated with various factors including surface structures, heteroatom doping and hybridization of electrochemical catalysts. Though these factors are interrelated and interplayed, the catalyst structure mainly limits the O_2 diffusion and the storage of discharge products on oxygen electrode, while the heteroatom doping and hybridization determines the oxygen redox kinetics associated with ORR/OER reactions [8].

This work focuses on exploring stable bi-functional electrocatalytically oxygen electrodes towards ORR and OER to produce high-performance non-aqueous Li-O_2 batteries. In order to achieve the aim, the following objectives are covered in this thesis:

1. Investigate the relationship between N-rGO porous structures and electrocatalytic performance of cathode materials in Li-O_2 batteries.
2. Explore efficient bi-functional catalysts towards both ORR and OER in Li-O_2 batteries to improve performance in specific capacity and cycling life.
3. Improve Li-O_2 battery performance by introducing novel composite cathode materials containing carbon materials and bi-functional catalysts.

1.3 Outlines of Thesis

Chapter 1 is an introduction including background, aim and objectives of the thesis.

Chapter 2 is a literature review about the design and mechanism of Li-O_2 batteries together with a summary of previous studies of graphene and cobalt sulfides as oxygen electrodes for Li-O_2 batteries.

Chapter 3 presents a poly-dopamine derived N-rGO as cathode materials for Li-O_2 batteries, and then further explores the relationships between porous structures and electrocatalytic performance for Li-O_2 batteries.

Chapter 4 describes the approach to prepare cobalt sulfides with different phases by simply tuning the decomposition temperature of cobalt thiourea complex. Single phase and dual-phase cobalt sulfides are physically mixed with N-rGO and employed as cathode materials for Li-O_2 batteries. It explores the effect of cobalt sulfides on battery performance by changing the morphologies of discharge products.

Chapter 5, Co_9S_8 nanoparticles were anchored to N, S co-doped graphene to form leave-like Co_9S_8/N, S-GO composites through hydrothermal treatment. The composites were further optimized by adjusting cobalt sulfide precursor amounts and employed as cathode materials for Li-O_2 batteries to explore the electrocatalytic performance of Co_9S_8/N, S-GO composites for Li-O_2 batteries.

Finally, Chapter 6 summarises the thesis and highlights main contributions. Future research work is recommended.

References

1. Wang, Z. L.; Xu, D.; Xu, J. J.; Zhang, X. B., Oxygen electrocatalysts in metal-air batteries: from aqueous to nonaqueous electrolytes. *Chem. Soc. Rev.* **2014,** *43* (22), 7746-7786.
2. Kim, H.; Jeong, G.; Kim, Y. U.; Kim, J. H.; Park, C. M.; Sohn, H. J., Metallic anodes for next generation secondary batteries. *Chem. Soc. Rev.* **2013,** *42* (23), 9011-9034.
3. Bruce, P. G.; Freunberger, S. A.; Hardwick, L. J.; Tarascon, J. M., Li-O-2 and Li-S batteries with high energy storage. *Nature Materials* **2012,** *11* (1), 19-29.

4. Xu, Y. F.; Chen, Y.; Xu, G. L.; Zhang, X. R.; Chen, Z. H.; Li, J. T.; Huang, L.; Amine, K.; Sun, S. G., RuO2 nanoparticles supported on MnO2 nanorods as high efficient bifunctional electrocatalyst of lithium-oxygen battery. *Nano Energy* **2016,** *28*, 63-70.

5. Black, R.; Adams, B.; Nazar, L. F., Non-Aqueous and Hybrid Li-O2 Batteries. *Advanced Energy Materials* **2012,** *2* (7), 801-815.

6. Feng, N. N.; He, P.; Zhou, H. S., Critical Challenges in Rechargeable Aprotic Li-O-2 Batteries. *Advanced Energy Materials* **2016,** *6* (9).

7. Lim, H. D.; Lee, B.; Bae, Y.; Park, H.; Ko, Y.; Kim, H.; Kim, J.; Kang, K., Reaction chemistry in rechargeable Li-O-2 batteries. *Chem. Soc. Rev.* **2017,** *46* (10), 2873-2888.

8. Lin, X.; Yuan, R.; Cai, S.; Jiang, Y.; Lei, J.; Liu, S.-G.; Wu, Q.-H.; Liao, H.-G.; Zheng, M.; Dong, Q., An Open-Structured Matrix as Oxygen Cathode with High Catalytic Activity and Large Li2O2 Accommodations for Lithium–Oxygen Batteries. *Advanced Energy Materials* **2018,** *8* (18), 1800089.

Chapter 2 Literature Review

2.1 Lithium-oxygen Batteries

Littauer and Tsai first introduced the concept of lithium-oxygen ($Li-O_2$) battery in 1974 with an aqueous alkaline solution as electrolyte [2]. Currently, four types of $Li-O_2$ batteries have been developed based on the electrolytes that are used: non-aqueous (aprotic), aqueous, solid-state, and hybrid aqueous/aprotic $Li-O_2$ batteries (Figure 2.1) [3]. For all these $Li-O_2$ batteries, Li metal is used as the anodes to provide lithium source, oxygen is obtained from the air through an open system to act as active material of the cathodes (oxygen electrodes) [3]. In aqueous and hybrid aqueous/aprotic $Li-O_2$ systems, a protective membrane for Li metal is required to prevent the reaction of Li and water. For non-aqueous and solid-state $Li-O_2$ systems, the performance of batteries is mostly determined by the cathode (catalysts), and electrolyte [4]. This thesis will focus on the development of non-aqueous $Li-O_2$ batteries.

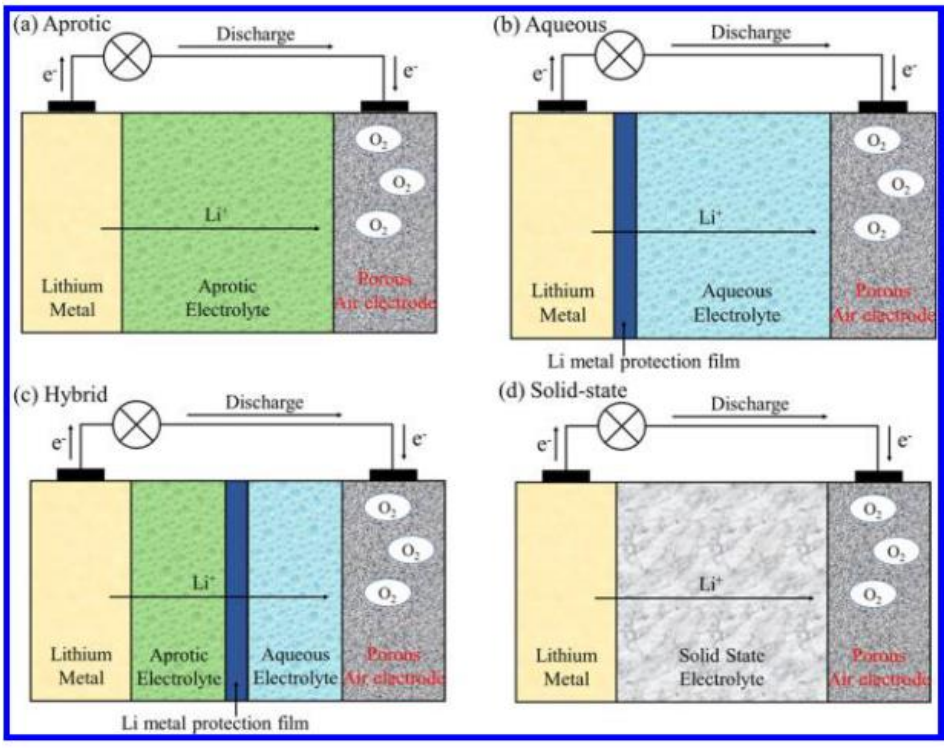

Figure 2.1. Schematic representations of (a) aprotic, (b) aqueous, (c) hybrid, and (d) solid-state $Li-O_2$ batteries. Reprinted from [3].

2.1.1 Mechanism of Li-O_2 Batteries

The high energy density non-aqueous Li-O_2 batteries is operated based on a simple reaction between oxygen and lithium ions [5 6], as shown in Reaction 2.1

$$2Li^+ + O_2 + 2e^- \leftrightarrow Li_2O_2 \quad (2.1)$$

The performance of Li-O_2 batteries is influenced by many factors including structure of catalysts, electrolyte stability, and the electrode degradation. These factors occur in conjunction with the basic mechanism of Li-O_2 batteries that described by Reaction 2.1. Previous studies show that even slightly changes in catalysts, electrolytes, or material structure of oxygen electrode can result in great differences of battery performance [7-8]. The following sections will discuss about the mechanism of Li-O_2 batteries from the discharge and charge processes, respectively.

2.1.1.1 Reaction chemistry on discharge

During an ideal discharge process, Li ion reacts with O_2 dissolved in electrolytes to form Li_2O_2 at the oxygen electrode (cathode). This process is referred as oxygen reduction reaction (ORR), described as following reactions:

$$O_2\,(g) + Li^+ + e^- \rightarrow LiO_2 \quad (2.2)$$

$$2LiO_2 \rightarrow Li_2O_2\,(s) + O_2 \quad (2.3)$$

$$LiO_2 + Li^+ + e^- \rightarrow Li_2O_2\,(s) \quad (2.4)$$

At the beginning, oxygen is reduced on the electrode and combines with Li ion dissolved in electrolyte to from LiO_2. Then, LiO_2 may undergo two different pathways to form Li_2O_2: either through a disproportionation reaction due to the instability of LiO_2 (Reaction 2.3), or another one electron transfer electrochemical process (Reaction 2.4). The crystalline discharge product Li_2O_2 is generated from a solution process when disproportionation reaction happens; while the Li_2O_2 film is grown on the oxygen electrode when one electron transfer electrochemical process occurs. The solubility of the LiO_2 intermediate is the key factor to determine the pathways to

form Li_2O_2 in Li-O_2 batteries. LiO_2 can dissolve in high donate number (DN) solvent, such as 1-methylimidazole and dimethyl sulfoxide to from crystalline Li_2O_2 through disproportionation reactions. On the other hand, LiO_2 is presented primarily on the electrode surface in a low DN solvent electrolyte, where one electron transfer electrochemical reaction occurs, depositing a thin layer of Li_2O_2 on electrode.

The formation of LiO_2 is unfavorable for Li-O_2 system, especially in its solubilized form, where O_2^- acts as a highly reactive oxygen radical that reacts with electrolyte to cause parasitic reactions. As a strong nucleophile, O_2^- is prone to attack electron-deficient part of electrolyte to form [solvent-O_2]$^-$complex (nucleophilic attack) and yield byproducts such as Li_2CO_3, LiOH, and HCO_2Li instead of Li_2O_2 (approach 1 in Figure 2.2). Carbonate based electrolytes including ethylene carbonate, propylene carbonate, and dimethyl carbonate are found to be vulnerable to nucleophilic attack and therefore are excluded from the Li-O_2 electrolyte candidates. In contrast, non-carbonate-based electrolytes such as ether-, sulfone-, and amide-based solvents possess high [solvent-O_2]$^-$complex formation energy and reaction barrier can counterwork with nucleophilic attack to produce Li_2O_2 as discharge product (approach 2 in Figure 2.2). However, O_2^- ables to further degrade these non-carbon-based electrolytes by H-abstraction to form unwanted byproducts (approach 3 in Figure 2.2).

Recent research indicates that additives in the electrolyte influence the discharge mechanism of Li-O_2 batteries by impacting the LiO_2 solubility. For example, water, as a strong Lewis acid, can facilitate the dissolution of LiO_2 in the electrolyte, which sequentially promotes the disproportionation reaction [9-10]. Therefore, the particle size of Li_2O_2 grows as the increase of H_2O content in electrolytes, and discharge capacity of Li-O_2 can be accordingly improved. However, exceed amount of water in the electrolyte leads to a formation of LiOH, which decays the ORR performance of Li-O_2 cells [11-13]. Similarly, other additives such as methanol and perchloric acid can change the pathway of Li_2O_2 formation by altering the solubility of LiO_2 [9-10].

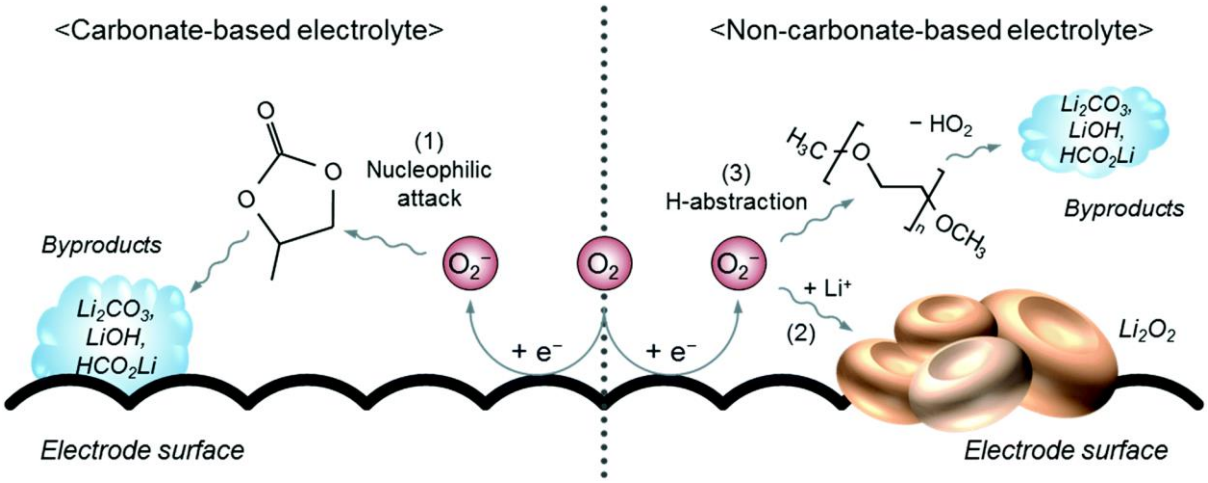

Figure 2.2. Schematic of discharge reactions involving oxygen radicals in different electrolyte systems. Reproduced from reference [1] by permission of The Royal Society of Chemistry.

The poor electrical conductivity of discharge product Li_2O_2 is another important challenge for non-aqueous Li-O_2 batteries, which leads to electrical passivation of cathode and a high discharge/charge overpotential. The most observed morphology of Li_2O_2 are discs/toroid, spheres, red-blood-cell like particles, and layered flakes, as shown in Figure 2.3. Apart from the impacts of solubility of LiO_2, the differences of morphology are largely depending on the discharging current rate and the oxygen affinity of the catalysts [14-16]. The catalysts on cathode have the potential to stabilize discharge intermediate because of their preferential affinity for O_2 and LiO_2, which can delay the liberation of LiO_2 into electrolyte, and accordingly promote LiO_2 to take additional electrons from electrode to from Li_2O_2 [17]. Meanwhile, the introduction of catalysts can change the reaction mechanism in Li-O_2 system. It is suggested that Ir-decorated reduced graphene oxide can offer a platform for stable growth of needle-like LiO_2 as final discharge product on the oxygen electrode of Li-O_2 batteries without further disproportioning to film-like Li_2O_2 [5]. Soluble catalysts, also called as redox mediator, can facilitate the electron transfer between the electrode and oxygen in the electrolyte during discharge, as described in the reactions below [18-19].

$$2(\text{ORR mediator}) + 2e^- \rightarrow 2(\text{ORR mediator})^- \quad (2.5)$$

$$2(\text{ORR mediator})^- + Li^+ + O_2 \rightarrow 2(\text{ORR mediator}) + Li_2O_2 \quad (2.6)$$

The introduction of soluble catalysts with higher reduction potential than that of O_2/O_2^- couple can upshift the discharge voltage. The reduction of ORR mediator happens before the oxygen reduction process occurs (Reaction 2.5) and then transfers an electron to Li^+ and oxygen to form Li_2O_2 (Reaction 2.6).

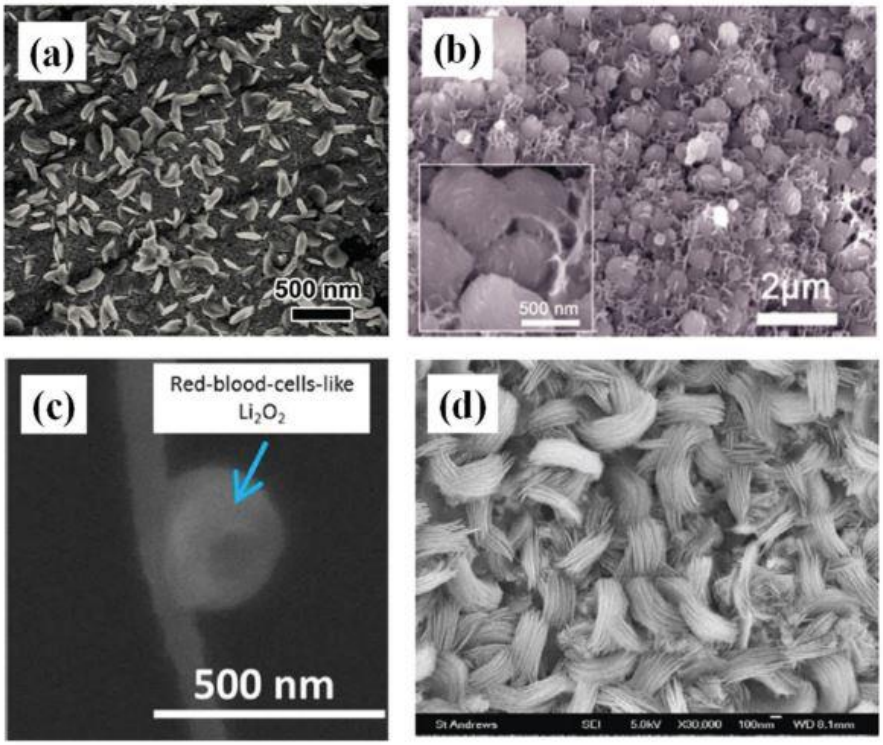

Figure 2.3. SEM images of various morphologies of Li_2O_2 formed on different cathode systems. (a) discs/toroids; (b) spherical; (c) red-blood cell like; (d) layered flake Li_2O_2. Reproduced from reference [20] with permission from WILEY (Copyright 2016 WILEY-VCH Verlag GmbH & Co. KGaA, Weinheim).

Apart from the parameters mentioned above, several kinetic issues can affect the mechanistic chemistry of Li-O_2 batteries, including discharge current rate, oxygen diffusivity and solubility. The discharge current rate influences the morphology of Li_2O_2, specifically, crystalline Li_2O_2 generates at low discharge rates and Li_2O_2 film produced at high discharge rates as high current rates accelerate the seed nucleation of Li_2O_2 on oxygen electrode surface, where Reaction 2.4 dominant the ORR process. In that case, surface precipitated Li_2O_2 were formed on the electrode as films to block the interaction between electrode and electrolyte, causing a low

discharge capacity. In contrast, disproportionation Reaction 2.3 is more favorable to occur when low current rate is applied, thus delivers a relative high discharge capacity of Li-O_2 batteries [14, 21-22]. Meanwhile, the oxygen diffusivity and solubility can be enhanced by using catalysts, increasing Li salt concentration in electrolyte, and selecting electrolyte with low DN solvents [23].

2.1.1.2 Reaction chemistry on charge

During an ideal charge, Li_2O_2 decomposes into lithium ion and oxygen following the reverse process of Reaction 2.1, which is called oxygen evolution reaction (OER). However, in a realistic practice, the charge mechanism can be complicated due to the morphology of Li_2O_2 and discharge byproducts from parasitic reactions.

Three decomposition pathways of Li_2O_2 have been observed. The primary decomposition occurs at the interface between the electrode and film-like Li_2O_2, as demonstrates in the green box of Figure 2.4a. The decomposition of Li_2O_2 film on the oxygen electrode creates voids at the interface, and then filled by the collapse of Li_2O_2 particles till the full decomposition [24]. Meanwhile, the decomposition also happens at the interface between Li_2O_2 and electrolyte, where crystalline Li_2O_2 releases lithium ion and oxygen, as shown in the blue box in Figure 2.4a [25]. However, the decomposition of large crystalline Li_2O_2 particles is difficult due to the slow charge transfer caused by the low conductivity of Li_2O_2 [26-28], which results in a high charge overpotential [29-30]. At last, electrochemical decomposition of byproducts including LiO_2 and Li^+ mainly takes place at the electrode/electrolyte interface (red box in Figure 2.4a), though the process is rarely dominant [31]. It is expected that three types of decomposition reactions may happen at the same time during charge, the dominant reaction can be determined by the nature of discharge products.

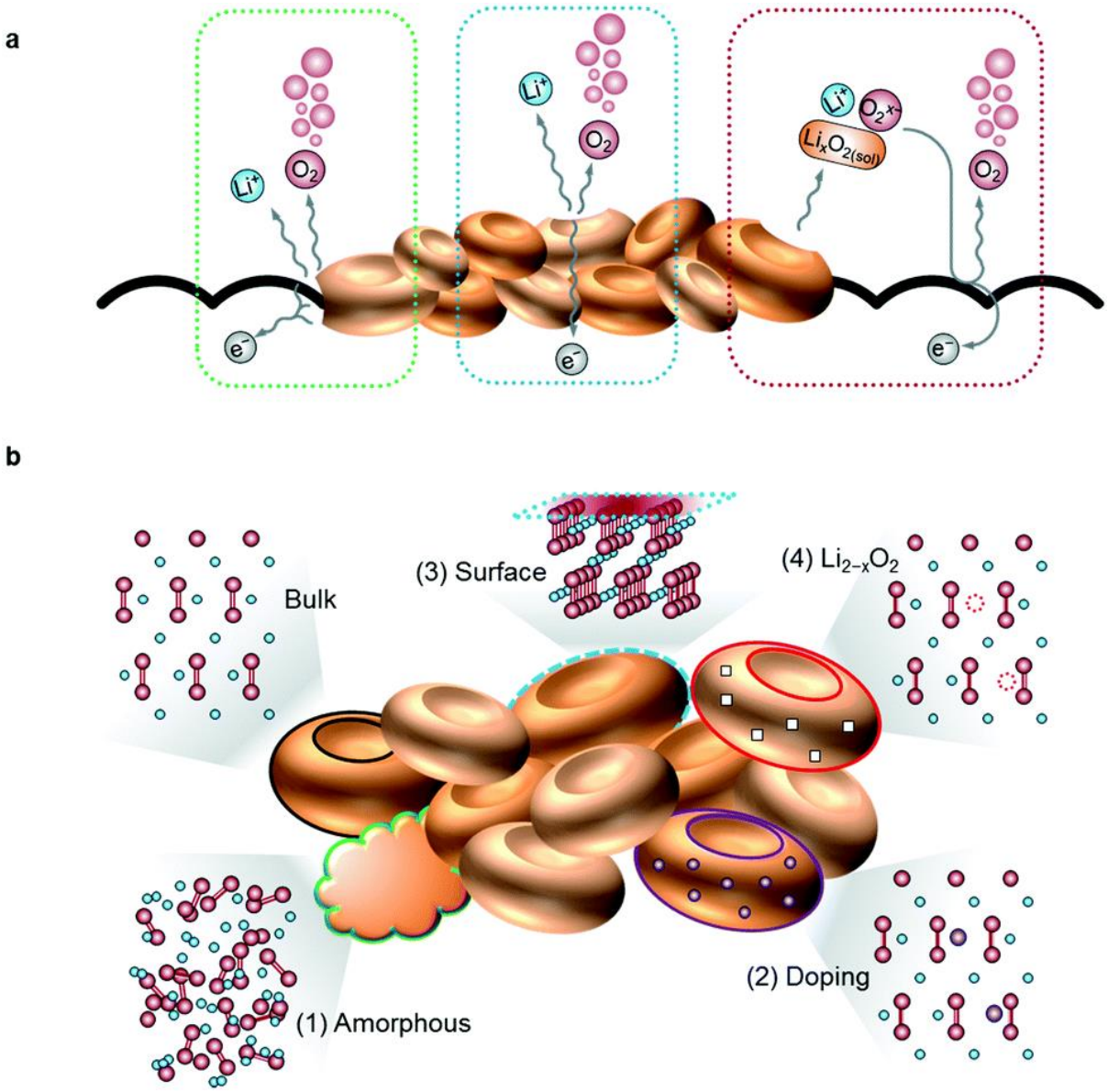

Figure 2.4. Reaction sites of Li_2O_2 decomposition and various atomic structures of Li_2O_2. (a) Possible reaction sites for electrochemical decomposition of Li_2O_2. (b)Atomic structures of defects in Li_2O_2. Reproduced from reference [1] by permission of The Royal Society of Chemistry.

Electrical charge transport is another key parameter influencing the electrochemical mechanism of OER process in Li-O_2 batteries by altering the decomposition speed of Li_2O_2. Electrochemically formed Li_2O_2 is found to present higher electrical charge transport than commercial Li_2O_2 crystalline powder due to the defects formed during the battery operation [32-33]. As presented in Figure 2.4b (1), amorphous Li_2O_2 with higher electronic conductivity than that of crystalline Li_2O_2 is one of the common defects observed in Li-O_2 batteries [34-35]. Another Li_2O_2 defects can be attributed to the heteroatom doping in Li_2O_2, which happens when

discharge products contact with metal oxide catalysts. Radin and co-workers discovered a 10 orders magnitude of electronic conductivity increase with the Li_2O_2 defects introduced by Co doping [36]. Finally, topotactic delithiation of Li_2O_2 is one of the most noticed defects in electrochemically formed Li_2O_2 that have proven to have the potential to improve the conductivity of discharge product [33, 37-38].

Due to the various morphology of electrochemical formed Li_2O_2, the mechanism of decomposition could be classified into two types. For film-like Li_2O_2, the discharge product mainly presents in a quasi-amorphous nature and the thickness is usually in a range of few nanometers [15, 39]. As mentioned above, as amorphous Li_2O_2 presents higher electronic conductivity, the electrochemical decomposition of Li_2O_2 is faster and the OER polarization is smaller when charge transport occurs via election tunneling through the film [27, 40]. Moreover, the large contact area between electrode and film-like Li_2O_2 has been proven to effectively promote the OER kinetics and therefore to achieve a low charge voltage [41]. On the other hand, crystalline Li_2O_2 potentially hinders the charge transport due to its poor electronic conductivity [8]. At beginning, Li ion is diffused out from crystalline Li_2O_2 to form a defective form of $Li_{2-x}O_2$, which is more electronic conductive. The $Li_{2-x}O_2$ will then be oxidized to release Li ions and oxygen when a charge plateau would be observed on galvanostatic charge/discharge figure. Further decomposition of residual byproducts such as Li_2CO_3 continued to take place at a higher potential. Compared with film-like Li_2O_2, the decomposition of crystalline Li_2O_2 have higher overpotential, due to the high charge voltage plateau [42]. Thus, during charge, non-crystalline Li_2O_2 is removed first at low voltage, and crystalline Li_2O_2 is proposed to charge via the Li-deficient solid solution ($Li_{2-x}O_2$) phase, followed by the oxidation of byproducts at a higher potential.

Like discharge process, the introduction of soluble OER catalysts or OER mediator can lower the charge potential by the following mechanism:

$$\text{(OER mediator)} \rightarrow \text{(OER mediator)}^+ + e^- \qquad (2.7)$$

$$2(\text{OER mediator})^{+} + Li_2O_2 \rightarrow 2(\text{OER mediator}) + 2Li^{+} + O_2 \quad (2.8)$$

Due to a higher redox potential, OER mediator can be oxidized before the oxidization of Li_2O_2 happens (Reaction 2.7) [43]. Then the oxidized OER mediator further chemically decompose Li_2O_2 into lithium ion and oxygen (Reaction 2.8) [44]. Lim and co-workers simply illustrated the mechanism of these process in Figure 2.5 [30].

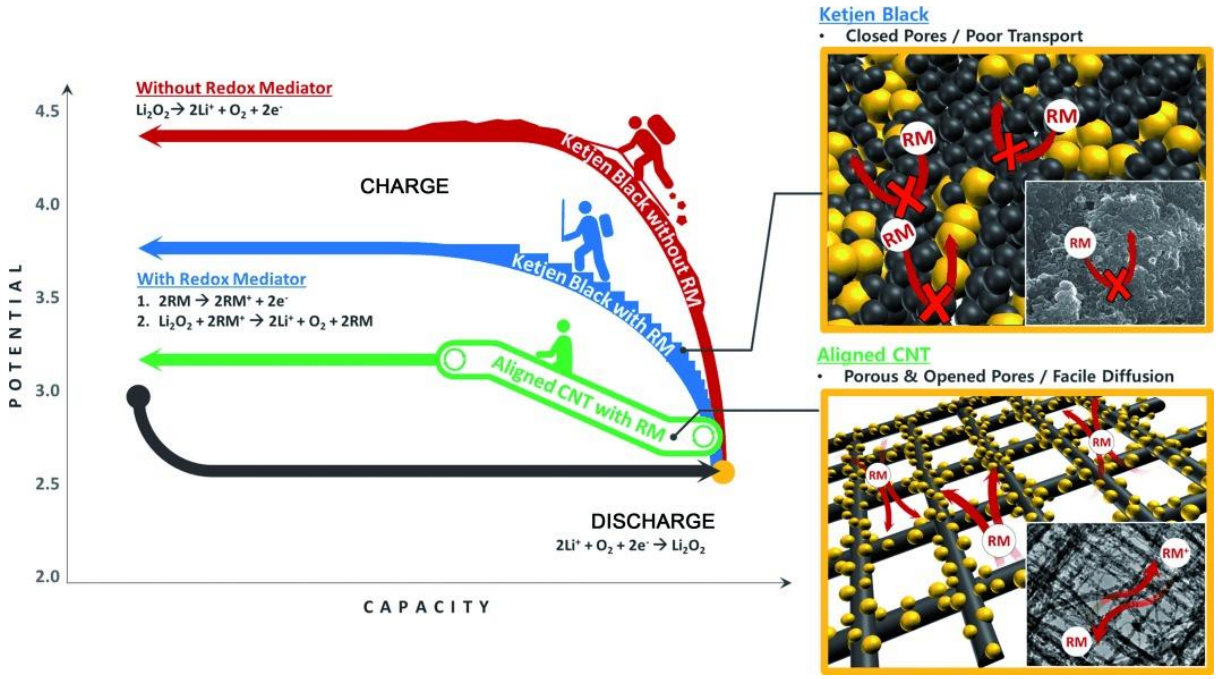

Figure 2.5. Schematic illustration of the role of the redox mediator (RM) in a Li-O_2 battery system using a hierarchical CNT fibril electrode. Reproduced from reference [30] with permission from WILEY (Copyright 2014 WILEY-VCH Verlag GmbH & Co. KGaA, Weinheim).

2.1.2 Oxygen Electrodes and Catalysts

The goal of the investigation of Li-O_2 batteries is to achieve long cycling life Li-O_2 batteries with high specific capacity. The achievement of this goal strongly depends on the oxygen electrode materials and the catalysts [3]. As described in section 2.1.1, the overall capacity and energy density of Li-O_2 batteries depends on the formation and decomposition of discharge product Li_2O_2. Therefore, an ideal cathode material should provide proper structure for storage of Li_2O_2, high catalytic activity toward ORR/OER, sufficient electron and mass transport property, and stability against parasitic reactions.

2.1.2.1 Carbon materials

Carbon has intensively been chosen as oxygen electrode material for Li-O_2 battery due to its low cost, good electrical conductivity, rich oxygen diffusion channels, and large space for housing the discharge products [3]. Research has also found that carbon materials can act as ORR catalysts [45]. Moreover, carbon cathode materials provide the possibility for heteroatoms doping (eg. N, S, P and B, etc.) to further tailor their properties [46]. In this direction, various carbon materials such as commercial carbon black, graphene, carbon nanotubes, mesoporous carbon etc. have been widely used in current Li-O_2 cells.

(a) Graphene

Graphene is a two-dimensional carbon nanostructure with high mechanical strength, large specific surface area, and thermal and chemical stability. However, the low activity of sp^2 carbon on the basal plane is not favorable for electrochemical reactions in Li-O_2 batteries [47]. It can be improved by introducing stable defects on graphene surface, such as the form reduced graphene oxide (rGO) [48]. Porous structure can also improve electrochemical activity by bending the sp^2 structure. Wang and co-workers achieved a super high discharge capacity at 17700 mA h g^{-1}, and a long cycle life up to 200 cycles (under the curtaining capacity of 1000 mA h g^{-1}) with porous graphene cathode materials for Li-O_2 batteries [49]. Another simple approach to increase defects in graphene is heteroatom doping. For example, when using as cathode for Li-O_2 batteries, N can promote ORR catalytic activity and S can promote OER catalytic performance for graphene materials.

Furthermore, the possibility of building 3D framework is another advantage of graphene. Along with the high surface area, 3D graphene has the potential to form high speed electronic channels with high tensile strength. In this case, the heavy current collector can be eliminated from the cathode to achieve significant improvement of specific capacity for Li-O_2 batteries [50-51].

(b) Porous Carbons

Due to the high porosity as well as the high specific surface area, porous structure has been

widely employed in carbon cathode design for Li-O_2 batteries to provide sufficient charge transfer for the electrochemical reactions and space for housing discharge products. Porous structure can be fabricated with porous templates, such as polystyrene spheres and silica nanoparticles, or through chemical vapor deposition (CVD) process [49, 52-53]

Park and co-workers compared Ordered mesoporous carbons (OMCs) with two different pore size of 6 and 17 nm [54]. Larger pore size with 35 and 36 nm were then tested by Xie et al. and Kim et al. [55-56]. However, limited by the pore size, mesopores were prone to be blocked by the accumulation of discharge products or by-products, and eventually resulted in low specific capacity and short cycle life for Li-O_2 batteries. In order to tackle this problem, Kang and co-workers incorporated macropores that are larger than 200 nm onto OMCs to improve the electrochemical performance of Li-O_2 batteries [57]. Figure 2.6 illustrates the pathways of order micro-porous carbon (CMK-3) and interconnected meso-porous carbon (MSU-F-C)[58].

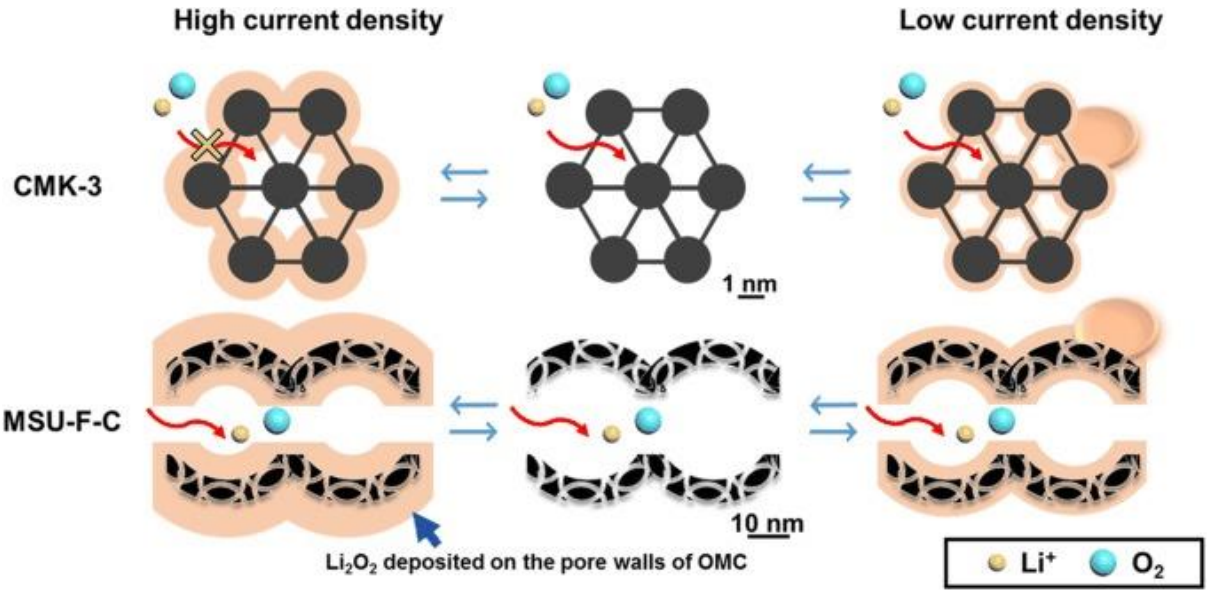

Figure 2.6. Schematic demonstration of the mass transport of reagents through the pore structures of mesoporous carbons. Reproduced from reference [58] with permission from WILEY (Copyright 2015 WILEY-VCH Verlag GmbH & Co. KGaA, Weinheim).

(c) Heteroatom-doped carbons

Heteroatom doping is a feasible method to modify carbon materials for better electrochemical properties. Due to the presence of dopants, charge distribution over carbon surface can be rearranged to form more active sites for both chemical and electrochemical reactions. Among all the dopants, the metal-free heteroatom (eg. N, and S) doped and nitrogen and transition metal co-doped carbon (M-N-C) catalysts show great promises acting as oxygen electrode for Li-O_2 batteries.

Due to the large electronegativity of nitrogen than carbon, the substitutional of nitrogen atom can form polarized C-N bonds, where carbon atoms to be positively charged and become more active for O_2 adsorption [59]. The uniform N doped on the carbon surface also provides more nucleation sites, facilitating better distribution of discharge products to reach a higher specific capacity[60]. Melamine and ammonia are two of the common nitrogen sources for nitrogen doping [61-62]. Previous research has found that with about 10 at % nitrogen, the specific discharge capacity of N-doped carbon nanotube (CNT) can be 1.5 times as that of pristine CNT in Li-O_2 batteries [63].

Chen and co-workers explored the relationships between N, S doping and cathodic performance for Li-O_2 batteries. N can facilitate ORR by breaking the uniformity of charge distribution on graphene basal plane, while S stabilized graphene from degradation to extend cycle life for Li-O_2 batteries [64].

Boron-doped rGO with porous structure presents high discharge capacity, low overpotential and excellent rate capability. Lu and co-workers suggest the doping of B atom greatly activates the electrons through conjugation effects and B-rGO promotes the charge transfer between Li_2O_2 and cathode [65].

N, and transition metal co-doped carbon catalysts can improve the electrochemical activity in harsh environment such as acid electrolyte. In a typical M-N-C catalyst, carbon is the dominant element that will take up to 85 at %, graphitic and pyridinic nitrogen may take another 8 at%,

and a transition metal (Fe, Co etc.) can be as high as 5 at % [66]. The mechanism of M-N-C is not fully understood yet, and the role of the transition metal seems to be controversial. It is unclear that whether transition metals are the active sites, or they just promote the ORR performance of nitrogen doping into carbon. Nevertheless, the catalytic performance of M-N-C was found strongly related to the synthetic chemistry of catalysts, including the structure of nitrogen precursor, transition metals, heating conditions, and post treatments [67].

2.1.2.2 Metal oxides

Metal oxides, especially transition metal oxides, are among the most studied electrocatalysts due to their many advantages, including multiple valence states and relatively high electrochemical activities. In this section, we will discuss ruthenium oxide, and various transition oxides, including manganese oxide, cobalt oxide, titania and ferric oxide.

(a) Ruthenium oxide

Though ruthenium oxide is not as economic friendly as transition oxides are, it is indeed the first and still one of the best electroactive materials. Due to its pseudocapacitive behavior, ruthenium oxide possesses active redox sites with different levels of energy, which enables RuO_2 to participate and function as a redox mediate in the electrochemical reactions at different potentials. Therefore, RuO_2 presented excellent catalytic performance in reducing the overpotential of Li-O_2 batteries and consequently improve the cycle stability to reach a long cycling life [68]. However, the heavy atom mass of RuO_2 makes it significantly reduce specific capacity of Li-O_2. To tackle this problem, a transition metal oxide is mixed with RuO_2, and the specific capacity was found to be improved in comparison with individual ones [69]. Another approach was reported by Xia and co-workers to successfully increase the specific capacity of Li-O_2 batteries by coating RuO_2 on mesoporous carbon to improve the specific surface area [70].

(b) Manganese oxide

Manganese oxide with advantages, such as high abundance, low-cost, acceptable ORR activity, and environmental friendliness, has been studied as a potential cathodic-catalysts for Li-O_2

batteries [71-72]. Since the report shows excellent catalytic performance of α-MnO_2 by Bruce et al., efforts have been taken to find the best polymorph of MnO_2, such as α, β, δ, γ, λ and ε-MnO_2 for cathodic process [73]. The ORR catalytic activity of these MnO_2 phases in alkaline solution was found as following sequence: α-MnO_2 ≈ δ- MnO_2 > γ- MnO_2 > λ- MnO_2 > β- MnO_2 [74].

The special 2×2 tunnels formed by edge and corner sharing MnO_6 octahedra in α-MnO_2 are excellent active sites to accommodate both Li^+ and O_2^- for the incorporating reaction to promote the formation of Li_2O_2, leading to a high specific capacity [73]. However, α-MnO_2 cannot reduce the potential of OER [75]. Various materials with high OER catalytic activity such as Pd, and Ag were applied as additives to α-MnO_2 for a lower overpotential in Li-O_2 batteries [76-77].

δ- MnO_2, on the other hand, has been reported to considerably reduce the overpotential of both ORR and OER on ketjenblack (KB) carbon, especially at high current rate [78]. It has been proved that the presence of δ- MnO_2 facilitates the formation of toroidal Li_2O_2, as demonstrated in Figure 2.7. Due to the low binding energy between LiO_2, Li_2O_2 are mainly formed on the carbon materials rather than attached on δ- MnO_2 surface [78-79]. Moreover, the oxygen vacancies on MnO_2 is proved to be effectively improve the catalytic activities for both ORR and OER by providing more active sites [80-81].

(c) Cobalt oxide

Co_3O_4 gives the best compromise between ORR and OER electrocatalytic activities and promotes the interfacial transition of LiO_2 [82-83]. The electrochemical performance of Co_3O_4 is greatly dependent to the specific surface area, thus the architecture and morphology design of Co_3O_4 is one of the important strategies for carbon-free cathode. When anchored with graphene, Co_3O_4 changes the charge transfer pathway and displays excellent cyclability for Li-O_2 batteries [84-85].

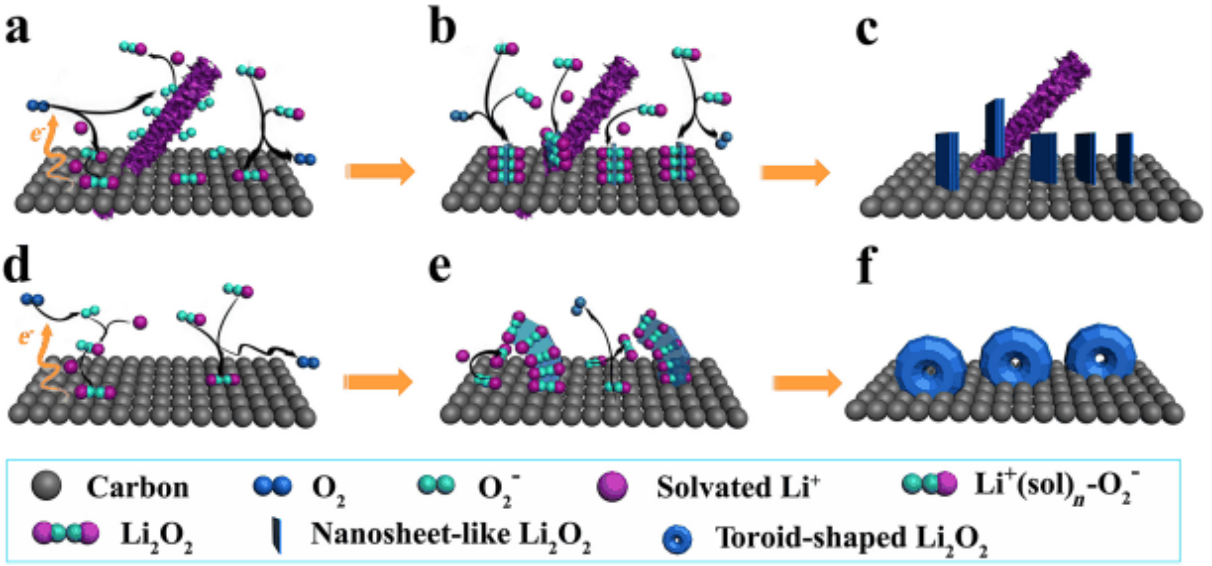

Figure 2.7. Proposed mechanism for the formation of the discharge product with different morphologies on (a-c) MnO_2/KB electrode (nanosheet-like Li_2O_2) and (d-f) KB electrode (toroidal Li_2O_2). Reproduced from reference [79] with permission from WILEY (Copyright 2015 WILEY-VCH Verlag GmbH & Co. KGaA, Weinheim).

Cobalt (II) oxide and its composites show excellent cyclability due to their high adsorption energy for LiO_2 from -2.7 to -13.4 eV, which can help to suppress the formation of byproduct Li_2CO_3 during the operation of Li-O_2 batteries, and lead to low overpotentials [86-87].

(d) Titanium oxide

With high mechanical and chemical properties, TiO_2 is studied in various electrochemical systems [88]. Kang et al reported the performance of rutile is better than anatase TiO_2 for rechargeable Li-O_2 battery [89]. It has found that the surface of TiO_2 are prone to absorb electrolyte during the formation of Li_2O_2, which results in the generation of amorphous Li_2O_2 thin film [90]. As discussed in section 2.1, amorphous Li_2O_2 thin film encourages charge transfer between reactants. The chemical irregularities, such as oxygen deficiency on TiO_2 promotes catalytic performance by accelerating the electronic transport at electrochemical reaction sites [91].

(e) Ferric oxide

Ferric oxides attracted many interests due to its non-toxicity, low cost and environmental

friendliness, and shows considerable electrochemical catalytic performance in Li-O_2 batteries [92-93]. In order to improve the ORR and OER catalytic activity, carbon materials are usually applied together with ferric oxide to form composites as cathode material in Li-O_2 batteries [93].

(f) Ternary metal oxide spinels

Ternary metal oxide spinels such as $ZnCo_2O_4$, $CoFe_2O_4$ and $CoMn_2O_4$ displays great bi-functional electrocatalytic performance for Li-O_2 batteries [94-96]. The main strategy to advance their catalytic activity is to design specific morphology or achieved homogeneous dispersion ternary metal oxide spinels on high specific surface area substrates [95-96].

(g) Perovskite metal oxide

Perovskite oxides are metal oxides with ABO_3 structure (A: alkaline or rare earth cations, B: transition metal cations) exhibiting many attractive properties, such as good electrochemical stability, high electronic/ionic conductivity, and tunable catalytic activity [97]. Perovskite metal oxides significantly promote Li-O_2 battery performance [98-99].

2.1.2.3 Metal carbides and nitrides

In comparison with metal oxides, metal carbides and nitrides possess higher electrical conductivity [100-101]. The highly ordered lattice structures make metal carbides/nitrides function in a different way from metal oxides in facilitating ORR/OER electrochemical process, in which the later are mostly dependent on the presence of vacancies and defects [47].

(a) Carbides

Transition metal carbide exhibited excellent electronic conductivity due to their d-orbital states that promote the electron transport between discharge products and cathode material to lower the overpotential and improve the specific capacity of Li-O_2 batteries [102-103].

TiC is reported to delivered reasonable specific capacity and stable cycling life for Li-O_2 batteries as TiC effectively reduces side reactions of electrolyte and electrode degradation [104]. Nazar and co-workers discovered that the charge transfer and effective OER will only happen

when TiC passivation layer is less than 2 nm [105]. Mo_2C nanoparticles promotes the formation of Li_2O_2 nanolayers on the cathode materials to reduce the overpotential and improve the cycling performance [106-107]. When composed with carbon materials, 3D carbon foam supported Mo_2C exhibits excellent bifunctional catalytic performance in both ORR and OER for Li-O_2 batteries. The dispersion of Mo_2C on carbon fibres prevents the aggregation of discharge products during extensive cycling [108]. XPS studies indicate Mo_2C performing as a redox mediate to promote Li_2O_2 decomposition by the formation of $LixMoO_3$ on Mo_2C at low potential [109].

(b) Nitrides

The high electronic conductivity, acceptable electrocatalytic activity and high chemical stability, enable transition metal nitrides act as efficient catalysts in various electrochemical reactions.

The electrocatalytic performance of TiN was found to be closely related to its particle size. Micro sized TiN presents decent electrocatalyst performance toward to ORR in aqueous Li-O_2 batteries [110]. A composite of MoN doped graphene nanosheets displays a reasonable discharge capacity and a high discharge plateau, suggesting a good ORR catalytic performance of MoN [111]. Nitridized Co_3O_4 can increase specific capacity, enhance cycling life, and reduce the overpotential of Li-O_2 batteries by accelerating electron transport [112-113]. The changes of morphology, electron density, and electronic structure caused by the introduction of nitrogen atom are the main reasons for the promotion of catalytic performance [114].

2.1.2.4 Noble metals and alloys

Noble metals are considered as efficient catalysts for many electrochemical systems because of their high stability and superior electrocatalytic activity [115]. The intrinsic half-filled antibonding state allows noble metals provide proper adsorption strength between catalysts and the reaction precursors to achieve high catalytic performance towards to both ORR and OER [116].

For Li-O_2 batteries, Pt, Pd, Au, Ru, and Ir have been employed as oxygen electrode catalysts with or without carbon support [16, 117-120]. Shao-Horn and co-workers discovered that according

to the oxygen adsorption energy, the order of surface catalytic activity for noble metals in nonaqueous Li-O_2 batteries is: Pd > Pt > Ru ≈ Au > glassy carbon [118]. However, similar to RuO_2, the heavy atomic mass of precious metals lowers the specific capacity of Li-O_2 batteries. Thus, alloys are introduced for better performance as well as lower cost.

The presence of addictive metal, such as transition metals or other precious metal, in alloys reduces the adsorption energy and facilitates the separation of the Li_2O_2 formed on the noble metal via surface diffusion process [121]. Because of the non-uniformed elements on the alloy surface, the charge distribution is not homogeneous dispersed, which is favorable for oxygen adsorption process during the operation of Li-O_2 batteries [122].

2.1.3 Electrolyte and Additives

2.1.3.1 Electrolyte

Initially, organic carbonates were used in Li-O_2 batteries and achieved excellent performance on the battery performance. However, it was later found the reactions were caused by decomposition of electrolyte rather than ORR/OER [4]. This finding encouraged researchers to explore new electrolytes for non-aqueous Li-O_2 batteries. Current research on electrolytes in Li-O_2 batteries focus on following areas: 1) ether-based electrolytes, 2) ionic liquids, 3) amide-based electrolytes, 4) sulfone-based electrolytes, and 5) dimethyl sulfoxide electrolytes [123].

Ethers attract much attention as an alternative to organic carbons due to their stability towards reduced O_2 and Li_2O_2, good wetting property for electrodes, low volatility, safety and low cost [20]. Some of ethers including tetraglyme ($CH_3O(CH_2CH_2O)_4CH_3$), dimethoxymethane ($CH_3OCH_2CH_2OCH_3$; DME), tetraethylene glycoldimethyl ether (TEGDME) and polythyleneoxide (PEO) [124-128]. However, decomposition of electrolytes is still presented in ether-based electrolytes as Li_2CO_3, HCO_2Li, and CH_3CO_2Li were later found after long cycles [126-127]. Despite the disadvantages, ether base electrolytes remain the most widely used electrolyte in non-aqueous Li-O_2 systems.

Other organic electrolytes have also been investigated in Li-O_2 batteries in recent years, such as dimethylformamide (DMF; amide-based electrolytes) [129-130], ethylmethylsulfone (EMS; sulfone-based electrolytes) [131], and dimethyl sulfoxide (DMSO)[132-133]. Among all the potential electrolytes, Peng and co-workers reported a very steady secondary Li-O_2 cell with $LiClO_4$/DMSO as the electrolyte and a Nano porous gold (NPG) as the cathode[134]. The cell was able to cycle up to 100 times without obvious decrease of the performance. A redox mediator, tetrathiafulvalene (TTF) was introduced in the later stage by the same group to reduce the high charge potential [133]. However, due to the instability of DMSO, the cells can only be charged to 4V [3], or the electrolyte will be decomposed [123].

Another electrolyte candidate for Li-O_2 batteries is ionic liquids. Ionic liquids are liquid salts at room temperature, which possesses many advantages, including negligibly low vapor pressure, non-flammability, low toxicity, stable chemical property, and comparable large electrochemical windows [135]. The first research on ILs in Li-O_2 batteries were reported by Kuboki and co-workers in 2005 [136], they applied EMITFS as electrolytes to prove the possibility of application of ILs in Li-O_2 batteries. After that, ionic liquids have been used as electrolyte alone or mix with other organic solvents and presented promising Li-O_2 performance [137-139]. However, the high viscosity of ionic liquids hindered their application in Li-O_2 batteries, and more investigation needed to be done for further application.

2.1.3.2 Suitable lithium Salts

Lithium salts are crucial in affecting the polarization of Li-O_2 batteries, which can also influence the capacity and reversibility in the batteries [20, 140]. A suitable Li salts should be highly soluble in electrolyte, be stable in rough environment, and be inert to solvent and current collectors.

Currently, the most studied Li salts for Li-O_2 batteries are $LiPF_6$, Lithium bis(trifluoromethylsulfonyl)amide (LiTFSA), $LiClO_4$, $LiNO_3$ and LiTFSI. However, many Li salts are found to be instable during discharge/charge process. For example, Oswald et al. found

$LiPF_6$ reacts with Li_2O_2 to decay the cycling performance of Li-O_2 batterers [141]. The compatibility of Li salts with electrolyte is critical to the electrochemical system. TEGDME solvent is found to be compatible with various Li salts such as $LiPF_6$, LiTFSI and $LiCF_3SO_3$ for stable cycling performance of Li-O_2 batteries [142].

2.1.3.3 Effective additives

In order to enhance the cyclability and round-trip efficiency of Li-O_2 batteries, inorganic salts or organic compounds are added into the electrolyte as additives. These additives mainly function in two ways to improve the cell performance: 1) promote the formation of SEI film to protect Li anode and 2) improve the solubility of oxygen gas and discharge products to increase the specific capacity [20].

2.1.4 Configuration of Li-O_2 Batteries

Currently, Li-O_2 batteries are mainly assembled in two ways, Swagelok-type (Figure 2.8a) and coin cell type (Figure 2.8b).

The Swagelok^{TM}-type Li-O_2 battery is a typical model used at Almaden Research Center, IBM research. The model contains a Li metal foil anode, an electrolyte-soaked separator, a porous carbon cathode, and a stainless-steel mesh current collector [143]. The high purity oxygen is filled in from inlet and released to outlet to keep oxygen environment for batteries. The cell is connected to a mass spectrometer (MS) for quantitative analysis of the oxygen consumed in discharge and the O_2 evolved during charge. This kind of battery model faces serious cleaning problem as the Swagelok^{TM} cell is not disposable, the residue from previous batteries may have huge impacts on following batteries.

Coin cell Li-O_2 batteries, on the other hand, attracts more attentions recently (Figure 2.8b). Oxygen electrode, electrolyte-soaked separator and fresh Li anode are fabricated in a 3032-coin cell in an argon-filled glove box. A plug sealed bottle (Figure 2.9) is used to maintain the oxygen environment for coin cell Li-O_2 batteries.

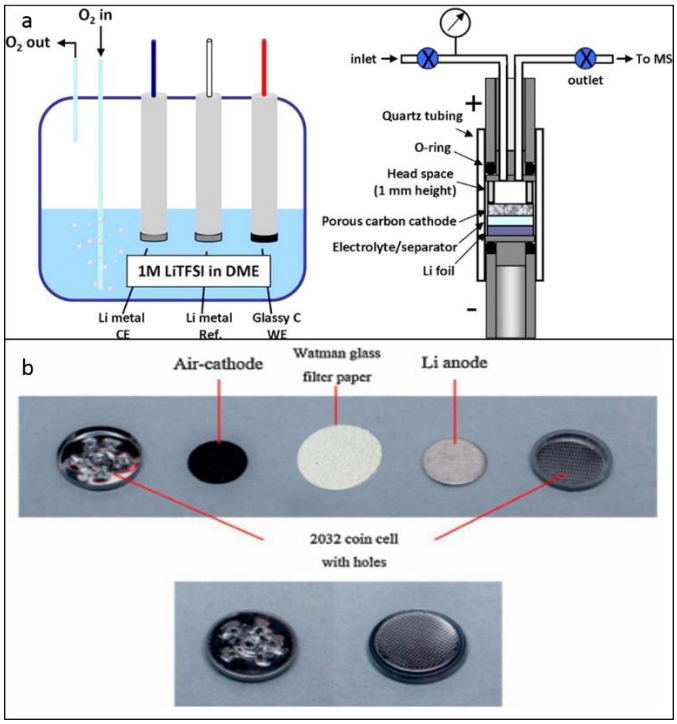

Figure 2.8. (a) Schematic demonstration of a Swagelok^{TM}-type Li-O_2 battery, Reprinted with permission from reference [143]. Copyright 2012 American Chemical Society. (b) Configuration of a coin-cell type Li-O_2 battery. Reproduced with permission from Elsevier, reference [144].

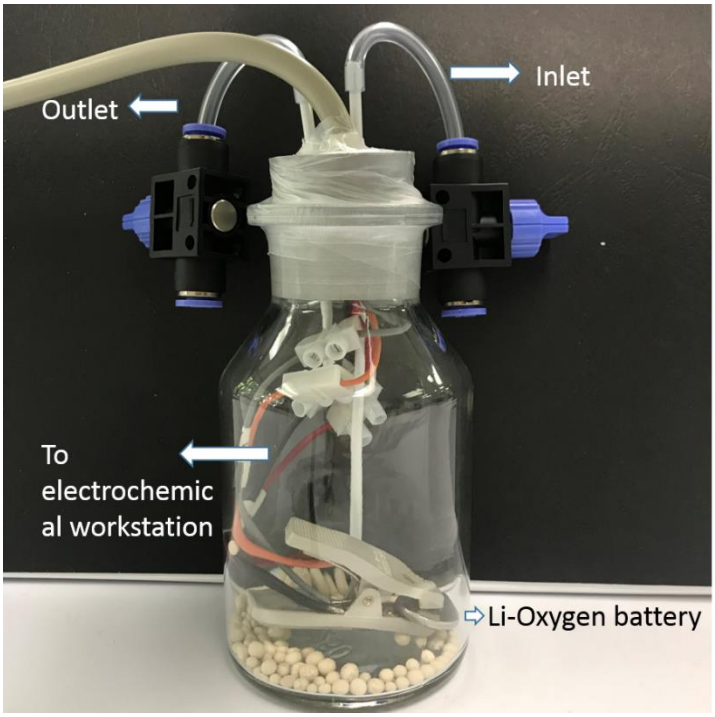

Figure 2.9. Image of a Li-O_2 battery in a plug sealed oxygen-filled bottle.

Two gas ports are built into the bottle plug for oxygen inlet and outlet. After 10 - 15 mins constantly oxygen flow, the oxygen filled bottle is sealed by two switches at the end of inlet and outlet ports. The coin cell is placed in-between a metal clip, where the wires lead to an electrochemical workstation for battery and electrochemical tests. Desiccant can be added into the bottle for moisture adsorption. Compared with the Swagelok type, the coin cell type Li-O_2 batteries possesses many advantages in fabrication and cleanness. In this thesis, all the Li-O_2 batteries are configured in coin cell type.

2.2 Reduced Graphene Oxide (rGO) and N-Doped Graphene

Since discovered by Andre Geim and Konstantin Novoselov in 2004, graphene has attracted many interests in widely research fields, due to its great properties in mechanical, thermal and electrical. However, as mentioned previously, the perfect structure of graphene makes it unfavourable for the chemical reactions to take place. Therefore, defects are introduced to graphene as active sites for both ORR and OER reactions. In this section, reduced graphene oxide and N-doped graphene will be discussed as the effective ways to increase defects on graphene.

2.2.1 Reduced Graphene Oxide

Graphene oxide (GO) is carbon nanosheets exfoliated from graphite oxide, containing only one or few layers of carbon atoms like graphene [145]. Reduced graphene oxide is achieved by removing the oxygen-containing groups with the recovery of a conjugated structure of GO. This section will focus on the preparation of GO, and the methods to further reduce GO to rGO.

2.2.1.1 Preparation of graphene oxide (GO)

GO was first reported in 1840 by Schafhaeutl and 1895 by Brodie [146-147]. Currently, the preparation of GO is mostly based on the method proposed by Hummers and Offeman in 1958

[148]. The oxidation of graphite is accomplished by treating graphite with a water-free mixture of concentrated sulfuric acid, sodium nitrate and potassium permanganate. This procedure releases toxic gases including NO_2, N_2O_4, and is highly explosive due to the presence of $NaNO_3$. Therefore, many modifications have been suggested [149-150], including an improved method proposed by Tour and co-workers in 2010 [151].

The improved Hummer's method avoids the potential of explosion by eliminated the usage of sodium nitrate. Additional phosphoric acid is added into the concentrated sulphuric acid in a proportion of 1:9 to achieve high oxidation. The GO prepared by improved Hummer's method possess more basal plane framework retained. After reduced with Hydrazine hydrate, the same level of conductivity is tested with Hummer's method GO [151].

2.2.1.2 Methods for GO reduction

(a) Thermal reduction

Thermal reduction is a process to reduce GO by heat treatment. Due to the rapid temperature increase, the oxygen containing functional groups attached on carbon plane decompose into gases. This procedure enables the reduction and exfoliation happening at the same time, which makes it a good strategy to produce bulk quantity graphene [152]. However, carbon atoms can be removed at the same time [153]. It has been found that around 30% of mass loss occurs during the exfoliation process, resulting in the distortion and lattice defects throughout the rGO sheets [154].

In this strategy, the annealing temperature is one of the most important factors to reduction on GO. Schniepp et al. found that when less than 500 °C, the carbon to oxygen atomic ratio (C/O ratio) is less than 7, indicating high presence of oxygen containing groups and low reduction degree, while the high level of reduction can be achieved when the annealing temperature is higher than 750 °C, when the C/O ratio could be higher than 13 [154].

The annealing environment is another factor that plays an important role in the reduction of GO. The oxygen should be excluded during the annealing in case the etching of oxygen with GO at high temperature. Therefore, the annealing mostly happens in vacuum, or an inert (N_2, or Ar),

or a reducing (H_2, Ar/H_2) atmosphere [155-157].

Apart from the direct thermal irradiation, microwave irradiation (MWI) and photo-irradiation were applied to the thermal reduction of GO recently [158-159]. By treating GO with MWI, the exfoliation process can be more rapidly with uniform-structured [158]. On the other hand, the photo-irradiation is more favourable to fabricate rGO with patterns by simply shielding the light [160].

(b) Chemical reduction

The chemical reduction is based on the chemical reactions between chemical reagents with GO, which can be carried out at the room temperature.

The reduction of GO by hydrazine can be traced to years before the discovery of graphene and has been widely used since then [161]. The rGO reduced through this approach can possess a conductivity as high as 99.6 S/cm with a C/O ratio around 12.5 [162]. Other chemicals such as sodium borohydrides, hydroiodic acid are then explored as new chemical reagents for chemical reduction of GO [163-164].

Ascorbic Acid (Vitamin C) is recently discovered as an ideal alternative for hydrazine to react as reducing reagent for GO, with a conductivity of 77 S/cm and a C/O at 12.5. The non-toxicity and mild reduce reactions make ascorbic acid safer and easier to control. Moreover, the presence of vitamin C can effectively avoid the aggregation of rGO sheets when reduced in colloid state [162].

2.2.2 N-doped Graphene

Substitutional doping of heteroatoms such as nitrogen, boron, and sulphur, to graphene has attracted largely attention to improve the electronic and chemical properties of graphene material. Among them, N-doped graphene are viewed as one of the most promising materials to alternate the precious metals in enhancing graphene's ORR activity with relatively low cost

[165].

Pyridinic, pyrrolic and graphitic are three forms of bonding configurations to connect nitrogen with carbon atoms for N-doped graphene, as show in Figure 2.10 [166].Specifically, pyridinic N is bonded with two carbon atoms at the edges or defects of graphene as a member of hexagon. Pyrrolic N bonds with two carbon atoms in a five membered ring and contributes two p electrons to the π system. Graphitic N refers to N atoms that replace C at the centre or valley of several hexagonal ring [166]. Among these nitrogen types, pyridinic and graphitic N are sp^2 hybridized and pyrrolic N is sp^3 hybridized [165]. Pyridinic and graphitic N are viewed as active N that facilitate the process of catalytic performance in electrochemical reactions and are much favourable for Li-O_2 batteries.

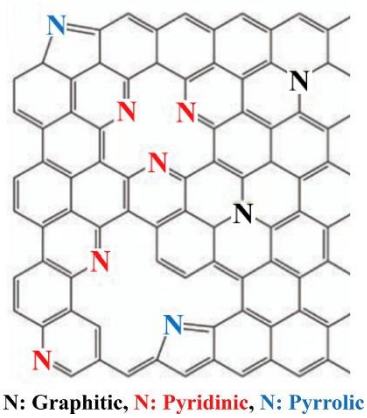

Figure 2.10. Atomic structure of N-doped graphene. Reproduced with permission from Elsevier, reference [166].

2.2.2.1 Preparation of N-doped graphene

Many approaches have been proposed for N-doped graphene preparation, which can be classified into two ways: direct synthesis and post treatment. Specifically, direct synthesis includes chemical vapour deposition (CVD), solvothermal, and arc-discharge approaches. Post treatment includes thermal treatment, and plasma treatment. Detailed discussions on these methods are followed below.

(a) Chemical vapor deposition (CVD)

CVD is one of the earliest methods to synthesize N-doped graphene [167], which usually contains two precursors, N precursor and graphene precursor. In a typical CVD process, NH_3 is chosen as N precursor along with pyridine and polypyrrole are employed as carrier gas [168]. During the CVD, a metal catalyst such as Ni and Cu, and a Si/SiO_2 plate are used as the substrate. Then a mixed gas contains both N and graphene precursors are introduced at a high temperature. These precursors then dissociate and recombine into N-doped graphene on the surface of catalysts [167, 169]. The N contents of this method can vary from 0.25 at % to 16.7 at %, which is highly dependent on the ratio of mixed gas and the decomposition conditions [167-168].

(b) Solvothermal method

The common procedure of solvothermal method is mixing tetrachloromethane (CCl_4) and lithium nitride (Li_3N) together with or without the presence of cyanuric chloride ($N_3C_3Cl_3$), followed by reacting in stainless steel autoclave under inert atmosphere (Ar or N_2) [170-171]. The N contents of this method is in the range from 4.0 to 28.1 at % [172].

(c) Arc-discharge method

As an old-fashioned method for N-doped graphene preparation, Arc-discharge method composes two graphite rods as electrodes. When a current is held, the anode is evaporated into N sources (usually NH_3 and inert gas) to form N-doped graphene [173-174]. The N content of this method is generally lower than 1%, however, the feasible operation in large scale N-doped multi-layered graphene makes it advanced than other methods [173-174].

(d) Thermal treatment

Thermal annealing is a popular approach to synthesize N-doped graphene by heating GO and N sources at a high temperature. The commonly used N sources are NH_3 and melamine [87, 175]. Qu et al. proposed a new approach to introduce N on GO by polydopamine, which shows great ORR catalytic performance [176]. This method contains two steps, the combination between GO

and N precursor, then followed by the thermal treatment at high temperature. This approach attracts many attentions as the N content can be as high as 10.8 at % [177].

(e) Plasma treatment

Plasma treatment is based on the principle that carbon atoms can be partly replaced by nitrogen atoms in a nitrogen plasma atmosphere [178]. This method has been developed for several years, however the low N content (<3.0 at %) makes it hardly to attract further interests [179-180].

2.2.2.2 Characterizations of N-doped graphene

(a) X-ray photoelectron spectroscope (XPS) characterization

XPS is the standard technique for surface analysis as it can reveal the elemental compositions, chemical states and electronic states of the elements from the surface of the material being studied [181]. Figure 2.11a shows the XPS survey of N-graphene, the peaks at around 400 and 243 eV represent the N 1s and C 1s, indicating the successful doping of N on graphene. High-resolution N 1s spectrum shows in Figure 2.11b, a nitrogen peak is split into three peaks, which can be assigned to pyridinic N (398.1 -399.9 eV), pyrrolic N (399.8- 401.2 eV), and graphitic N (401.1 -402.7 eV), respectively [165, 172, 182].

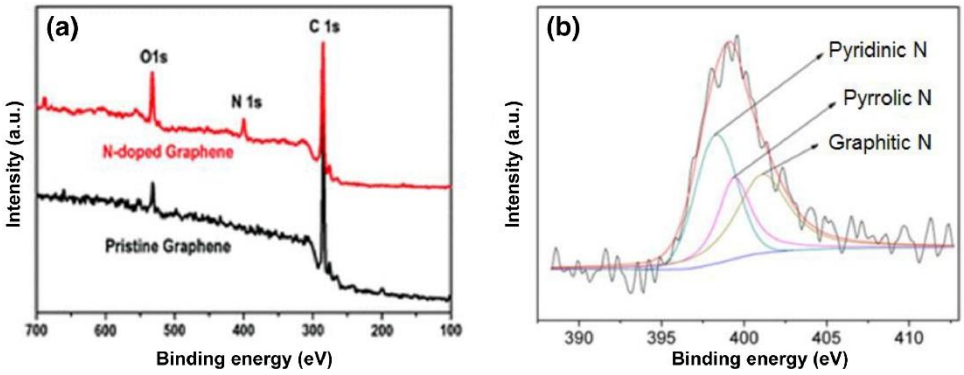

Figure 2.11. XPS (a) survey and (b) N 1s spectrum of N-doped graphene. Reproduced with permission from Elsevier, reference [182].

(b) Raman spectroscopy

Raman spectroscopy is a spectroscopic technique used to observe vibrational, rotational, and other low-frequency modes in a system [184]. The D and G bands displayed at the Ramon spectra at approximately 1320-1350, and 1570-1585 cm^{-1} are the predominant features in the spectrum of N-doped graphene [185-186]. Figure 2.12 is typical Raman spectra of N-doped graphene vs. graphene [183]. The D band at 1340 cm^{-1} indicates the structure defects and other disordered structures that might be caused by the introduction of N atoms, while the G band at around 1570 cm^{-1} was observed for all graphitic structures. The intensity ratio of D band to G band (I_D/I_G) is used to quantify the defects and disordered structures of graphene-based materials [175]. Compared with graphene, the increasing of I_D/I_G of N-doped graphene in Figure 2.12 demonstrated the increasing of defects and disordered structures after the introducing of N atoms. The 2D band at around 2640-2680 cm^{-1} is always observed in carbon materials and were sensitive to the number of graphene layers [174].

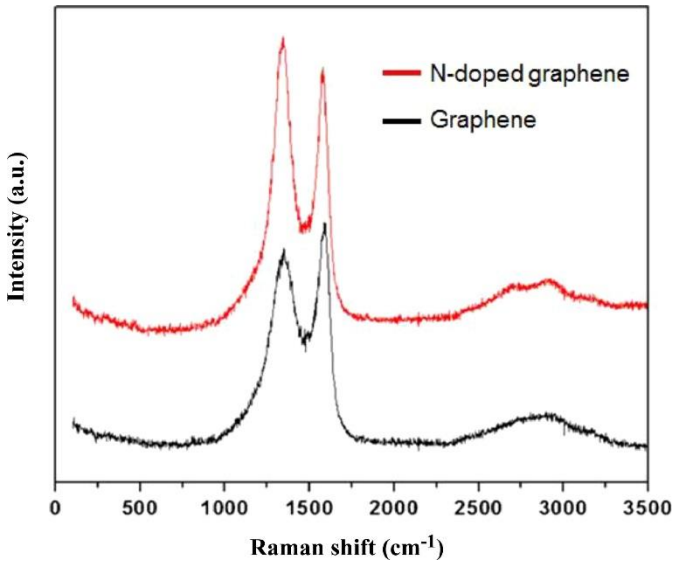

Figure 2.12. A comparison of typical Raman spectra for N-doped graphene and graphene. Reproduced with permission from Elsevier, reference [183].

(c) Other characterization techniques

Apart from techniques mentioned above, scanning electron microscope (SEM), HRTEM, atomic force microscope (AFM), electron energy lose spectra (EELS), infrared spectra (IR) selected area electron diffraction (SAED), N_2 adsorption/desorption isotherm and thermogravimetric analysis (TGA) have also been used to study N-doped graphene [53, 61-62, 173, 187]. Among them, SEM and HRTEM can provide the morphology of N-doped graphene. AFM can be used to estimate the thickness of graphene as well as the number of graphene layers. SAED can tell the crystalline structure of N-doped graphene. N_2 adsorption/desorption isotherm indicates the surface area and porous structure information of sample materials. TGA is used to calculate the weight loss during the temperature increase.

2.3 Cobalt Sulfides

As a common transition metal element, Co can form various metal sulfides, such as CoS, CoS_2, Co_3S_4, and Co_9S_8. Some of these sulfides have attracted much attentions to be performed as ORR, OER and HER catalysts in widely research fields [188-193]. However, the application of cobalt sulfides is still in its infancy with limit reports for Li-O_2 batteries. In this section, we will give a brief review to the electrocatalytic activities of cobalt sulfides, mainly Co_9S_8 and its composites, and their application in electrochemical systems.

2.3.1 Electrochemical Properties of Cobalt Sulfides and Composites

Cobalt sulfides have attracted tremendous attentions for various applications due to their low cost, noble-metal-like catalytic properties, high electrical conductivity, and high chemical kinetic stability [194-196]. These compounds are originally developed for hydrogen evolution reaction (HER) due to their fast charge transfer ability and chemical resistance against acid/alkaline electrolytes. Very recently, both theoretical calculations and experimental results indicate that cobalt sulfides can be applied as ORR/OER electrocatalysts. Cobalt sulfides are

involved in multi-electron redox reactions as electrode materials for batteries and capacitors to achieve high specific capacity that can be double than their oxide counterparts do [197-198]. However, the relatively low conductivity and structural instability hinder their further applications [199].

Among them, Co_9S_8 presents high electrocatalytic performance due to its unique crystal structure [196, 200 201]. Co_9S_8 presents a cubic structure in space group Fm3m (225). The primitive unit cell of Co_9S_8 is shown in Figure 2.13, which contained one octahedral Co atom Co(O), eight tetrahedral Co atoms Co(T), two linking sulfurs S(l) and six face-capping sulfurs S(f) atoms [201]. This structure allows Co_9S_8 possess the optimal number of electrons per atom and therefore to maintain its superior stability.

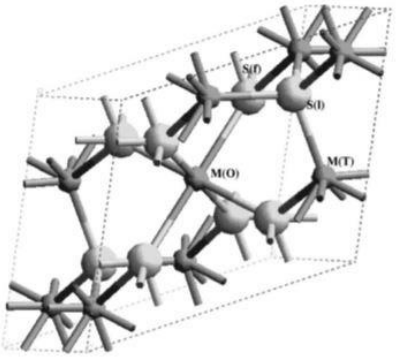

Figure 2.13. Crystal structure of pentlandite: The primitive unit cell of Co_9S_8. M(O), octahedral metal; M(T), tetrahedral metal; S(l), linking sulfurs; S(f), face-capping sulfurs. Reprinted from [201].

The electrocatalytic performance of cobalt sulfides is largely dependent on the high purity, nanostructured morphologies and large surface area. The severe aggregation of cobalt sulfides hinders the full utilization of their electrocatalytic activity. Therefore, apart from various proposal of cobalt sulfides with diverse morphologies, such as hollow Co_3S_4 nanocrystals [202], CoS flowers [203], Co_9S_8 hierarchical microspheres[188], one of the most used strategy is to disperse cobalt sulfides on graphene substrate [191-192].

Shanmugam and co-workers proposed an approach to prepare cobalt sulfide nanoparticles on a nitrogen and sulfur co-doped graphene oxide surface [194]. By changing the temperature (400,

500, and 600 °C)), they obtained CoS_2 (400)/N, S-GO, CoS_2 (500)/N, S-GO, and Co_9S_8(600)/N, S-GO. Among the composites, they found that CoS_2 (400)/N, S-GO exhibits good bifunctional activity in alkaline medium. Al-Mamum et al. then investigated the OER performance of Co_9S_8 nanoparticle on carbon nanosheets with different proportions and achieved a satisfied OER performance better than RuO_2 [204]. Recently, research is conducted to investigate the ORR and OER bi-functional electrocatalytic performance of Co_9S_8-prorous carbon spheres synthesized at different temperatures [196]. The results show that when annealed at 800 °C, the composite demonstrates good stability and excellent activity for both ORR and OER that are comparable to Pt/C catalyst.

2.3.2 Application of Cobalt Sulfides and Composites in Li-O_2 Batteries

Cobalt sulfides and their composites have been applied to various electrochemical systems, including lithium-ion batteries, sodium-ion batteries, supercapacitor, fuel cell and emerging new energy storage systems such as Li-O_2 batteries, because of their unique physical and chemical properties, as well as the rich redox chemistry [205-207]. Couples of review papers have also been published on the application of these materials for energy storage systems [199, 206]. However, to best of our knowledge, there is very limited report on the application of cobalt sulfides on Li-O_2 batteries.

In 2005, Lee and co-workers synthesized a 2D Co_3S_4 in a nano thickness sheet-like morphology via hydrothermal process and applied the materials as a bifunctional electrocatalyst for Li-O_2 system [208]. As a result, the battery reaches a high capacity at 6990 mA h g^{-1} at the current density of 0.2 mA cm^{-2} and an acceptable cycling life for 25 cycles. Later on, CoS_2 nanoparticle-graphene hybrid was employed as a cathode material for Li-O_2 batteries, and achieved a low overpotential that is less than 0.15 V [209]. Very recently, an open structured Co_9S_8 matrix with sisal morphology was synthesized by Dong and co-workers, which provided good contact interface between Li_2O_2 and Co_9S_8-PCF electrode to enable the efficient transport of oxygen and electron [207]. The Li-O_2 batteries with the Co_9S_8 electrode delivered a high discharge

capacity of around 6875 mA h g^{-1} at 50 mA g^{-1} and displayed a low overpotential of 0.57 V under a cut-off capacity of 1000 mA h g^{-1}. The development of cobalt sulfides and their composites as efficient catalysts for Li-O_2 batteries is at the very initial stage.

References

1. Lim, H. D.; Lee, B.; Bae, Y.; Park, H.; Ko, Y.; Kim, H.; Kim, J.; Kang, K., Reaction chemistry in rechargeable Li-O-2 batteries. *Chem. Soc. Rev.* **2017,** *46* (10), 2873-2888.

2. Littauer, E. L.; Tsai, K. C., Corrosion of Lithium in Alkaline Solution. *J. Electrochem. Soc.* **1977,** *124* (6), 850-855.

3. Lu, J.; Li, L.; Park, J. B.; Sun, Y. K.; Wu, F.; Amine, K., Aprotic and Aqueous Li-O-2 Batteries. *Chem. Rev.* **2014,** *114* (11), 5611-5640.

4. Li, F.; Zhang, T.; Zhou, H., Challenges of non-aqueous Li-O2 batteries: electrolytes, catalysts, and anodes. *Energy Environ. Sci.* **2013,** *6* (4), 1125-1141.

5. Lu, J.; Lee, Y. J.; Luo, X.; Lau, K. C.; Asadi, M.; Wang, H. H.; Brombosz, S.; Wen, J.; Zhai, D.; Chen, Z.; Miller, D. J.; Jeong, Y. S.; Park, J. B.; Fang, Z. Z.; Kumar, B.; Salehi-Khojin, A.; Sun, Y. K.; Curtiss, L. A.; Amine, K., A lithium-oxygen battery based on lithium superoxide. *Nature* **2016,** *529* (7586), 377-82.

6. Oh, D.; Qi, J.; Lu, Y. C.; Zhang, Y.; Shao-Horn, Y.; Belcher, A. M., Biologically enhanced cathode design for improved capacity and cycle life for lithium-oxygen batteries. *Nat Commun* **2013,** *4*, 2756.

7. Peng, Z.; Freunberger, S. A.; Chen, Y.; Bruce, P. G., A reversible and higher-rate Li-O2 battery. *Science* **2012,** *337* (6094), 563-6.

8. Johnson, L.; Li, C.; Liu, Z.; Chen, Y.; Freunberger, S. A.; Ashok, P. C.; Praveen, B. B.; Dholakia, K.; Tarascon, J. M.; Bruce, P. G., The role of LiO2 solubility in O2 reduction in aprotic solvents and its consequences for Li-O2 batteries. *Nat. Chem.* **2014,** *6* (12), 1091-9.

9. Aetukuri, N. B.; McCloskey, B. D.; García, J. M.; Krupp, L. E.; Viswanathan, V.; Luntz, A. C., Solvating additives drive solution-mediated electrochemistry and enhance toroid growth in non-aqueous Li–O2 batteries. *Nat. Chem.* **2014,** *7*, 50.

10. Schwenke, K. U.; Metzger, M.; Restle, T.; Piana, M.; Gasteiger, H. A., The Influence of Water and Protons on Li2O2 Crystal Growth in Aprotic Li-O2 Cells. *J. Electrochem. Soc.* **2015,** *162* (4), A573-A584.

11. Wu, S.; Tang, J.; Li, F.; Liu, X.; Yamauchi, Y.; Ishida, M.; Zhou, H., A Synergistic System for Lithium–Oxygen Batteries in Humid Atmosphere Integrating a Composite Cathode and a Hydrophobic Ionic Liquid-Based Electrolyte. *Adv. Funct. Mater.* **2016,** *26* (19), 3291-3298.

12. Li, F.; Wu, S.; Li, D.; Zhang, T.; He, P.; Yamada, A.; Zhou, H., The water catalysis at oxygen cathodes of lithium–oxygen cells. *Nature Communications* **2015,** *6*, 7843.

13. Wu, S.; Tang, J.; Li, F.; Liu, X.; Zhou, H., Low charge overpotentials in lithium–oxygen batteries based on tetraglyme electrolytes with a limited amount of water. *Chem. Commun.* **2015,** *51* (94), 16860-16863.

14. Adams, B. D.; Radtke, C.; Black, R.; Trudeau, M. L.; Zaghib, K.; Nazar, L. F., Current density dependence of peroxide formation in the Li–O2 battery and its effect on charge. *Energy Environ. Sci.* **2013,** *6* (6), 1772-1778.

15. Yilmaz, E.; Yogi, C.; Yamanaka, K.; Ohta, T.; Byon, H. R., Promoting Formation of Noncrystalline Li2O2 in the Li–O2 Battery with RuO2 Nanoparticles. *Nano Lett.* **2013,** *13* (10), 4679-4684.

16. Sankarasubramanian, S.; Singh, N.; Mizuno, F.; Prakash, J., Ab initio investigation of the oxygen reduction reaction activity on noble metal (Pt, Au, Pd), Pt3M (M = Fe, Co, Ni, Cu) and Pd3M (M = Fe, Co, Ni, Cu) alloy surfaces, for LiO2 cells. *J. Power Sources* **2016,** *319*, 202-209.

17. Yang, C.; Wong, R. A.; Hong, M.; Yamanaka, K.; Ohta, T.; Byon, H. R., Unexpected Li2O2 Film Growth on Carbon Nanotube Electrodes with CeO2 Nanoparticles in Li-O2 Batteries. *Nano Lett.* **2016,** *16* (5), 2969-2974.

18. Lacey, M. J.; Frith, J. T.; Owen, J. R., A redox shuttle to facilitate oxygen reduction in the lithium air battery. *Electrochem. Commun.* **2013,** *26*, 74-76.

19. Matsuda, S.; Hashimoto, K.; Nakanishi, S., Efficient Li2O2 Formation via Aprotic Oxygen Reduction Reaction Mediated by Quinone Derivatives. *The Journal of Physical Chemistry C* **2014,** *118* (32), 18397-18400.

20. Feng, N. N.; He, P.; Zhou, H. S., Critical Challenges in Rechargeable Aprotic Li-O-2 Batteries. *Advanced Energy Materials* **2016,** *6* (9).

21. Lau, S.; Archer, L. A., Nucleation and Growth of Lithium Peroxide in the Li–O2 Battery. *Nano Lett.* **2015,** *15* (9), 5995-6002.

22. Gallant, B. M.; Kwabi, D. G.; Mitchell, R. R.; Zhou, J.; Thompson, C. V.; Shao-Horn, Y., Influence of Li2O2 morphology on oxygen reduction and evolution kinetics in Li–O2 batteries. *Energy Environ. Sci.* **2013,** *6* (8), 2518-2528.

23. Gittleson, F. S.; Jones, R. E.; Ward, D. K.; Foster, M. E., Oxygen solubility and transport in Li–air battery electrolytes: establishing criteria and strategies for electrolyte design. *Energy Environ. Sci.* **2017,** *10* (5), 1167-1179.

24. Kushima, A.; Koido, T.; Fujiwara, Y.; Kuriyama, N.; Kusumi, N.; Li, J., Charging/Discharging Nanomorphology Asymmetry and Rate-Dependent Capacity Degradation in Li–Oxygen Battery. *Nano Lett.* **2015,** *15* (12), 8260-8265.

25. Zheng, H.; Xiao, D.; Li, X.; Liu, Y.; Wu, Y.; Wang, J.; Jiang, K.; Chen, C.; Gu, L.; Wei, X.; Hu, Y.-S.; Chen, Q.; Li, H., New Insight in Understanding Oxygen Reduction and Evolution in Solid-State Lithium–Oxygen Batteries Using an in Situ Environmental Scanning Electron Microscope. *Nano Lett.* **2014,** *14* (8), 4245-4249.

26. Lee, B.; Kim, J.; Yoon, G.; Lim, H.-D.; Choi, I.-S.; Kang, K., Theoretical Evidence for Low Charging Overpotentials of Superoxide Discharge Products in Metal–Oxygen Batteries. *Chem. Mater.* **2015,** *27* (24), 8406-8413.

27. Wang, J.; Zhang, Y.; Guo, L.; Wang, E.; Peng, Z., Identifying Reactive Sites and Transport Limitations of Oxygen Reactions in Aprotic Lithium-O2 Batteries at the Stage of Sudden Death. *Angew. Chem. Int. Ed.* **2016,** *55* (17), 5201-5205.

28. Varley, J. B.; Viswanathan, V.; Nørskov, J. K.; Luntz, A. C., Lithium and oxygen vacancies and their role in Li2O2 charge transport in Li–O2 batteries. *Energy Environ. Sci.* **2014,** *7* (2), 720-727.

29. Girishkumar, G.; McCloskey, B.; Luntz, A. C.; Swanson, S.; Wilcke, W., Lithium−Air Battery: Promise and Challenges. *The Journal of Physical Chemistry Letters* **2010,** *1* (14), 2193-2203.

30. Lim, H.-D.; Song, H.; Kim, J.; Gwon, H.; Bae, Y.; Park, K.-Y.; Hong, J.; Kim, H.; Kim, T.; Kim, Y. H.; Lepró, X.; Ovalle-Robles, R.; Baughman, R. H.; Kang, K., Superior Rechargeability and Efficiency of Lithium–Oxygen Batteries: Hierarchical Air Electrode Architecture Combined with a Soluble Catalyst. *Angew. Chem.* **2014,** *126* (15), 4007-4012.

31. Khetan, A.; Luntz, A.; Viswanathan, V., Trade-Offs in Capacity and Rechargeability in Nonaqueous Li–O2 Batteries: Solution-Driven Growth versus Nucleophilic Stability. *The Journal of Physical Chemistry Letters* **2015,** *6* (7), 1254-1259.

32. Radin, M. D.; Siegel, D. J., Charge transport in lithium peroxide: relevance for rechargeable metal–air batteries. *Energy Environ. Sci.* **2013,** *6* (8), 2370-2379.

33. Ganapathy, S.; Adams, B. D.; Stenou, G.; Anastasaki, M. S.; Goubitz, K.; Miao, X. F.; Nazar, L. F.; Wagemaker, M., Nature of Li2O2 oxidation in a Li-O2 battery revealed by operando X-ray diffraction. *J. Am. Chem. Soc.* **2014,** *136* (46), 16335-44.

34. Tian, F.; Radin, M.; Siegel, D., *Enhanced Charge Transport in Amorphous Li2O2*. **2014**; Vol. 26.

35. Jung, H.-G.; Kim, H.-S.; Park, J.-B.; Oh, I.-H.; Hassoun, J.; Yoon, C. S.; Scrosati, B.; Sun, Y.-K., A Transmission Electron Microscopy Study of the Electrochemical Process of Lithium–Oxygen Cells. *Nano Lett.* **2012,** *12* (8), 4333-4335.

36. Radin, M. D.; Monroe, C. W.; Siegel, D. J., How Dopants Can Enhance Charge Transport in Li2O2. *Chem. Mater.* **2015,** *27* (3), 839-847.

37. Kang, S.; Mo, Y.; Ong, S. P.; Ceder, G., A Facile Mechanism for Recharging Li2O2 in Li–O2 Batteries. *Chem. Mater.* **2013,** *25* (16), 3328-3336.

38. Lu, Y.-C.; Shao-Horn, Y., Probing the Reaction Kinetics of the Charge Reactions of Nonaqueous Li–O2 Batteries. *The Journal of Physical Chemistry Letters* **2013,** *4* (1), 93-99.

39. Lim, H.-D.; Song, H.; Kim, J.; Gwon, H.; Bae, Y.; Park, K.-Y.; Hong, J.; Kim, H.; Kim, T.; Kim, Y. H.; Lepró, X.; Ovalle-Robles, R.; Baughman, R. H.; Kang, K., Superior Rechargeability and Efficiency of Lithium–Oxygen Batteries: Hierarchical Air Electrode Architecture Combined with a Soluble Catalyst. *Angew. Chem. Int. Ed.* **2014,** *53* (15), 3926-3931.

40. Luntz, A. C.; Viswanathan, V.; Voss, J.; Varley, J. B.; Nørskov, J. K.; Scheffler, R.; Speidel, A., Tunneling and Polaron Charge Transport through Li2O2 in Li–O2 Batteries. *The Journal of Physical Chemistry Letters* **2013,** *4* (20), 3494-3499.

41. Zhang, Y.; Cui, Q.; Zhang, X.; McKee, W. C.; Xu, Y.; Ling, S.; Li, H.; Zhong, G.; Yang, Y.; Peng, Z., Amorphous Li2 O2 : Chemical Synthesis and Electrochemical Properties. *Angewandte Chemie (International ed. in English)* **2016,** *55* (36), 10717-10721.

42. Zhang, Y.; Qinghua, C.; Zhang, X.; C. McKee, W.; Xu, Y.; Ling, S.; Li, H.; Zhong, G.; Yang, Y.; Peng, Z., *Amorphous Li2O2: Chemical Synthesis and Electrochemical Properties*. **2016**.

43. Ottakam Thotiyl, M. M.; Freunberger, S. A.; Peng, Z.; Bruce, P. G., The Carbon Electrode in Nonaqueous Li–O2 Cells. *J. Am. Chem. Soc.* **2013,** *135* (1), 494-500.

44. Freunberger, S. A.; Chen, Y.; Peng, Z.; Griffin, J. M.; Hardwick, L. J.; Barde, F.; Novak, P.; Bruce, P. G., Reactions in the rechargeable lithium-O2 battery with alkyl carbonate electrolytes. *J. Am. Chem. Soc.* **2011,** *133* (20), 8040-7.

45. Wang, Z. L.; Xu, D.; Xu, J. J.; Zhang, L. L.; Zhang, X. B., Graphene Oxide Gel-Derived, Free-Standing, Hierarchically Porous Carbon for High-Capacity and High-Rate Rechargeable Li-O2 Batteries. *Adv. Funct. Mater.* **2012,** *22* (17), 3699-3705.

46. Borchardt, L.; Zhu, Q.-L.; Casco, M. E.; Berger, R.; Zhuang, X.; Kaskel, S.; Feng, X.; Xu, Q., Toward a molecular design of porous carbon materials. *Mater. Today* **2017,** *20* (10), 592-610.

47. Eftekhari, A.; Ramanujam, B., In pursuit of catalytic cathodes for lithium-oxygen batteries. *Journal of Materials Chemistry A* **2017,** *5* (17), 7710-7731.

48. Gadgil, B.; Damlin, P.; Kvarnström, C., Graphene vs. reduced graphene oxide: A comparative study of graphene-based nanoplatforms on electrochromic switching kinetics. *Carbon* **2016,** *96*, 377-381.

49. Sun, B.; Huang, X.; Chen, S.; Munroe, P.; Wang, G., Porous Graphene Nanoarchitectures: An Efficient Catalyst for Low Charge-Overpotential, Long Life, and High Capacity Lithium–Oxygen Batteries. *Nano Lett.* **2014,** *14* (6), 3145-3152.

50. Ozcan, S.; Cetinkaya, T.; Tokur, M.; Algul, H.; Guler, M. O.; Akbulut, H., Synthesis of flexible pure graphene papers and utilization as free standing cathodes for lithium-air batteries. *Int. J. Hydrogen Energy* **2016,** *41* (23), 9796-9802.

51. Wang, D.-W.; Li, F.; Liu, M.; Lu, G. Q.; Cheng, H.-M., 3D Aperiodic Hierarchical Porous Graphitic Carbon Material for High-Rate Electrochemical Capacitive Energy Storage. *Angew. Chem. Int. Ed.* **2008,** *47* (2), 373-376.

52. Sun, B.; Chen, S.; Liu, H.; Wang, G., Mesoporous Carbon Nanocube Architecture for High-Performance Lithium–Oxygen Batteries. *Adv. Funct. Mater.* **2015,** *25* (28), 4436-4444.

53. Zhao, C.; Yu, C.; Liu, S.; Yang, J.; Fan, X.; Huang, H.; Qiu, J., 3D Porous N-Doped Graphene Frameworks Made of Interconnected Nanocages for Ultrahigh-Rate and Long-Life Li-O2Batteries. *Adv. Funct. Mater.* **2015,** *25* (44), 6913-6920.

54. Park, J.-B.; Lee, J.; Yoon, C. S.; Sun, Y.-K., Ordered Mesoporous Carbon Electrodes for Li–O2 Batteries. *ACS Applied Materials & Interfaces* **2013,** *5* (24), 13426-13431.

55. Xie, J.; Yao, X.; Cheng, Q.; Madden, I. P.; Dornath, P.; Chang, C.-C.; Fan, W.; Wang, D., Three Dimensionally Ordered Mesoporous Carbon as a Stable, High-Performance Li–O2 Battery Cathode. *Angew. Chem. Int. Ed.* **2015,** *54* (14), 4299-4303.

56. Kim, B. G.; Jo, C.; Shin, J.; Mun, Y.; Lee, J.; Choi, J. W., Ordered Mesoporous Titanium Nitride as a Promising Carbon-Free Cathode for Aprotic Lithium-Oxygen Batteries. *ACS Nano* **2017,** *11* (2), 1736-1746.

57. Kim, D. Y.; Jin, X.; Lee, C. H.; Kim, D. W.; Suk, J.; Shon, J. K.; Kim, J. M.; Kang, Y., Improved electrochemical performance of ordered mesoporous carbon by incorporating macropores for Li–O2 battery cathode. *Carbon* **2018,** *133*, 118-126.

58. Park, J.; Jeong, J.; Lee, S.; Jo, C.; Lee, J., Effect of Mesoporous Structured Cathode Materials on Charging Potentials and Rate Capability of Lithium–Oxygen Batteries. *ChemSusChem* **2015,** *8* (18), 3146-3152.

59. Gong, K.; Du, F.; Xia, Z.; Durstock, M.; Dai, L., Nitrogen-Doped Carbon Nanotube Arrays with High Electrocatalytic Activity for Oxygen Reduction. *Science* **2009,** *323* (5915), 760-764.

60. Mi, R.; Liu, H.; Wang, H.; Wong, K.-W.; Mei, J.; Chen, Y.; Lau, W.-M.; Yan, H., Effects of nitrogen-doped carbon nanotubes on the discharge performance of Li-air batteries. *Carbon* **2014,** *67*, 744-752.

61. Xue, Y.; Liu, J.; Chen, H.; Wang, R.; Li, D.; Qu, J.; Dai, L., Nitrogen-Doped Graphene Foams as Metal-Free Counter Electrodes in High-Performance Dye-Sensitized Solar Cells. *Angew. Chem. Int. Ed.* **2012,** *51* (48), 12124-12127.

62. Li, Y.; Wang, J.; Li, X.; Geng, D.; Banis, M. N.; Li, R.; Sun, X., Nitrogen-doped graphene nanosheets as cathode materials with excellent electrocatalytic activity for high capacity lithium-oxygen batteries. *Electrochem. Commun.* **2012,** *18*, 12-15.

63. Li, Y.; Wang, J.; Li, X.; Liu, J.; Geng, D.; Yang, J.; Li, R.; Sun, X., Nitrogen-doped carbon nanotubes as cathode for lithium–air batteries. *Electrochem. Commun.* **2011,** *13* (7), 668-672.

64. Han, J.; Guo, X.; Ito, Y.; Liu, P.; Hojo, D.; Aida, T.; Hirata, A.; Fujita, T.; Adschiri, T.; Zhou, H.; Chen, M., Effect of Chemical Doping on Cathodic Performance of Bicontinuous Nanoporous Graphene for Li-O2 Batteries. *Advanced Energy Materials* **2016,** *6* (3), 1501870.

65. Wu, F.; Xing, Y.; Li, L.; Qian, J.; Qu, W.; Wen, J.; Miller, D.; Ye, Y.; Chen, R.; Amine, K.; Lu, J., Facile Synthesis of Boron-Doped rGO as Cathode Material for High Energy Li-O2 Batteries. *ACS Appl Mater Interfaces* **2016,** *8* (36), 23635-45.

66. Parvez, K.; Yang, S.; Hernandez, Y.; Winter, A.; Turchanin, A.; Feng, X.; Müllen, K., Nitrogen-Doped Graphene and Its Iron-Based Composite As Efficient Electrocatalysts for Oxygen Reduction Reaction. *ACS Nano* **2012,** *6* (11), 9541-9550.

67. Wu, G.; Santandreu, A.; Kellogg, W.; Gupta, S.; Ogoke, O.; Zhang, H.; Wang, H.-L.; Dai, L., Carbon nanocomposite catalysts for oxygen reduction and evolution reactions: From nitrogen doping to transition-metal addition. *Nano Energy* **2016,** *29*, 83-110.

68. Jung, C. Y.; Zhao, T. S.; Zeng, L.; Tan, P., Vertically aligned carbon nanotube-ruthenium dioxide core-shell cathode for non-aqueous lithium-oxygen batteries. *J. Power Sources* **2016,** *331*, 82-90.

69. Tan, P.; Shyy, W.; Wu, M. C.; Huang, Y. Y.; Zhao, T. S., Carbon electrode with NiO and RuO2 nanoparticles improves the cycling life of non-aqueous lithium-oxygen batteries. *J. Power Sources* **2016,** *326*, 303-312.

70. Guo, Z.; Zhou, D.; Liu, H.; Dong, X.; Yuan, S.; Yu, A.; Wang, Y.; Xia, Y., Synthesis of ruthenium oxide coated ordered mesoporous carbon nanofiber arrays as a catalyst for lithium oxygen battery. *J. Power Sources* **2015,** *276*, 181-188.

71. Liu, Z. X.; De Jesus, L. R.; Banerjee, S.; Mukherjee, P. P., Mechanistic Evaluation of LixOy Formation on delta-MnO2 in Nonaqueous Li-Air Batteries. *Acs Applied Materials & Interfaces* **2016,** *8* (35), 23028-23036.

72. Wei, Z. H.; Zhao, T. S.; Zhu, X. B.; Tan, P., MnO2-x nanosheets on stainless steel felt as a carbon- and binder-free cathode for non-aqueous lithium-oxygen batteries. *J. Power Sources* **2016,** *306*, 724-732.

73. Débart, A.; Paterson, A. J.; Bao, J.; Bruce, P. G., α-MnO2 Nanowires: A Catalyst for the O2 Electrode in Rechargeable Lithium Batteries. *Angew. Chem. Int. Ed.* **2008,** *47* (24), 4521-4524.

74. Cao, Y. L.; Yang, H. X.; Ai, X. P.; Xiao, L. F., The mechanism of oxygen reduction on MnO2-catalyzed air cathode in alkaline solution. *J. Electroanal. Chem.* **2003,** *557*, 127-134.

75. McCloskey, B. D.; Scheffler, R.; Speidel, A.; Bethune, D. S.; Shelby, R. M.; Luntz, A. C., On the Efficacy of Electrocatalysis in Nonaqueous Li–O2 Batteries. *J. Am. Chem. Soc.* **2011,** *133* (45), 18038-18041.

76. Thapa, A. K.; Ishihara, T., Mesoporous α-MnO2/Pd catalyst air electrode for rechargeable lithium–air battery. *J. Power Sources* **2011,** *196* (16), 7016-7020.

77. Huang, Z.; Zhang, M.; Cheng, J.; Gong, Y.; Li, X.; Chi, B.; Pu, J.; Jian, L., Silver decorated beta-manganese oxide nanorods as an effective cathode electrocatalyst for rechargeable lithium–oxygen battery. *J. Alloys Compd.* **2015,** *626*, 173-179.

78. Zhang, P.; Sun, D.; He, M.; Lang, J.; Xu, S.; Yan, X., Synthesis of Porous δ-MnO2 Submicron Tubes as Highly Efficient Electrocatalyst for Rechargeable Li–O2 Batteries. *ChemSusChem* **2015,** *8* (11), 1972-1979.

79. Zhang, P.; Sun, D.; He, M.; Lang, J.; Xu, S.; Yan, X., *Synthesis of Porous δ-MnO2 Submicron Tubes as Highly Efficient Electrocatalyst for Rechargeable Li–O2 Batteries.* **2015**; Vol. 8.

80. Cheng, F.; Zhang, T.; Zhang, Y.; Du, J.; Han, X.; Chen, J., Enhancing Electrocatalytic Oxygen Reduction on MnO2 with Vacancies. *Angew. Chem. Int. Ed.* **2013,** *52* (9), 2474-2477.

81. Tompsett, D. A.; Parker, S. C.; Islam, M. S., Rutile (β-)MnO2 Surfaces and Vacancy Formation for High Electrochemical and Catalytic Performance. *J. Am. Chem. Soc.* **2014,** *136* (4), 1418-1426.

82. Débart, A.; Bao, J.; Armstrong, G.; Bruce, P. G., An O2 cathode for rechargeable lithium batteries: The effect of a catalyst. *J. Power Sources* **2007,** *174* (2), 1177-1182.

83. Lin, X.; Shang, Y.; Li, L.; Yu, A., Sea-Urchin-like Cobalt Oxide Grown on Nickel Foam as a Carbon-Free Electrode for Lithium–Oxygen Batteries. *ACS Sustainable Chemistry & Engineering* **2015,** *3* (5), 903-908.

84. Gnana kumar, G.; Christy, M.; Jang, H.; Nahm, K. S., Cobaltite oxide nanosheets anchored graphene nanocomposite as an efficient oxygen reduction reaction (ORR) catalyst for the application of lithium-air batteries. *J. Power Sources* **2015,** *288*, 451-460.

85. Li, Z.; Yu, X.-Y.; Paik, U., Facile preparation of porous Co3O4 nanosheets for high-performance lithium ion batteries and oxygen evolution reaction. *J. Power Sources* **2016,** *310*, 41-46.

86. Shang, C.; Dong, S.; Hu, P.; Guan, J.; Xiao, D.; Chen, X.; Zhang, L.; Gu, L.; Cui, G.; Chen, L., Compatible interface design of CoO-based Li-O2 battery cathodes with long-cycling stability. *Sci. Rep.* **2015,** *5*, 8335.

87. Zhang, P.; Wang, R.; He, M.; Lang, J.; Xu, S.; Yan, X., 3D Hierarchical Co/CoO-Graphene-Carbonized Melamine Foam as a Superior Cathode toward Long-Life Lithium Oxygen Batteries. *Adv. Funct. Mater.* **2016,** *26* (9), 1354-1364.

88. Liu, Q.-C.; Xu, J.-J.; Xu, D.; Zhang, X.-B., Flexible lithium–oxygen battery based on a recoverable cathode. *Nature Communications* **2015,** *6*, 7892.

89. Kang, S. H.; Song, K.; Jung, J.; Jo, M. R.; Kang, Y.-M., Polymorphism-induced catalysis difference of TiO2 nanofibers for rechargeable Li–O2 batteries. *Journal of Materials Chemistry A* **2014,** *2* (46), 19660-19664.

90. Geng, W. T.; Ohno, T., Li2O2 Wetting on the (110) Surface of RuO2, TiO2, and SnO2: An Initiating Force for Polycrystalline Growth. *The Journal of Physical Chemistry C* **2015,** *119* (2), 1024-1031.

91. Kundu, D.; Black, R.; Berg, E. J.; Nazar, L. F., A highly active nanostructured metallic oxide cathode for aprotic Li–O2 batteries. *Energy Environ. Sci.* **2015,** *8* (4), 1292-1298.

92. Zhang, W.; Zeng, Y.; Xu, C.; Tan, H.; Liu, W.; Zhu, J.; Xiao, N.; Hng, H. H.; Ma, J.; Hoster, H. E.; Yazami, R.; Yan, Q., Fe2O3 nanocluster-decorated graphene as O2 electrode for high energy Li–O2 batteries. *RSC Advances* **2012,** *2* (22), 8508-8514.

93. Lu, J.; Qin, Y.; Du, P.; Luo, X.; Wu, T.; Ren, Y.; Wen, J.; Miller, D. J.; Miller, J. T.; Amine, K., Synthesis and characterization of uniformly dispersed Fe3O4/Fe nanocomposite on porous carbon: application for rechargeable Li–O2 batteries. *RSC Advances* **2013,** *3* (22), 8276-8285.

94. Hung, T.-F.; Mohamed, S. G.; Shen, C.-C.; Tsai, Y.-Q.; Chang, W.-S.; Liu, R.-S., Mesoporous ZnCo2O4 nanoflakes with bifunctional electrocatalytic activities toward efficiencies of rechargeable lithium–oxygen batteries in aprotic media. *Nanoscale* **2013,** *5* (24), 12115-12119.

95. Şener, T.; Kayhan, E.; Sevim, M.; Metin, Ö., Monodisperse CoFe2O4 nanoparticles supported on Vulcan XC-72: High performance electrode materials for lithium-air and lithium-ion batteries. *J. Power Sources* **2015,** *288*, 36-41.

96. Wang, L.; Zhao, X.; Lu, Y.; Xu, M.; Zhang, D.; Ruoff, R. S.; Stevenson, K. J.; Goodenough, J. B., CoMn2O4 Spinel Nanoparticles Grown on Graphene as Bifunctional Catalyst for Lithium-Air Batteries. *J. Electrochem. Soc.* **2011,** *158* (12), A1379-A1382.

97. Suntivich, J.; Gasteiger, H. A.; Yabuuchi, N.; Nakanishi, H.; Goodenough, J. B.; Shao-Horn, Y., Design principles for oxygen-reduction activity on perovskite oxide catalysts for fuel cells and metal–air batteries. *Nat. Chem.* **2011,** *3*, 546.

98. Liu, G.; Chen, H.; Xia, L.; Wang, S.; Ding, L.-X.; Li, D.; Xiao, K.; Dai, S.; Wang, H., Hierarchical Mesoporous/Macroporous Perovskite La0.5Sr0.5CoO3–x Nanotubes: A Bifunctional Catalyst with Enhanced Activity and Cycle Stability for Rechargeable Lithium Oxygen Batteries. *ACS Applied Materials & Interfaces* **2015,** *7* (40), 22478-22486.

99. Cheng, J.; Zhang, M.; Jiang, Y.; Zou, L.; Gong, Y.; Chi, B.; Pu, J.; Jian, L., Perovskite La0.6Sr0.4Co0.2Fe0.8O3 as an effective electrocatalyst for non-aqueous lithium air batteries. *Electrochim. Acta* **2016,** *191*, 106-115.

100. Park, J.; Jun, Y.-S.; Lee, W.-r.; Gerbec, J. A.; See, K. A.; Stucky, G. D., Bimodal Mesoporous Titanium Nitride/Carbon Microfibers as Efficient and Stable Electrocatalysts for Li–O2 Batteries. *Chem. Mater.* **2013,** *25* (19), 3779-3781.

101. Riaz, A.; Jung, K.-N.; Chang, W.; Shin, K.-H.; Lee, J.-W., Carbon-, Binder-, and Precious Metal-Free Cathodes for Non-Aqueous Lithium–Oxygen Batteries: Nanoflake-Decorated Nanoneedle Oxide Arrays. *ACS Applied Materials & Interfaces* **2014,** *6* (20), 17815-17822.

102. Li, Z.; Chen, C.; Zhan, E.; Ta, N.; Li, Y.; Shen, W., Crystal-phase control of molybdenum carbide nanobelts for dehydrogenation of benzyl alcohol. *Chem. Commun.* **2014,** *50* (34), 4469-4471.

103. Wan, C.; Regmi, Y. N.; Leonard, B. M., Multiple Phases of Molybdenum Carbide as Electrocatalysts for the Hydrogen Evolution Reaction. *Angew. Chem. Int. Ed.* **2014,** *53* (25), 6407-6410.

104. Ottakam Thotiyl, M. M.; Freunberger, S. A.; Peng, Z.; Chen, Y.; Liu, Z.; Bruce, P. G., A stable cathode for the aprotic Li–O2 battery. *Nature Materials* **2013,** *12*, 1050.

105. Adams, B. D.; Black, R.; Radtke, C.; Williams, Z.; Mehdi, B. L.; Browning, N. D.; Nazar, L. F., The Importance of Nanometric Passivating Films on Cathodes for Li–Air Batteries. *ACS Nano* **2014,** *8* (12), 12483-12493.

106. Zhang, H.-J.; Wang, K.-X.; Wu, X.-Y.; Jiang, Y.-M.; Zhai, Y.-B.; Wang, C.; Wei, X.; Chen, J.-S., MoO2/Mo2C Heteronanotubes Function as High-Performance Li-Ion Battery Electrode. *Adv. Funct. Mater.* **2014,** *24* (22), 3399-3404.

107. Xia, G.; Liu, D.; Zheng, F.; Yang, Y.; Su, J.; Chen, Q., Preparation of porous MoO2@C nano-octahedrons from a polyoxometalate-based metal–organic framework for highly reversible lithium storage. *Journal of Materials Chemistry A* **2016,** *4* (32), 12434-12441.

108. Luo, Y.; Jin, C.; Wang, Z.; Wei, M.; Yang, C.; Yang, R.; Chen, Y.; Liu, M., A high-performance oxygen electrode for Li–O2 batteries: Mo2C nanoparticles grown on carbon fibers. *Journal of Materials Chemistry A* **2017,** *5* (12), 5690-5695.

109. Kundu, D.; Black, R.; Adams, B.; Harrison, K.; Zavadil, K.; Nazar, L. F., Nanostructured Metal Carbides for Aprotic Li–O2 Batteries: New Insights into Interfacial Reactions and Cathode Stability. *The Journal of Physical Chemistry Letters* **2015,** *6* (12), 2252-2258.

110. Wang, Y.; Ohnishi, R.; Yoo, E.; He, P.; Kubota, J.; Domen, K.; Zhou, H., Nano- and micro-sized TiN as the electrocatalysts for ORR in Li–air fuel cell with alkaline aqueous electrolyte. *J. Mater. Chem.* **2012,** *22* (31), 15549-15555.

111. Zhang, K.; Zhang, L.; Chen, X.; He, X.; Wang, X.; Dong, S.; Gu, L.; Liu, Z.; Huang, C.; Cui, G., Molybdenum Nitride/N-Doped Carbon Nanospheres for Lithium-O2 Battery Cathode Electrocatalyst. *ACS Applied Materials & Interfaces* **2013,** *5* (9), 3677-3682.

112. Ningthoujam, R. S.; Gajbhiye, N. S., Synthesis, electron transport properties of transition metal nitrides and applications. *Prog. Mater Sci.* **2015,** *70*, 50-154.

113. Xu, S.-M.; Zhu, Q.-C.; Harris, M.; Chen, T.-H.; Ma, C.; Wei, X.; Xu, H.-S.; Zhou, Y.-X.; Cao, Y.-C.; Wang, K.-X.; Chen, J.-S., Toward Lower Overpotential through Improved Electron Transport Property: Hierarchically Porous CoN Nanorods Prepared by Nitridation for Lithium–Oxygen Batteries. *Nano Lett.* **2016,** *16* (9), 5902-5908.

114. Wang, K.-X.; Zhu, Q.-C.; Chen, J.-S., Strategies toward High-Performance Cathode Materials for Lithium–Oxygen Batteries. *Small* **2018,** *14* (27), 1800078.

115. Wang, Z. L.; Xu, D.; Xu, J. J.; Zhang, X. B., Oxygen electrocatalysts in metal-air batteries: from aqueous to nonaqueous electrolytes. *Chem. Soc. Rev.* **2014,** *43* (22), 7746-7786.

116. Song, K.; Agyeman, D. A.; Jung, J.; Jo, M. R.; Yang, J.; Kang, Y.-M., A Review of the Design Strategies for Tailored Cathode Catalyst Materials in Rechargeable Li-O2 Batteries. *Isr. J. Chem.* **2015,** *55* (5), 458-471.

117. Shen, Y.; Sun, D.; Yu, L.; Zhang, W.; Shang, Y.; Tang, H.; Wu, J.; Cao, A.; Huang, Y., A high-capacity lithium–air battery with Pd modified carbon nanotube sponge cathode working in regular air. *Carbon* **2013,** *62*, 288-295.

118. Lu, Y.-C.; Gasteiger, H. A.; Shao-Horn, Y., Catalytic Activity Trends of Oxygen Reduction Reaction for Nonaqueous Li-Air Batteries. *J. Am. Chem. Soc.* **2011,** *133* (47), 19048-19051.

119. Ko, B. K.; Kim, M. K.; Kim, S. H.; Lee, M. A.; Shim, S. E.; Baeck, S.-H., Synthesis and electrocatalytic properties of various metals supported on carbon for lithium–air battery. *J. Mol. Catal. A: Chem.* **2013,** *379*, 9-14.

120. Su, D. W.; Dou, S. X.; Wang, G. X., Hierarchical Ru nanospheres as highly effective cathode catalysts for Li–O2 batteries. *Journal of Materials Chemistry A* **2015,** *3* (36), 18384-18388.

121. Park, J.-B.; Luo, X.; Lu, J.; Shin, C. D.; Yoon, C. S.; Amine, K.; Sun, Y.-K., Improvement of Electrochemical Properties of Lithium–Oxygen Batteries Using a Silver Electrode. *The Journal of Physical Chemistry C* **2015,** *119* (27), 15036-15040.

122. Lee, M.; Hwang, Y.; Yun, K.-H.; Chung, Y.-C., Greatly improved electrochemical performance of lithium–oxygen batteries with a bimetallic platinum–copper alloy catalyst. *J. Power Sources* **2015,** *288*, 296-301.

123. Freunberger, S.; Chen, Y.; Bardé, F.; Takechi, K.; Mizuno, F.; Bruce, P., Nonaqueous Electrolytes. In *The Lithium Air Battery*, Imanishi, N.; Luntz, A. C.; Bruce, P., Eds. Springer New York: **2014**; Chapter 2, pp 23-58.

124. Laoire, C. O.; Mukerjee, S.; Abraham, K. M.; Plichta, E. J.; Hendrickson, M. A., Influence of Nonaqueous Solvents on the Electrochemistry of Oxygen in the Rechargeable Lithium−Air Battery. *The Journal of Physical Chemistry C* **2010,** *114* (19), 9178-9186.

125. Laoire, C.; Mukerjee, S.; Plichta, E. J.; Hendrickson, M. A.; Abraham, K. M., Rechargeable Lithium/TEGDME- LiPF6 ／ O2 Battery. *J. Electrochem. Soc.* **2011,** *158* (3), A302-A308.

126. Freunberger, S. A.; Chen, Y.; Drewett, N. E.; Hardwick, L. J.; Bardé, F.; Bruce, P. G., The Lithium–Oxygen Battery with Ether-Based Electrolytes. *Angew. Chem. Int. Ed.* **2011,** *50* (37), 8609-8613.

127. McCloskey, B. D.; Bethune, D. S.; Shelby, R. M.; Girishkumar, G.; Luntz, A. C., Solvents' Critical Role in Nonaqueous Lithium–Oxygen Battery Electrochemistry. *The Journal of Physical Chemistry Letters* **2011,** *2* (10), 1161-1166.

128. Hassoun, J.; Croce, F.; Armand, M.; Scrosati, B., Investigation of the O2 Electrochemistry in a Polymer Electrolyte Solid-State Cell. *Angew. Chem. Int. Ed.* **2011,** *50* (13), 2999-3002.

129. Bryantsev, V. S.; Faglioni, F., Predicting Autoxidation Stability of Ether- and Amide-Based Electrolyte Solvents for Li–Air Batteries. *The Journal of Physical Chemistry A* **2012,** *116* (26), 7128-7138.

130. Bryantsev, V. S.; Uddin, J.; Giordani, V.; Walker, W.; Addison, D.; Chase, G. V., The Identification of Stable Solvents for Nonaqueous Rechargeable Li-Air Batteries. *J. Electrochem. Soc.* **2013,** *160* (1), A160-A171.

131. Sun, X.-G.; Angell, C. A., New sulfone electrolytes for rechargeable lithium batteries.: Part I. Oligoether-containing sulfones. *Electrochem. Commun.* **2005,** *7* (3), 261-266.

132. Mozhzhukhina, N.; Méndez De Leo, L. P.; Calvo, E. J., Infrared Spectroscopy Studies on Stability of Dimethyl Sulfoxide for Application in a Li–Air Battery. *The Journal of Physical Chemistry C* **2013,** *117* (36), 18375-18380.

133. Chen, Y.; Freunberger, S. A.; Peng, Z.; Fontaine, O.; Bruce, P. G., Charging a Li–O2 battery using a redox mediator. *Nat. Chem.* **2013,** *5* (6), 489-494.

134. Peng, Z.; Freunberger, S. A.; Chen, Y.; Bruce, P. G., A Reversible and Higher-Rate Li-O2 Battery. *Science* **2012,** *337* (6094), 563-566.

135. Stark, A.; Seddon, K. R., Ionic Liquids. In *Kirk-Othmer Encyclopedia of Chemical Technology*, John Wiley & Sons, Inc.: **2000**.

136. Kuboki, T.; Okuyama, T.; Ohsaki, T.; Takami, N., Lithium-air batteries using hydrophobic room temperature ionic liquid electrolyte. *J. Power Sources* **2005,** *146* (1–2), 766-769.

137. Monaco, S.; Arangio, A. M.; Soavi, F.; Mastragostino, M.; Paillard, E.; Passerini, S., An electrochemical study of oxygen reduction in pyrrolidinium-based ionic liquids for lithium/oxygen batteries. *Electrochim. Acta* **2012,** *83*, 94-104.

138. Soavi, F.; Monaco, S.; Mastragostino, M., Catalyst-free porous carbon cathode and ionic liquid for high efficiency, rechargeable Li/O-2 battery. *J. Power Sources* **2013,** *224*, 115-119.

139. Elia, G. A.; Hassoun, J.; Kwak, W. J.; Sun, Y. K.; Scrosati, B.; Mueller, F.; Bresser, D.; Passerini, S.; Oberhumer, P.; Tsiouvaras, N.; Reiter, J., An Advanced Lithium-Air Battery Exploiting an Ionic Liquid-Based Electrolyte. *Nano Lett.* **2014,** *14* (11), 6572-6577.

140. Elia, G. A.; Park, J.-B.; Sun, Y.-K.; Scrosati, B.; Hassoun, J., Role of the Lithium Salt in the Performance of Lithium–Oxygen Batteries: A Comparative Study. *ChemElectroChem* **2014,** *1* (1), 47-50.

141. Oswald, S.; Mikhailova, D.; Scheiba, F.; Reichel, P.; Fiedler, A.; Ehrenberg, H., XPS investigations of electrolyte/electrode interactions for various Li-ion battery materials. *Anal. Bioanal. Chem.* **2011,** *400* (3), 691-696.

142. Du, P.; Lu, J.; Lau, K. C.; Luo, X.; Bareño, J.; Zhang, X.; Ren, Y.; Zhang, Z.; Curtiss, L. A.; Sun, Y.-K.; Amine, K., Compatibility of lithium salts with solvent of the non-aqueous electrolyte in Li–O2 batteries. *PCCP* **2013,** *15* (15), 5572-5581.

143. McCloskey, B. D.; Scheffler, R.; Speidel, A.; Girishkumar, G.; Luntz, A. C., On the Mechanism of Nonaqueous Li–O2 Electrochemistry on C and Its Kinetic Overpotentials: Some Implications for Li–Air Batteries. *The Journal of Physical Chemistry C* **2012,** *116* (45), 23897-23905.

144. Chaolumen Wu, C.-B. L., Lei Li, Jun Yang, Ethylene sulfite based electrolyte for non-aqueous lithium oxygen batteries. *Chin. Chem. Lett.* **2016,** (27(9)), 1485-1489.

145. Novoselov, K. S.; Geim, A. K.; Morozov, S. V.; Jiang, D.; Zhang, Y.; Dubonos, S. V.; Grigorieva, I. V.; Firsov, A. A., Electric Field Effect in Atomically Thin Carbon Films. *Science* **2004,** *306* (5696), 666-669.

146. LXXXVI. On the combinations of carbon with silicon and iron, and other metals, forming the different species of cast iron, steel, and malleable iron AU - Schafhaeutl, C. *The London, Edinburgh, and Dublin Philosophical Magazine and Journal of Science* **1840,** *16* (106), 570-590.

147. Brodie, B. C., *On the atomic weight of graphite* **1859**, 249-259.

148. Hummers, W. S.; Offeman, R. E., Preparation of Graphitic Oxide. *J. Am. Chem. Soc.* **1958,** *80* (6), 1339-1339.

149. Zhao, J.; Pei, S.; Ren, W.; Gao, L.; Cheng, H.-M., Efficient Preparation of Large-Area Graphene Oxide Sheets for Transparent Conductive Films. *ACS Nano* **2010,** *4* (9), 5245-5252.

150. Hirata, M.; Gotou, T.; Horiuchi, S.; Fujiwara, M.; Ohba, M., Thin-film particles of graphite oxide 1:: High-yield synthesis and flexibility of the particles. *Carbon* **2004,** *42* (14), 2929-2937.

151. Marcano, D. C.; Kosynkin, D. V.; Berlin, J. M.; Sinitskii, A.; Sun, Z.; Slesarev, A.; Alemany, L. B.; Lu, W.; Tour, J. M., Improved Synthesis of Graphene Oxide. *ACS Nano* **2010,** *4* (8), 4806-4814.

152. Pei, S.; Cheng, H.-M., The reduction of graphene oxide. *Carbon* **2012,** *50* (9), 3210-3228.

153. Kudin, K. N.; Ozbas, B.; Schniepp, H. C.; Prud'homme, R. K.; Aksay, I. A.; Car, R., Raman Spectra of Graphite Oxide and Functionalized Graphene Sheets. *Nano Lett.* **2008,** *8* (1), 36-41.

154. Schniepp, H. C.; Li, J.-L.; McAllister, M. J.; Sai, H.; Herrera-Alonso, M.; Adamson, D. H.; Prud'homme, R. K.; Car, R.; Saville, D. A.; Aksay, I. A., Functionalized Single Graphene Sheets Derived from Splitting Graphite Oxide. *The Journal of Physical Chemistry B* **2006,** *110* (17), 8535-8539.

155. Becerril, H. A.; Mao, J.; Liu, Z.; Stoltenberg, R. M.; Bao, Z.; Chen, Y., Evaluation of Solution-Processed Reduced Graphene Oxide Films as Transparent Conductors. *ACS Nano* **2008,** *2* (3), 463-470.

156. Wang, X.; Zhi, L.; Müllen, K., Transparent, Conductive Graphene Electrodes for Dye-Sensitized Solar Cells. *Nano Lett.* **2008,** *8* (1), 323-327.

157. Wu, Z.-S.; Ren, W.; Gao, L.; Zhao, J.; Chen, Z.; Liu, B.; Tang, D.; Yu, B.; Jiang, C.; Cheng, H.-M., Synthesis of Graphene Sheets with High Electrical Conductivity and Good Thermal Stability by Hydrogen Arc Discharge Exfoliation. *ACS Nano* **2009,** *3* (2), 411-417.

158. Zhu, Y.; Murali, S.; Stoller, M. D.; Velamakanni, A.; Piner, R. D.; Ruoff, R. S., Microwave assisted exfoliation and reduction of graphite oxide for ultracapacitors. *Carbon* **2010,** *48* (7), 2118-2122.

159. Zhang, Y.; Guo, L.; Wei, S.; He, Y.; Xia, H.; Chen, Q.; Sun, H.-B.; Xiao, F.-S., Direct imprinting of microcircuits on graphene oxides film by femtosecond laser reduction. *Nano Today* **2010,** *5* (1), 15-20.

160. Cote, L. J.; Cruz-Silva, R.; Huang, J., Flash Reduction and Patterning of Graphite Oxide and Its Polymer Composite. *J. Am. Chem. Soc.* **2009,** *131* (31), 11027-11032.

161. Kotov, N. A.; Dékány, I.; Fendler, J. H., Ultrathin graphite oxide–polyelectrolyte composites prepared by self-assembly: Transition between conductive and non-conductive states. *Adv. Mater.* **1996,** *8* (8), 637-641.

162. Fernández-Merino, M. J.; Guardia, L.; Paredes, J. I.; Villar-Rodil, S.; Solís-Fernández, P.; Martínez-Alonso, A.; Tascón, J. M. D., Vitamin C Is an Ideal Substitute for Hydrazine in the Reduction of Graphene Oxide Suspensions. *The Journal of Physical Chemistry C* **2010,** *114* (14), 6426-6432.

163. Shin, H.-J.; Kim, K. K.; Benayad, A.; Yoon, S.-M.; Park, H. K.; Jung, I.-S.; Jin, M. H.; Jeong, H.-K.; Kim, J. M.; Choi, J.-Y.; Lee, Y. H., Efficient Reduction of Graphite Oxide by Sodium Borohydride and Its Effect on Electrical Conductance. *Adv. Funct. Mater.* **2009,** *19* (12), 1987-1992.

164. Moon, J. Y.; Tuokko, I.; Suominen, A.; Tuominen, A.; Oh, D. S.; Park, B. K.; Kim, H. In *Hydrogen sensing performance of TiO<inf>2</inf> nanotubes at room temperature*, 2010 12th Biennial Baltic Electronics Conference, 4-6 Oct. 2010; **2010**; pp 73-76.

165. Wang, H.; Maiyalagan, T.; Wang, X., Review on Recent Progress in Nitrogen-Doped Graphene: Synthesis, Characterization, and Its Potential Applications. *ACS Catalysis* **2012,** *2* (5), 781-794.

166. Inagaki, M.; Toyoda, M.; Soneda, Y.; Morishita, T., Nitrogen-doped carbon materials. *Carbon* **2018,** *132*, 104-140.

167. Wei, D.; Liu, Y.; Wang, Y.; Zhang, H.; Huang, L.; Yu, G., Synthesis of N-Doped Graphene by Chemical Vapor Deposition and Its Electrical Properties. *Nano Lett.* **2009,** *9* (5), 1752-1758.

168. Xue, Y.; Wu, B.; Jiang, L.; Guo, Y.; Huang, L.; Chen, J.; Tan, J.; Geng, D.; Luo, B.; Hu, W.; Yu, G.; Liu, Y., Low Temperature Growth of Highly Nitrogen-Doped Single Crystal Graphene Arrays by Chemical Vapor Deposition. *J. Am. Chem. Soc.* **2012,** *134* (27), 11060-11063.

169. Di, C.-a.; Wei, D.; Yu, G.; Liu, Y.; Guo, Y.; Zhu, D., Patterned Graphene as Source/Drain Electrodes for Bottom-Contact Organic Field-Effect Transistors. *Adv. Mater.* **2008,** *20* (17), 3289-3293.

170. Bai, J.; Zhu, Q.; Lv, Z.; Dong, H.; Yu, J.; Dong, L., Nitrogen-doped graphene as catalysts and catalyst supports for oxygen reduction in both acidic and alkaline solutions. *Int. J. Hydrogen Energy* **2013,** *38* (3), 1413-1418.

171. Choi, C. H.; Park, S. H.; Chung, M. W.; Woo, S. I., Easy and controlled synthesis of nitrogen-doped carbon. *Carbon* **2013,** *55*, 98-107.

172. Xu, H.; Ma, L.; Jin, Z., Nitrogen-doped graphene: Synthesis, characterizations and energy applications. *Journal of Energy Chemistry* **2018,** *27* (1), 146-160.

173. Li, N.; Wang, Z.; Zhao, K.; Shi, Z.; Gu, Z.; Xu, S., Large scale synthesis of N-doped multi-layered graphene sheets by simple arc-discharge method. *Carbon* **2010,** *48* (1), 255-259.
174. Guan, L.; Cui, L.; Lin, K.; Wang, Y. Y.; Wang, X. T.; Jin, F. M.; He, F.; Chen, X. P.; Cui, S., Preparation of few-layer nitrogen-doped graphene nanosheets by DC arc discharge under nitrogen atmosphere of high temperature. *Appl. Phys. A* **2011,** *102* (2), 289-294.
175. Zhang, C.; Fu, L.; Liu, N.; Liu, M.; Wang, Y.; Liu, Z., Synthesis of Nitrogen-Doped Graphene Using Embedded Carbon and Nitrogen Sources. *Adv. Mater.* **2011,** *23* (8), 1020-1024.
176. Qu, K.; Zheng, Y.; Dai, S.; Qiao, S. Z., Polydopamine-graphene oxide derived mesoporous carbon nanosheets for enhanced oxygen reduction. *Nanoscale* **2015,** *7* (29), 12598-12605.
177. Bai, S.; Shen, X.; Zhu, G.; Li, M.; Xi, H.; Chen, K., In situ Growth of NixCo100–x Nanoparticles on Reduced Graphene Oxide Nanosheets and Their Magnetic and Catalytic Properties. *ACS Applied Materials & Interfaces* **2012,** *4* (5), 2378-2386.
178. Golberg, D.; Bando, Y.; Bourgeois, L.; Kurashima, K.; Sato, T., Large-scale synthesis and HRTEM analysis of single-walled B- and N-doped carbon nanotube bundles. *Carbon* **2000,** *38* (14), 2017-2027.
179. Wang, Y.; Shao, Y.; Matson, D. W.; Li, J.; Lin, Y., Nitrogen-Doped Graphene and Its Application in Electrochemical Biosensing. *ACS Nano* **2010,** *4* (4), 1790-1798.
180. Jeong, H. M.; Lee, J. W.; Shin, W. H.; Choi, Y. J.; Shin, H. J.; Kang, J. K.; Choi, J. W., Nitrogen-Doped Graphene for High-Performance Ultracapacitors and the Importance of Nitrogen-Doped Sites at Basal Planes. *Nano Lett.* **2011,** *11* (6), 2472-2477.
181. Yang, D.; Velamakanni, A.; Bozoklu, G.; Park, S.; Stoller, M.; Piner, R. D.; Stankovich, S.; Jung, I.; Field, D. A.; Ventrice, C. A.; Ruoff, R. S., Chemical analysis of graphene oxide films after heat and chemical treatments by X-ray photoelectron and Micro-Raman spectroscopy. *Carbon* **2009,** *47* (1), 145-152.
182. Xiong, B.; Zhou, Y.; O'Hayre, R.; Shao, Z., Facile single-step ammonia heat-treatment and quenching process for the synthesis of improved Pt/N-graphene catalysts. *Appl. Surf. Sci.* **2013,** *266*, 433-439.
183. Geng, D.; Yang, S.; Zhang, Y.; Yang, J.; Liu, J.; Li, R.; Sham, T.-K.; Sun, X.; Ye, S.; Knights, S., Nitrogen doping effects on the structure of graphene. *Appl. Surf. Sci.* **2011,** *257* (21), 9193-9198.
184. Gardiner, D. J., Introduction to Raman Scattering. In *Practical Raman Spectroscopy*, Gardiner, D. J.; Graves, P. R., Eds. Springer Berlin Heidelberg: Berlin, Heidelberg, **1989**, pp 1-12.

185. Luo, Z.; Lim, S.; Tian, Z.; Shang, J.; Lai, L.; MacDonald, B.; Fu, C.; Shen, Z.; Yu, T.; Lin, J., Pyridinic N doped graphene: synthesis, electronic structure, and electrocatalytic property. *J. Mater. Chem.* **2011,** *21* (22), 8038-8044.

186. Deng, D.; Pan, X.; Yu, L.; Cui, Y.; Jiang, Y.; Qi, J.; Li, W.-X.; Fu, Q.; Ma, X.; Xue, Q.; Sun, G.; Bao, X., Toward N-Doped Graphene via Solvothermal Synthesis. *Chem. Mater.* **2011,** *23* (5), 1188-1193.

187. Qu, K.; Zheng, Y.; Dai, S.; Qiao, S. Z., Graphene oxide-polydopamine derived N, S-codoped carbon nanosheets as superior bifunctional electrocatalysts for oxygen reduction and evolution. *Nano Energy* **2016,** *19*, 373-381.

188. Liu, Q.; Zhang, J., A general and controllable synthesis of ComSn (Co9S8, Co3S4, and Co1-xS) hierarchical microspheres with homogeneous phases. *CrystEngComm* **2013,** *15* (25), 5087-5092.

189. Mahmood, N.; Zhang, C. Z.; Jiang, J.; Liu, F.; Hou, Y. L., Multifunctional Co3S4/Graphene Composites for Lithium Ion Batteries and Oxygen Reduction Reaction. *Chemistry-a European Journal* **2013,** *19* (16), 5183-5190.

190. Jin, R.; Yang, L.; Li, G.; Chen, G., Hierarchical worm-like CoS2 composed of ultrathin nanosheets as an anode material for lithium-ion batteries. *Journal of Materials Chemistry A* **2015,** *3* (20), 10677-10680.

191. Cao, F.; Zhao, M.; Yu, Y.; Chen, B.; Huang, Y.; Yang, J.; Cao, X.; Lu, Q.; Zhang, X.; Zhang, Z.; Tan, C.; Zhang, H., Synthesis of Two-Dimensional CoS1.097/Nitrogen-Doped Carbon Nanocomposites Using Metal–Organic Framework Nanosheets as Precursors for Supercapacitor Application. *J. Am. Chem. Soc.* **2016,** *138* (22), 6924-6927.

192. Dou, S.; Tao, L.; Huo, J.; Wang, S. Y.; Dai, L. M., Etched and doped Co9S8/graphene hybrid for oxygen electrocatalysis. *Energy Environ. Sci.* **2016,** *9* (4), 1320-1326.

193. Ma, X.; Zhang, W.; Yida, D.; Zhong, C.; Hu, W.; Han, X., *Phase and composition controlled synthesis of cobalt sulfide hollow nanospheres for electrocatalytic water splitting*. **2018**; Vol. 10.

194. Ganesan, P.; Prabu, M.; Sanetuntikul, J.; Shanmugam, S., Cobalt Sulfide Nanoparticles Grown on Nitrogen and Sulfur Codoped Graphene Oxide: An Efficient Electrocatalyst for Oxygen Reduction and Evolution Reactions. *ACS Catalysis* **2015,** *5* (6), 3625-3637.

195. Qian, H.; Tang, J.; Wang, Z.; Kim, J.; Kim, J. H.; Alshehri, S. M.; Yanmaz, E.; Wang, X.; Yamauchi, Y., Synthesis of Cobalt Sulfide/Sulfur Doped Carbon Nanocomposites with Efficient Catalytic Activity in the Oxygen Evolution Reaction. *Chemistry – A European Journal* **2016,** *22* (50), 18259-18264.

196. Li, W. Q.; Li, Y. H.; Wang, H. J.; Cao, Y. H.; Yu, H.; Peng, F., Co9S8-porous carbon spheres as bifunctional electrocatalysts with high activity and stability for oxygen reduction and evolution reactions. *Electrochim. Acta* **2018,** *265*, 32-40.

197. Tong, H.; Bai, W.; Yue, S.; Gao, Z.; Lu, L.; Shen, L.; Dong, S.; Zhu, J.; He, J.; Zhang, X., Zinc cobalt sulfide nanosheets grown on nitrogen-doped graphene/carbon nanotube film as a high-performance electrode for supercapacitors. *Journal of Materials Chemistry A* **2016,** *4* (29), 11256-11263.

198. Kulkarni, P.; Nataraj, S. K.; Balakrishna, R. G.; Nagaraju, D. H.; Reddy, M. V., Nanostructured binary and ternary metal sulfides: synthesis methods and their application in energy conversion and storage devices. *Journal of Materials Chemistry A* **2017,** *5* (42), 22040-22094.

199. Liu, Y.; Li, Y.; Kang, H.; Jin, T.; Jiao, L., Design, synthesis, and energy-related applications of metal sulfides. *Materials Horizons* **2016,** *3* (5), 402-421.

200. Zhang, Y. T.; Chao, S. J.; Wang, X. B.; Han, H. J.; Bai, Z. Y.; Yang, L., Hierarchical Co9S8 hollow microspheres as multifunctional electrocatalysts for oxygen reduction, oxygen evolution and hydrogen evolution reactions. *Electrochim. Acta* **2017,** *246*, 380-390.

201. Chauke, H. R.; Nguyen-Manh, D.; Ngoepe, P. E.; Pettifor, D. G.; Fries, S. G., Electronic structure and stability of the pentlandites Co9S8 and (Fe, Ni)9S8. *Physical Review B* **2002,** *66* (15), 155105.

202. Yin, Y.; Erdonmez, C. K.; Cabot, A.; Hughes, S.; Alivisatos, A. P., Colloidal Synthesis of Hollow Cobalt Sulfide Nanocrystals. *Adv. Funct. Mater.* **2006,** *16* (11), 1389-1399.

203. Dong, W.; Wang, X.; Li, B.; Wang, L.; Chen, B.; Li, C.; Li, X.; Zhang, T.; Shi, Z., Hydrothermal synthesis and structure evolution of hierarchical cobalt sulfide nanostructures. *Dalton Transactions* **2011,** *40* (1), 243-248.

204. Al-Mamun, M.; Wang, Y.; Liu, P.; Zhong, Y. L.; Yin, H.; Su, X.; Zhang, H.; Yang, H.; Wang, D.; Tang, Z.; Zhao, H., One-step solid phase synthesis of a highly efficient and robust cobalt pentlandite electrocatalyst for the oxygen evolution reaction. *Journal of Materials Chemistry A* **2016,** *4* (47), 18314-18321.

205. Li, R.; Dai, Y.; Chen, B.; Zou, J.; Jiang, B.; Fu, H., Nitrogen-doped Co/Co9S8/partly-graphitized carbon as durable catalysts for oxygen reduction in microbial fuel cells. *J. Power Sources* **2016,** *307*, 1-10.

206. Geng, P. B.; Zheng, S. S.; Tang, H.; Zhu, R. M.; Zhang, L.; Cao, S.; Xue, H. G.; Pang, H., Transition Metal Sulfides Based on Graphene for Electrochemical Energy Storage. *Advanced Energy Materials* **2018,** *8* (15).

207. Lin, X.; Yuan, R.; Cai, S.; Jiang, Y.; Lei, J.; Liu, S.-G.; Wu, Q.-H.; Liao, H.-G.; Zheng, M.; Dong, Q., An Open-Structured Matrix as Oxygen Cathode with High Catalytic Activity

and Large Li2O2 Accommodations for Lithium–Oxygen Batteries. *Advanced Energy Materials* **2018,** *8* (18), 1800089.

208. Sennu, P.; Christy, M.; Aravindan, V.; Lee, Y.-G.; Nahm, K. S.; Lee, Y.-S., Two-Dimensional Mesoporous Cobalt Sulfide Nanosheets as a Superior Anode for a Li-Ion Battery and a Bifunctional Electrocatalyst for the Li–O2 System. *Chem. Mater.* **2015,** *27* (16), 5726-5735.

209. Lyu, Z.; Zhang, J.; Wang, L.; Yuan, K.; Luan, Y.; Xiao, P.; Chen, W., CoS2 nanoparticles–graphene hybrid as a cathode catalyst for aprotic Li–O2 batteries. *RSC Advances* **2016,** *6* (38), 31739-31743.

Chapter 3 Polydopamine Derived N-doped Graphene Electrodes with Controlled Pores for High-Capacity Rechargeable Li-O_2 Batteries

3.1 Introduction and Significance

The catalytic activity of catalysts in Li-O2 batteries are strongly associated with the surface structure and heteroatom doping of oxygen electrode. However, there is a lack of understanding of how porous structures can influence the catalytic activity of N-doped graphene cathode regarding to oxygen reduction reaction (ORR) and oxygen evolution reaction (OER) for Li-O2 batteries. This work introduced a robust method using polydopamine as N precursor, polystyrene spheres as template to prepare porous N doped graphene as cathode materials for Li-O2 batteries and systematically explore the relationship between porous structures and the catalytic performance of N-doped graphene. The highlights of this work include:

(a) We introduced control-sized porous structure on polydopamine derived N-doped graphene as oxygen electrode for Li-O2 batteries to explore the relationship between porous structure and the performance of Li-O2 batteries.

(b) We demonstrated the porous structures on N-rGO can improve ORR activity by providing sufficient space for discharge products and expose more N active site. The N-rGO with 170 nm pores achieved one of the highest discharge specific capacity at a current rate of 200 mA g^{-1}.

(c) We further elucidated porous structures improved OER activity for N-rGO by the improvement of cycle life and stability of porous N-rGO Li-O_2 batteries.

(d) We studied the morphologies of cathode materials before and after discharge and charge to discover the distortion of N-doped caused by irregular Li2O2 crystalline residue is the main reason for battery decays.

3.2 Polydopamine Derived N-doped Graphene Electrodes with Controlled Pores for High-Capacity Rechargeable Li-O_2 Batteries

This section is included as an un-submitted manuscript by Qi Bi, Guoxue Liu, Heng Wang, Yanting Yin, Gunther Andersson, Haihui Wang and Sheng Dai.

Statement of Authorship

Title of Paper	Polydopamine Derived N-doped Graphene Electrodes with Controlled Pores for High-Capacity Rechargeable Li-O2 Batteries
Publication Status	☐ Published ☐ Accepted for Publication ☐ Submitted for Publication ☑ Unpublished and Unsubmitted work written in manuscript style
Publication Details	To be submitted.

Principal Author

Name of Principal Author (Candidate)	Qi Bi		
Contribution to the Paper	Designed research plan; performed experiments, parts of material characterizations, and battery performance evaluations; analysed data; wrote and edited manuscript.		
Overall percentage (%)	80%		
Certification:	This paper reports on original research I conducted during the period of my Higher Degree by Research candidature and is not subject to any obligations or contractual agreements with a third party that would constrain its inclusion in this thesis. I am the primary author of this paper.		
Signature		Date	15/10/2019

Co-Author Contributions

By signing the Statement of Authorship, each author certifies that:

i. the candidate's stated contribution to the publication is accurate (as detailed above);

ii. permission is granted for the candidate in include the publication in the thesis; and

iii. the sum of all co-author contributions is equal to 100% less the candidate's stated contribution.

Name of Co-Author	Guoxue Liu		
Contribution to the Paper	Coached the fabrication of Li-O2 battery.		
Signature		Date	

Name of Co-Author	Heng Wang		
Contribution to the Paper	Discussed the research plan.		
Signature		Date	15/10/2019

Name of Co-Author	Yanting Yin		
Contribution to the Paper	Performed XPS tests.		
Signature		Date	

Name of Co-Author	Gunther Andersson		
Contribution to the Paper	Facilitated XPS tests.		
Signature		Date	

Name of Co-Author	Haihui Wang		
Contribution to the Paper	Co-supervised the research.		
Signature		Date	18/10/2019

Name of Co-Author	Sheng Dai		
Contribution to the Paper	Supervised the research and revised the manuscript.		
Signature		Date	15/10/2019

Please cut and paste additional co-author panels here as required.

Polydopamine Derived N-doped Graphene Electrodes with Controlled Pores for High-Capacity Rechargeable Li-O_2 Batteries

Qi Bi, Guoxue Liu, Heng Wang, Yanting Yin, Gunther Andersson, Haihui Wang, and Sheng Dai**

Q. Bi, H. Wang, Prof. H. Wang, Prof. S. Dai
School of Chemical Engineering
The University of Adelaide
Adelaide SA 5005 Australia

G. Liu, Prof. H. Wang
School of Chemistry & Chemical Engineering
South China University of Technology
Guangzhou 510640 China

Y. Yin, Prof. Gunther Andersson
School of Chemical and Physical Sciences
Flinders University
Adelaide SA 5001 Australia

Prof. S. Dai
Department of Chemical Engineering
Brunel University London
Uxbridge UB8 3PH United Kingdom

* Corresponding authors

Email: hhwang@scut.edu.cn

s.dai@adelaide.edu.au

Abstract

Electrochemical performance of Li-O_2 batteries strongly depend on the catalytic activities of cathode materials towards oxygen reduction reaction (ORR) and oxygen evolution reaction (OER) that associate with both surface structure and heteroatom doping of oxygen electrode. In this study, we introduced a robust method of using polydopamine as N precursor and polystyrene beads as template to produce porous N doped graphene as the cathode materials for Li-O_2 batteries. Both porous structure and N-doped graphene facilitate bi-functional (ORR/OER) electrocatalytic performance and superior properties in promoting higher capacity and longer cycle life of Li-O_2 systems. As a result, Li-O_2 batteries with N-rGO/170 cathode materials display excellent electrochemical performance with a discharge capacity of 16777 mA h g^{-1} and excellent reversible recharge characteristics, outperforming most of the current reported N-doped graphene cathode.

Keywords: porous structure, polydopamine, nitrogen doped graphene, lithium oxygen batteries, ORR/OER

Introduction

Non-aqueous rechargeable Li-O_2 batteries have been investigated intensely in recent years for their extraordinary theoretical energy densities. They are viewed as the promising candidates for next generation energy storage systems [1-10]. However, the development of Li-O_2 battery is still hindered by several challenges, including low rate capability, inferior cycling stability and poor round-trip efficiency. In order to tackle these problems, the mechanism of Li-O_2 battery has been carefully studied: during discharge, Li_2O_2 is formed through the oxygen reduction reaction (ORR) process and deposited on cathode surface; during charge, Li_2O_2 decomposes into lithium ion and oxygen through the oxygen evolution reaction (OER) [1, 8, 10]. It is found that the generation of un-favorite by-products and the accumulation of insoluble discharge products are the major reasons to cause serious decay of electrochemical performance by hindering the reversible redox reactions (ORR/OER) [11]. Therefore, the development of electrochemical catalysts that facilitate both ORR/OER processes with limited by-product formation is crucial to improve the performance of Li-O_2 batteries.

Due to its excellent properties in electrochemistry, graphene based materials are widely used as cathode materials for Li-O_2 batteries. To tailor material properties and improve catalytic performance, graphene are doped with various heteroatoms such as N, S and B [12-16]. Among them, nitrogen doped graphene is particularly attractive because of the excellent catalytic activity to improve ORR performance of Li-O_2 battery [17-18]. However, traditional nitrogen doped methods such as melamine, NH_3, polypyrrole, polyaniline [19-20] are limited by their weak nanostructural tunability and poor residual yield for further applications [21]. Our team recently introduced polydopamine (PDA) as a high efficiency N source to dope graphene oxide. The as-prepared N doped reduced graphene oxide shows excellent catalytic activity towards ORR and exhibits potential for various post-modifications [22-23].

On the other hand, the electrochemical performance of cathode materials is also largely influenced by the surface structures of oxygen electrode associated with O_2 diffusion and discharge product storage [24]. It has been noticed that porous structure on cathode materials can

significantly promote the performance of Li-O_2 batteries in specific capacity and cycle abilities performance. [25-30]. Wang and co-workers prepared porous GO cathode materials with silica template to achieve long life and high capacity Li-O_2 batteries [31]. The outstanding results can be attributed to the introduction of porous structure on graphene which largely enlarges surface areas for discharge product storage and increases the exposure of active sites on cathode materials.

Despite great promises, the effect of porous structure on N-doped graphene has not been studied as cathode materials in Li-O_2 batteries. Herein, we employed PDA derived N-rGO with templated porous structure as the cathode materials for Li-O_2 batteries to elucidate the relation between porous structure and catalytic performance. We found that the PDA derived N-rGO with 170 nm porous structure shows great electrochemical catalytic performance towards ORR/OER and delivered high specific discharge capacity and long cycle life to Li-O_2 batteries due to its structure advantages.

Experimental Section

Materials: Graphite flake (100 mesh), potassium permanganate ($KMnO_4$), phosphoric acid (H_3PO_4 85%), sodium dodecyl sulphate (SDS), styrene, polydopamine (PDA), and N-methyl-2-pyrrolidone (NMP) were purchased from Sigma-Aldrich. Potassium peroxydisulfate (KPS) was obtained from Fluka. Sulfuric acid (H_2SO_4, 98%), hydrogen peroxide (H_2O_2, 30%), and polyvinylidene fluoride (PVDF) were supplied by Chem-Supply. Glass fiber membrane (Grade GF/F) were from Whatman. Lithium foil was supplied by China Energy Lithium Co., Ltd. 1M lithium bis(trifluoromethanesulfonyl)imide (LiTFSI) intetraethylene glycol dimethyl ether (TEGDME) was from Suzhou Qianmin Chemical Reagent Co., Ltd. Ultra-high purity (99.999%) O_2 was acquired from Coregas.

Synthesis of porous N-rGO: GO was synthesized from natural graphite flakes by an improved Hummer's method (supporting information). 85 ml of GO dispersion (2 mg ml^{-1}) was mixed

with 125 mg polydopamine dissolved in 10 ml Milli-Q water. The mixture was added ti 130 ml Milli-Q water and sonicated for 5 min. Later, 25 ml PBS buffer (0.4 M, pH = 8.5) was added, and continuously stirred at room temperature for 24 h. After that, 13 ml polystyrene template dispersion (25 mg ml^{-1}) with different particle sizes (170 nm, 230 nm, and 410 nm) was add to the mixture and stirred at room temperature for another 12 h. 1.5 g vitamin C was added into the mixture and stirred till the mixture turned to black. Porous N-rGO was collected by centrifugation and washed for three times with Milli-Q water. On the other hand, the non-porous N-rGO was also prepared according to the same procedure but without the addition of PS templates. The final products were obtained through carbonization in a temperature programmable tube furnace under N_2 atmosphere at 400 °C for 2 h with a heating rate of 1 °C min^{-1}, which was followed by further treatment at 900 °C for 3 h with a heating rate of 5 °C min^{-1}.

Microstructural and chemical characterization: Field emission scanning electron microscope (FESEM) images were obtained on a FEI Quanta 450 SEM, the transmission electron microscopy images were acquired on a Tecnai G2 Spirit TEM. Raman spectra were collected on an iHR550 from HORIBA Scientific with a 532 nm solid-state laser as excitation source. The X-ray photoelectron spectroscopy (XPS) was conducted on an UHV no-monochromatic X-ray source (12 KV-200 W) built by SPECS. Nitrogen adsorption-desorption isotherm was measured on the Tristar II (Micrometrics) at 77 K. Pore size distribution was calculated by the Barrett-Joyner-Halenda (BJH) model, and the specific surface area of the materials was calculated using adsorption data at the pressure range of P/P_0 = 0.05 - 0.3 by the Brunauer-Emmett-Teller (BET) model on a Belsorp-Max instrument.

Li-O_2 battery evaluation: The oxygen electrodes were fabricated by coating the homogeneous slurry contained N-rGO and polyvinylidene fluoride (PVDF) (weight ratio 9:1) in N-methyl-2-pyrrolidone (NMP) onto Ni foam and dried at 80 °C overnight. The typical loading of the oxygen electrode is about 0.5 $mg_{(carbon)}$ cm^{-2}. The Li-O_2 batteries were assembled with 2032-type coin cells in an argon filled glove box with a water and oxygen level less than 0.5 ppm.

The Li-O_2 cells are established using a Li metal foil as the counter electrode and the anode, a glass fiber membrane separator, the as-prepared oxygen cathode, and 1 M LiTFSI in tetra (ethylene) glycol dimethyl ether (TEGDME) electrolyte. All measurements were conducted at 1 atm dry oxygen atmosphere. Galvanostatic discharge/recharge was tested on a Neware battery testing system within a voltage window of 2.0 – 4.5 V (Li/Li^+) after resting for 10 h at room temperature. Cyclic voltammetry (CV) tests were measured at a rate of 0.1 mV s^{-1} within the potential range of 2.0 to 4.5 V (Li/Li^+) by a CHI600 electrochemical workstation. Electrochemical impedance spectroscopy (EIS) were performed by a Zahner IM6 Electrochemical workstation in the frequency range of 0.1 Hz to 100 kHz.

Results and Discussion

Nitrogen doped reduced graphene oxide (N-rGO) with well-defined porous structure were prepared by a combination process of dopamine adsorption, PS template loading, GO reduction and materials calcination as shown in Scheme 1. Dopamine was adsorbed onto GO nanosheets, following by anchoring polystyrene (PS) templates and Vitamin C reduction. The PS templates were finally removed by calcinating the as-prepared materials at 900 °C under nitrogen atmosphere to obtain the N-rGO with well-controlled pores.

To elucidate the influence of pores to electrochemical properties of N-rGO, three PS templates of 170, 230 and 410 nm in diameter were used to prepare a series of N-rGO with different controlled pores (N-rGO/170, N-rGO/230, and N-rGO/410). Two references of non-porous N-rGO and rGO were also prepared for comparison (supporting information). The morphologies and structures of resulting rGO, N-rGO, N-rGO/170, N-rGO/230 and N-rGO/410 were examined by scanning electron microscopy (SEM) and transmission electron microscopy (TEM). Compared with the nanosheet structures of rGO (Figure 3.S1a) and N-rGO (Figure 3.S1b), N-rGO/170, N-rGO/230 and N-rGO/-410 (Figure 3.1a-c) showed porous architectures, indicating the successful synthesis of N-rGO with controlled pores in the presence of PS

templates. TEM images (Figure 3.1d-f) provides further evidence of the fabricated porous N-rGO with controlled pore size of 170, 230 and 410 nm. These well-controlled pores are able to provide tunnels facilitating express transfer of Li^+ and O_2 and act as ideal storage sites for the discharge products of Li-O_2 batteries[32].

The nitrogen adsorption-desorption isotherms (Figure 3.2) and pore size distribution (Figure 3.S2) were compared among rGO, N-rGO and various templated porous N-rGO. The adsorption isotherms for all materials exhibited type IV characteristics that indicates the presence of both micro and mesoporous structures [26, 33]. The steep rise at low relative pressure ($P/P_0 < 0.001$) reflects the presence of large amount of microporous structure. [34] The steep rises at high relative pressure ($P/P_0 = 1$) is caused by the wrinkles on rGO, N-rGO surfaces and the template-introduced porous structure on N-rGO/170, N-rGO/230 and N-rGO/410. In addition, H3 hysteresis loop presents at the P/P_0 between 0.4 and 1.0 in all materials, suggesting the existing of slit-shaped pores between plate-like graphene nanosheets [35]. The pore size distribution (Figure 3.S2) confirms the existence of 2 nm micropores for all materials. Brunauer-Emmett-Teller (BET) method was used to calculate the specific surface areas and pore volumes for rGO (110 $m^2 g^{-1}$, 0.30 $cm^3 g^{-1}$), N-rGO (111 $m^2 g^{-1}$, 0.36 $cm^3 g^{-1}$), N-rGO/170 (449 $m^2 g^{-1}$, 1.00 $cm^3 g^{-1}$), N-rGO/230 (373 $m^2 g^{-1}$, 0.91 $cm^3 g^{-1}$) and N-rGO/410 (136 $m^2 g^{-1}$, 0.23 $cm^3 g^{-1}$). The introduction of porous structure significantly improves the surface areas and pore volumes of N doped graphene, which are highly required for cathode materials in Li-O_2 batteries for large space to store discharge products and further to facilitate ORR/OER reactions in discharge/recharge process.

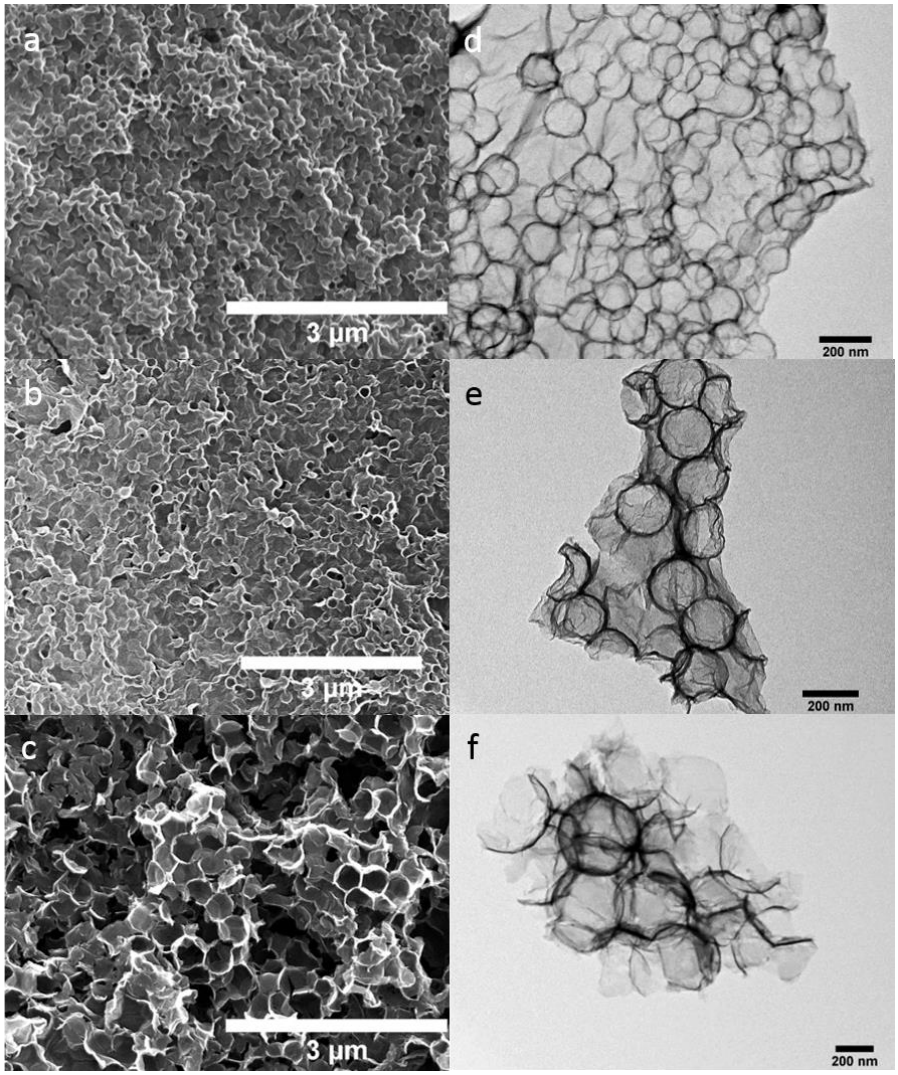

Figure 3.1. Morphologies of porous N-rGO in the presence of different polysterene templates. (a-c) SEM images for N-rGO/170, N-rGO/230, and N-rGO/410; (d-f) TEM images for N-rGO/170, N-rGO/230, and N-rGO/410.

The Raman spectra of rGO, N-rGO and porous N-rGO displays typical D band and G band at approximate Raman shifts at1350 and 1580 cm^{-1} [36]. The intensity ratio of D band and G band (I_D/I_G) can be used to quantify the defects and disordered structures of graphene-based materials [37]. As shown in Figure 3.2b, I_D/I_G increased from 1.07 (rGO) to 1.17 (N-rGO), which demonstrates more defects and disordered structure being produced as a result of incorporation of N and partial damage of the graphitic structure [37-38]. Compared with N-rGO, the I_D/I_G of N-rGO/170 (1.18), N-rGO/230 (1.17) and N-rGP/410 (1.16) are approximately identical, which suggests that the porous structure generation from PS templates does not alter the defects or disordered structures of N-rGO.

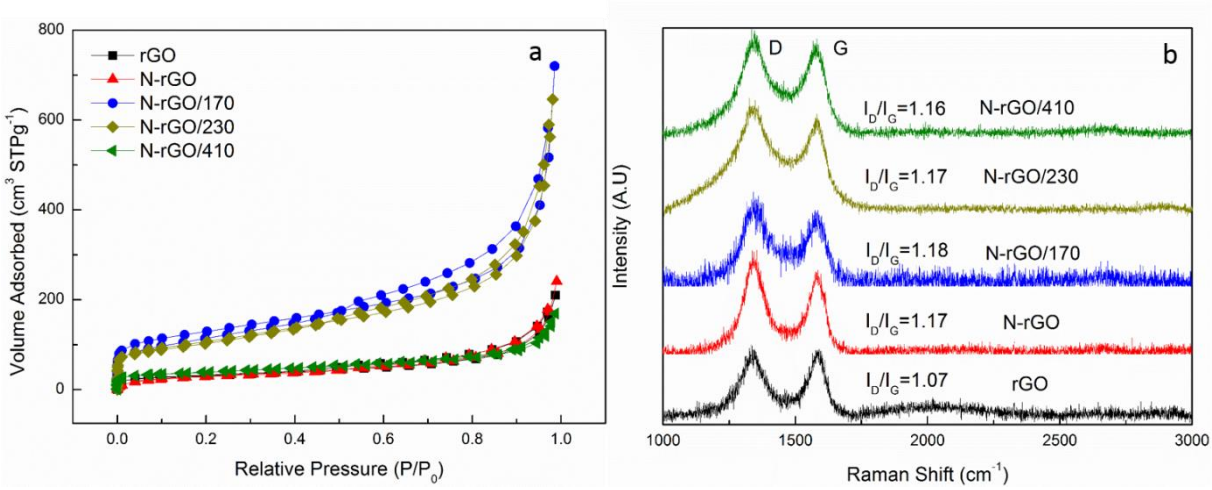

Figure 3.2. (a) N_2 adsorption-desorption isotherms and (b) Raman spectra of various cathode materials.

To further quantify the surface compositions and nitrogen bonding configurations of rGO, N-rGO and N-rGO/170, X-ray photoelectron spectroscopy (XPS) results are shown in Figures 3-3 and 3-S3. The absence of N 1s in the XPS survey scan for rGO, and the existence of N 1s in the XPS survey scans for N-rGO and N-rGO/170 confirm the successful doping N using PDA. To be specific, nitrogen doping is further proved by the appearance of sp^3 C-N (c.a 287.1 eV) and sp^2 C=N (c.a 285.8 eV) bonds on the high resolution C 1s spectra of N-rGO and N-rGO/170 by comparing with that of rGO [39]. In addition, reduce of C-O (c.a 286.0 eV) bond and COO (c.a 289.0 eV) group are observed on N-rGO and N-rGO/170, due to further reduction of rGO by introduced N on GO [40]. According to peak areas, N-rGO contains 2.9 at% N, while N-rGO/170 contains 2.3 at% N. The decrease of nitrogen content in N-rGO/170 is attributed to the contribution of extra carbon from polystyrene templates during calcination. The high resolution N 1s XPS spectra of N-rGO and N-rGO/170 reveal that nitrogen atoms in the as-made materials exist in the forms of graphitic (c.a. 401.2 eV), pyridinic (c.a. 398.4 eV), and oxidic (c.a. 403.2 eV) nitrogen types [41]. This demonstrates that pyrrolic N has been completely converted to pyridinic N and graphitic N after calcination [22]. Pyridinic and graphitic N are viewed as active N that can facilitate the process of catalytical performance in electrochemical

reactions. Pyridinic N increases the electron-donating ability, and graphitic N has been proven to promote ORR process by improving oxygen adsorption [42]. The amount of these active N in both N-rGO and N-rGO/170 are 1.94 at%. Although the total amount of N dropped after introducing porous structures decreases, the amount of active N in N-rGO and N-rGO/170 keep at around the same level. Comparing with non-porous N-rGO, the introduction of controlled pores to N-rGO only affected morphology, surface areas and pore volumes. The defects and disorder structures as well as active N doping levels remain approximately the same.

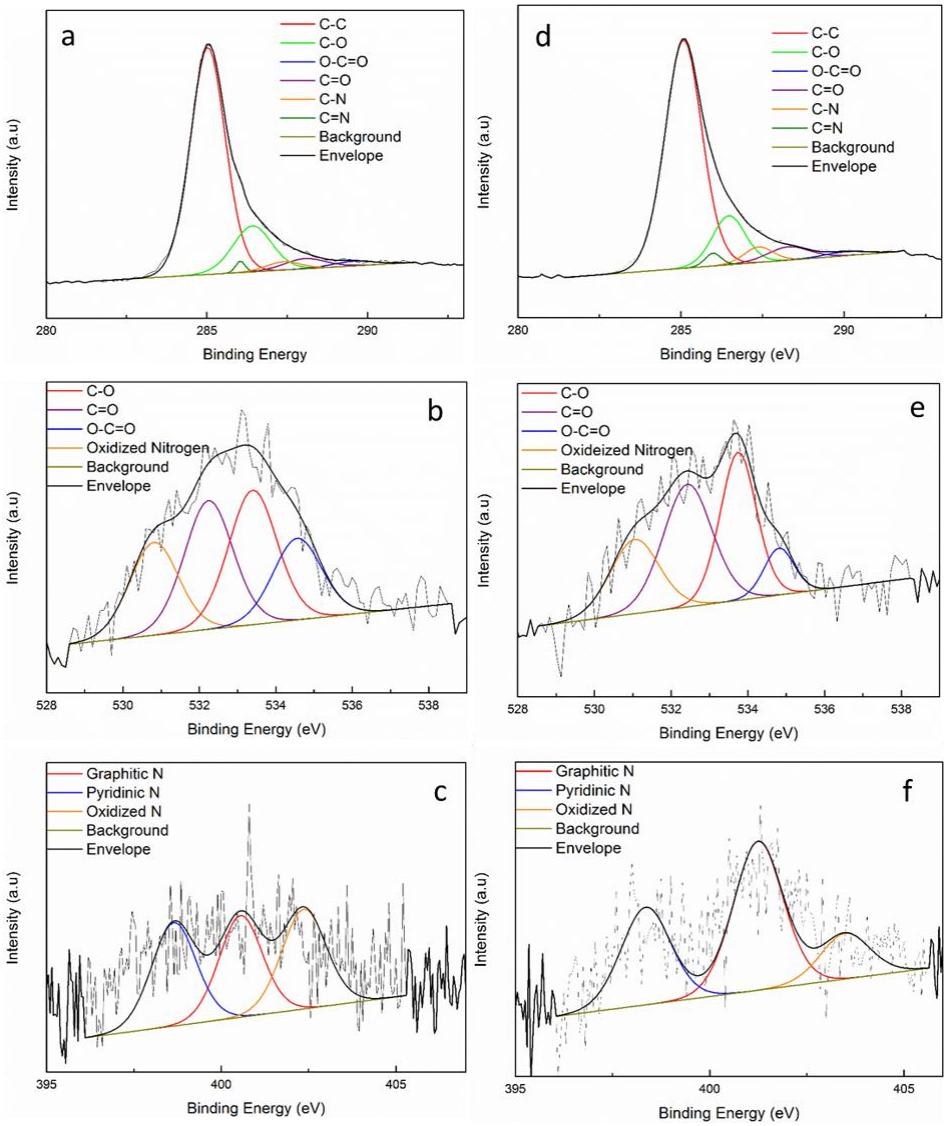

Figure 3.3. XPS spectra of N-rGO and N-rGO/170. (a) C 1s spectrum of N-rGO; (b) O1s spectrum of N-rGO; (c) N 1s spectrum of N-rGO; (d) C 1s spectrum of N-rGO/170; (e) O1s spectrum of N-rGO/170; (f) N 1s spectrum of N-rGO/170.

The electrochemical performance of rGO, N-rGO, and porous N-rGO as the cathode materials in Li-O_2 batteries was tested in coin cells with fresh Li foil as anode and 1 M LiTFSI in tetraethylene glycol dimethyl ether (TEGDME) as electrolyte. During discharge, Li_2O_2 forms through the ORR process and deposited onto the cathode; during charge, Li_2O_2 decomposes into lithium ion and oxygen through the OER [43]. The galvanostatic first discharge-charge tests (Figure 3.4a) were measured within the voltage window of 2.0 - 4.5 V. The discharge-charge curves of Li-O_2 batteries were tested with a current density of 200 mA g^{-1}. The Li-O_2 battery with rGO as cathode materials shows the lowest specific discharge capacity at 1627 mA h g^{-1}. A higher specific discharge capacity at 2841 mA h g^{-1} is achieved for N-rGO. The introduction of controlled porous structure on N-rGO largely increases discharge capacity with 6505 mA h g^{-1} for N-rGO/410, 10908 mA hg^{-1} for N-rGO/230, and as high as 16777 mA h g^{-1} for N-rGO/170. Remarkably, the discharge capacity of 16777 mA h g^{-1} is one of the highest being achieved from pure carbon-based Li-O_2 batteries (Table 3.S1). On the other hand, the first recharge capability for N-rGO/170 is 15868 mA h g^{-1}, taking 94.6 % of initial discharge capacity, which is similar with the 95.4 % recovery of N-rGO/230 cathode. Other cathode materials achieve fully recovery for charge capacity. The results suggests the introducing controlled pores to N-rGO facilitates discharge capability significantly due to the increase of surface areas and pore volumes, where more active ORR sites can be exposed and more cathode surface space for discharge product deposition can be achieved. However, the charge performance is not benefit from the porous structure. The electrochemical impedance spectroscopy (EIS) is an effective method to investigate the electrochemical behavior of batteries. The EIS for initial batteries with rGO, N-rGO and N-rGO/170 as electrodes shows in Figure 3.S4. The resistance of battery with N-rGO electrode is slightly less than that of rGO, while the resistance of battery with N-rGO/170 electrode is much less than that of rGO and N-rGO. That gives another possible explanation for the large discharge and recharge capacity of N-rGO/170 electrode, where the N-rGO/170 with controlled pores seems to be highly conductive and structure stable, which improves ionic mobility and is beneficial to ion transfer,

consequently led to a higher discharge capacity [44-45].

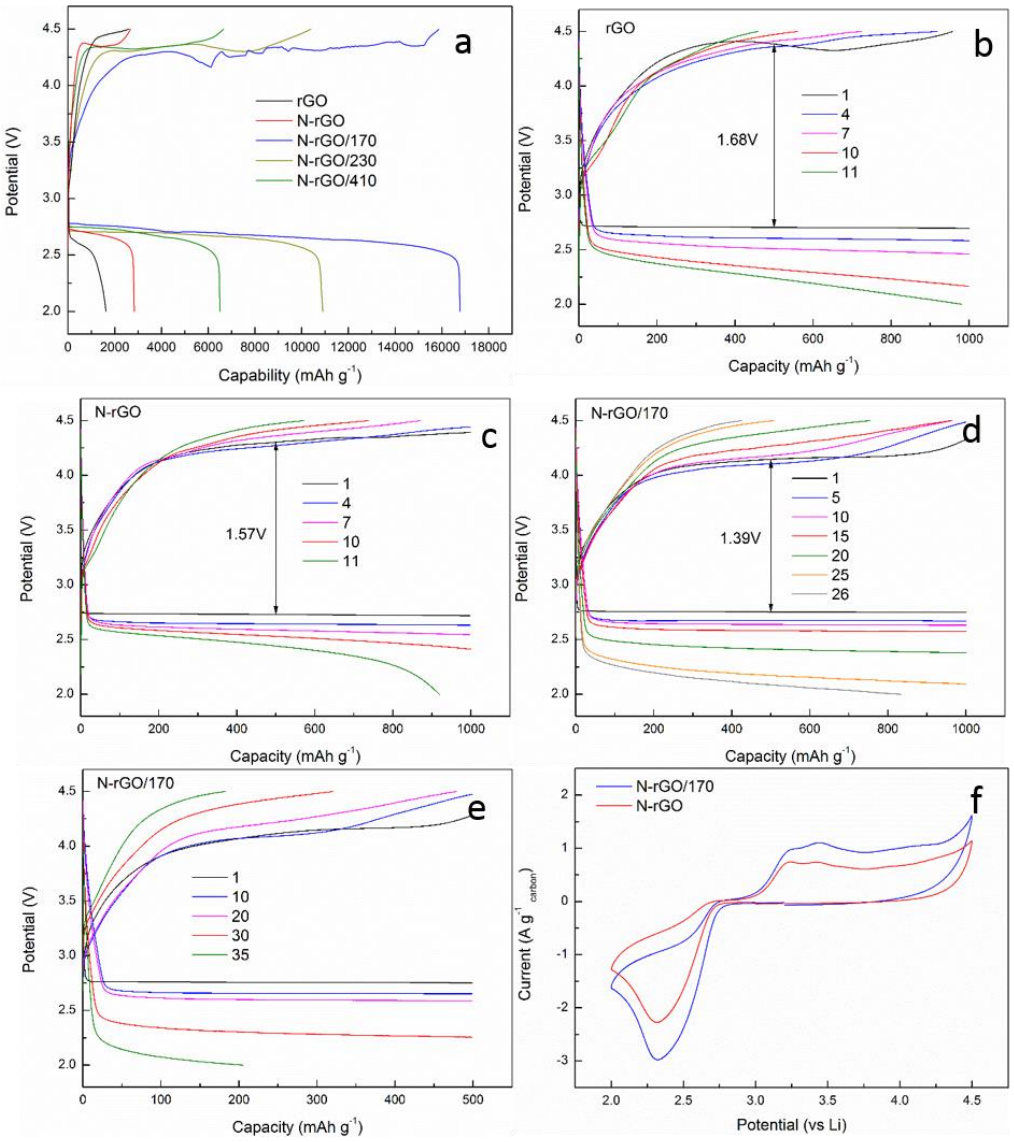

Figure 3.4. (a) Discharge-charge curves of Li-O_2 batteries with various catalysts at a current density of 200 mA g^{-1}; Cycling performances of Li-O_2 batteries with (b) rGO at a controlled capacity of 1000 mA h g^{-1}; (c) N-rGO at a controlled capacity of 1000 mA h g^{-1}; (d) N-rGO/170 at a controlled capacity of 1000 mA h g^{-1}. (e) N-rGO/170 at a controlled capacity of 500 mA h g^{-1}. (f) CV curves of N-rGO and N-rGO/170 at a constant scan rate of 1 mV s^{-1}.

To further investigate the stability and cycle ability, cycling performance of Li-O_2 batteries with different cathode materials were tested with a current density at 200 mA h g^{-1} as shown in Figures 3-4b-e and 3-S5a-b. Batteries with both rGO (Figure 3.4b) and N-rGO (Figure 3.4c) as cathodes can stay stable to the 10th cycle with a cut-off capacity of 1000 mA h g^{-1}. After the introduction of controlled pores, the cycle stability of battery increases to 14th for N-rGO/410

(Figure 3.S5a) and 21st for N-rGO/230 (Figure 3.S5b). Battery with N-rGO/170 electrode can stay stable till the 25th cycle with a cut-off capacity of 1000 mA h g^{-1} (Figure 3.4d) and 34th cycle with a cut-off capacity of 500 mA h g^{-1} (Figure 3.4e). Obviously, porous N-rGO electrodes exhibit much better stability and cycle ability than non-porous electrodes, indicating porous structure with high surface areas and pore volumes provide enough space to promote the formation (ORR) and decomposition (OER) of Li_2O_2 during discharge and recharge to maintain cycling stability for Li-O_2 batteries [31]. In addition, the average first discharge voltage platform of N-rGO/170 is 2.75 V (vs Li^+/Li) at 200 mA g^{-1} with a cut-off capacity of 1000 mA h g^{-1}, higher than that of rGO (2.70 V) and N-rGO (2.72 V). Accordingly, the first charge voltage plateau of Li-O_2 battery with N-rGO/170 electrode is about 4.14 V, lower than that of rGO (4.38 V) and N-rGO (4.29 V). Therefore, the Li-O_2 battery with N-rGO/170 exhibits a lower over potential (1.39 V) than rGO (1.68 V) and N-rGO (1.57 V). These results reveal that the presence of controlled pores in N doped rGO effectively promotes both ORR and OER processes and reduces the overpotential for Li-O_2 batteries. That can be further confirmed by the cyclic voltammetry (CV) study. Figure 3.4f shows the CV curves of N-rGO and N-rGO/170 electrodes within 2.0 – 4.5 V scanned at 1 mV s^{-1}. The N-rGO/170 electrode presents much higher onset ORR/OER potential, and larger ORR/OER peaks, which advises lower ORR/OER kinetic overpotential and better ORR/OER performance [46]. It is worth noting that the CV curve shows two obvious oxidation peaks at around 3.2 and 3.4 V during OER process. The first peak is attributed to the surface oxidation of LiO_2, and the second peak is due to the oxidation of bulk Li_2O_2 [47-49]. The N-rGO/170 electrode displays a much higher Li_2O_2 oxidation peak than that of N-rGO, which explains the better cyclic stability of N-rGO/170 cathode due to the more effective decomposition of Li_2O_2 in OER process. The rate performance of the N-rGO/170 was tested at higher charge/discharge current densities of 400, 600, 800, and 1000 mA g^{-1} (Figure 3.S5c). The capacity decreases as increasing current densities. Meanwhile, at a higher current density, the Li-O_2 system deliveries a higher over potential. These results reveal that the electrocatalytic performance of N-rGO/170 cathodes towards both ORR and OER are much

more stable at lower energy density.

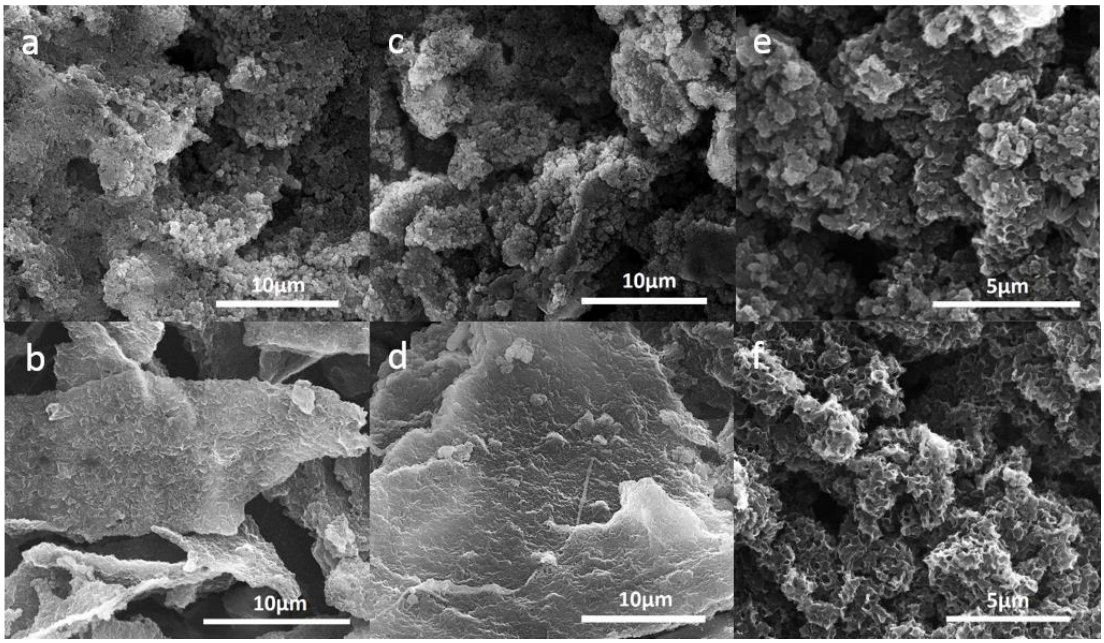

Figure 3.5. SEM images of cathode materials (a, b) N-rGO/170 after 1st full discharge, and recharge; (c, d) N-rGO/230 after 1st full discharge, and recharge; (e, f) N-rGO/410 after 1st full discharge, and recharge.

The morphologies of porous N-rGO cathodes after discharge and recharge are further investigated using SEM to explore the formation and decomposition of discharge products during the operation of Li-O_2 battery. Figures 3-5a, 3-5c and 3-5e presents the morphology of N-rGO/170, N-rGO/230, N-rGO/410 electrodes after first full discharge. From the SEM images, more discharge products are generated on N-rGO/170 electrode, and Li_2O_2 on N-rGO/170 electrode are smaller and denser than N-rGO/230 and N-rGO/410 electrodes. The results support its largest first cycle full discharge capacity. After the first charge, parts of discharge products can still be seen on N-rGO/170 (Figure 3.5b), N-rGO/230 (Figure 3.5d), while N-rGO/410 (Figure 3.5f) recovers to its pristine state. The discharge residue on the surface of electrode materials can result in reducing catalytic performance in the OER process, which is the main reason for N-rGO/170 and N-rGO/230 fails to achieve full charge recovery from their discharge capacity. This can also be proved on the cycling CV curves of N-rGO/170 electrode

(Figure 3.S6) that the peak at around 3.4 V drops significantly in the second cycle due to less oxidation of Li_2O_2, so that results in the recharge fading of Li-O_2 systems. Compared with the SEM image of electrode materials (Figure 3.1), obvious distortion can be observed after first charge. It may be caused by the formation of irregular Li_2O_2 that deforms the structure of porous electrodes surface during first discharge. In order to discover factors that affect the cycle stability of Li-O_2 batteries, the morphology of N-rGO/170 electrode after the 1st and 20th discharge and recharge at a cut-off capacity of 1000 mA h g^{-1} was studied. The discharge products of 1st discharge (Figure 3.S7a) are smaller than those of 20th discharge (Figure 3.S7c) on N-rGO/170 electrode. It is very interesting to observe that after 1st charge (Figure 3.S7b) at a cut-off capacity of 1000 $mAhg^{-1}$, the cathode materials recover its original morphology without distortion of the porous structure or remaining any discharge products. In contrast, the cathode materials exhibits serious distortion and large amount discharge products are left on the surface of N-rGO/170 electrode after 20th recharge (Figure 3.S7d). The SEM images strongly support that the extreme deformation and discharge residue on the surface of electrode materials contribute to the fading of cycle stability.

Conclusion

N doped reduced graphene oxides with controlled pores have been successfully prepared using polydopamine as the nitrogen precursor and PS as the template. The relationship between porous structured N-rGO and ORR/OER catalytic performance in Li-O_2 batteries was investigated. A high discharge specific capacity of 16777 mA h g^{-1} with a high energy efficiency of 94.6% was achieved from the N-rGO/170 due to its specially controlled-pore structures and large surface areas. Most importantly, the N-rGO/170 electrode also demonstrated superior cycle stability than other electrode materials with an up to 34 cycles at a cut-off capacity of 500 mA h g^{-1} and 25 cycles at 1000 mA h g^{-1}. The low cycling capability was attributed to the serious distortion of electrode materials and presence of large amount irreversible discharge products on electrode surface. Controlled pore structure in electrode materials plays an

important role in facilitating both ORR and OER processes in Li-O_2 systems, and size of pores has significant impact to catalytic performance of electrode materials. Our work highlights the design strategies in cathode structure to improve the electrocatalytic performance for Li-O_2 systems.

References

1. Black, R.; Adams, B.; Nazar, L. F., Non-Aqueous and Hybrid Li-O2 Batteries. *Advanced Energy Materials* **2012,** *2* (7), 801-815.
2. Capsoni, D.; Bini, M.; Ferrari, S.; Quartarone, E.; Mustarelli, P., Recent advances in the development of Li-air batteries. *J. Power Sources* **2012,** *220*, 253-263.
3. Li, F.; Zhang, T.; Zhou, H., Challenges of non-aqueous Li-O2 batteries: electrolytes, catalysts, and anodes. *Energy Environ. Sci.* **2013,** *6* (4), 1125-1141.
4. Lu, J.; Li, L.; Park, J. B.; Sun, Y. K.; Wu, F.; Amine, K., Aprotic and Aqueous Li-O-2 Batteries. *Chem. Rev.* **2014,** *114* (11), 5611-5640.
5. Luntz, A. C.; McCloskey, B. D., Nonaqueous Li-Air Batteries: A Status Report. *Chem. Rev.* **2014,** *114* (23), 11721-11750.
6. Grande, L.; Paillard, E.; Hassoun, J.; Park, J. B.; Lee, Y. J.; Sun, Y. K.; Passerini, S.; Scrosati, B., The Lithium/Air Battery: Still an Emerging System or a Practical Reality? *Adv. Mater.* **2015,** *27* (5), 784-800.
7. Aurbach, D.; McCloskey, B. D.; Nazar, L. F.; Bruce, P. G., Advances in understanding mechanisms underpinning lithium-air batteries. *Nature Energy* **2016,** *1*.
8. Feng, N. N.; He, P.; Zhou, H. S., Critical Challenges in Rechargeable Aprotic Li-O-2 Batteries. *Advanced Energy Materials* **2016,** *6* (9).
9. Eftekhari, A.; Ramanujam, B., In pursuit of catalytic cathodes for lithium-oxygen batteries. *Journal of Materials Chemistry A* **2017,** *5* (17), 7710-7731.
10. Lim, H. D.; Lee, B.; Bae, Y.; Park, H.; Ko, Y.; Kim, H.; Kim, J.; Kang, K., Reaction chemistry in rechargeable Li-O-2 batteries. *Chem. Soc. Rev.* **2017,** *46* (10), 2873-2888.
11. Xu, Y. F.; Chen, Y.; Xu, G. L.; Zhang, X. R.; Chen, Z. H.; Li, J. T.; Huang, L.; Amine, K.; Sun, S. G., RuO2 nanoparticles supported on MnO2 nanorods as high efficient bifunctional electrocatalyst of lithium-oxygen battery. *Nano Energy* **2016,** *28*, 63-70.
12. Borchardt, L.; Zhu, Q.-L.; Casco, M. E.; Berger, R.; Zhuang, X.; Kaskel, S.; Feng, X.; Xu, Q., Toward a molecular design of porous carbon materials. *Mater. Today* **2017,** *20* (10), 592-610.
13. Wu, G.; Mack, N. H.; Gao, W.; Ma, S.; Zhong, R.; Han, J.; Baldwin, J. K.; Zelenay, P.,

Nitrogen Doped Graphene-Rich Catalysts Derived from Heteroatom Polymers for Oxygen Reduction in Nonaqueous Lithium-O-2 Battery Cathodes. *Acs Nano* **2012,** *6* (11), 9764-9776.

14. Shu, C.; Li, B.; Zhang, B.; Su, D., Hierarchical Nitrogen-Doped Graphene/Carbon Nanotube Composite Cathode for Lithium–Oxygen Batteries. *ChemSusChem* **2015,** *8* (23), 3973-3976.

15. Wu, F.; Xing, Y.; Li, L.; Qian, J.; Qu, W.; Wen, J.; Miller, D.; Ye, Y.; Chen, R.; Amine, K.; Lu, J., Facile Synthesis of Boron-Doped rGO as Cathode Material for High Energy Li-O2 Batteries. *ACS Appl Mater Interfaces* **2016,** *8* (36), 23635-45.

16. Han, J.; Guo, X.; Ito, Y.; Liu, P.; Hojo, D.; Aida, T.; Hirata, A.; Fujita, T.; Adschiri, T.; Zhou, H.; Chen, M., Effect of Chemical Doping on Cathodic Performance of Bicontinuous Nanoporous Graphene for Li-O2 Batteries. *Advanced Energy Materials* **2016,** *6* (3), n/a-n/a.

17. Li, S.; Wang, M.; Yao, Y.; Zhao, T.; Yang, L.; Wu, F., Effect of the Activation Process on the Microstructure and Electrochemical Properties of N-Doped Carbon Cathodes in Li–O2 Batteries. *ACS Applied Materials & Interfaces* **2019,** *11* (38), 34997-35004.

18. Li, F.; Zhu, M.; Luo, Z.; Guo, L.; Bian, Z.; Li, Y.; Luo, K., Nitrogen-doped graphene derived from polyaniline/graphene oxide composites with improved capacity and cyclic performance of Li-O2 battery. *J. Solid State Electrochem.* **2019,** *23* (8), 2391-2399.

19. Wang, H.; Maiyalagan, T.; Wang, X., Review on Recent Progress in Nitrogen-Doped Graphene: Synthesis, Characterization, and Its Potential Applications. *ACS Catalysis* **2012,** *2* (5), 781-794.

20. Deng, Y.; Xie, Y.; Zou, K.; Ji, X., Review on recent advances in nitrogen-doped carbons: preparations and applications in supercapacitors. *Journal of Materials Chemistry A* **2016,** *4* (4), 1144-1173.

21. Zhang, S.; Dokko, K.; Watanabe, M., Direct Synthesis of Nitrogen-Doped Carbon Materials from Protic Ionic Liquids and Protic Salts: Structural and Physicochemical Correlations between Precursor and Carbon. *Chem. Mater.* **2014,** *26* (9), 2915-2926.

22. Qu, K.; Zheng, Y.; Dai, S.; Qiao, S. Z., Polydopamine-graphene oxide derived mesoporous carbon nanosheets for enhanced oxygen reduction. *Nanoscale* **2015,** *7* (29), 12598-12605.

23. Qu, K.; Zheng, Y.; Dai, S.; Qiao, S. Z., Graphene oxide-polydopamine derived N, S-codoped carbon nanosheets as superior bifunctional electrocatalysts for oxygen reduction and evolution. *Nano Energy* **2016,** *19*, 373-381.

24. Lin, X.; Yuan, R.; Cai, S.; Jiang, Y.; Lei, J.; Liu, S.-G.; Wu, Q.-H.; Liao, H.-G.; Zheng, M.; Dong, Q., An Open-Structured Matrix as Oxygen Cathode with High Catalytic Activity and Large Li2O2 Accommodations for Lithium–Oxygen Batteries. *Advanced Energy Materials* **2018,** *8* (18), 1800089.

25. Xiao, J.; Mei, D.; Li, X.; Xu, W.; Wang, D.; Graff, G. L.; Bennett, W. D.; Nie, Z.; Saraf, L. V.; Aksay, I. A.; Liu, J.; Zhang, J.-G., Hierarchically Porous Graphene as a Lithium–Air Battery Electrode. *Nano Lett.* **2011,** *11* (11), 5071-5078.

26. Wang, Z. L.; Xu, D.; Xu, J. J.; Zhang, L. L.; Zhang, X. B., Graphene Oxide Gel-Derived, Free-Standing, Hierarchically Porous Carbon for High-Capacity and High-Rate Rechargeable Li-O2 Batteries. *Adv. Funct. Mater.* **2012,** *22* (17), 3699-3705.

27. Kichambare, P.; Rodrigues, S.; Kumar, J., Mesoporous Nitrogen-Doped Carbon-Glass Ceramic Cathodes for Solid-State Lithium–Oxygen Batteries. *ACS Applied Materials & Interfaces* **2012,** *4* (1), 49-52.

28. Soavi, F.; Monaco, S.; Mastragostino, M., Catalyst-free porous carbon cathode and ionic liquid for high efficiency, rechargeable Li/O-2 battery. *J. Power Sources* **2013,** *224*, 115-119.

29. He, M.; Zhang, P.; Liu, L.; Liu, B.; Xu, S., Hierarchical porous nitrogen doped three-dimensional graphene as a free-standing cathode for rechargeable lithium-oxygen batteries. *Electrochim. Acta* **2016,** *191*, 90-97.

30. Shui, J. L.; Lin, Y.; Connell, J. W.; Xu, J. T.; Fan, X. L.; Dai, L. M., Nitrogen-Doped Holey Graphene for High-Performance Rechargeable Li-O-2 Batteries. *Acs Energy Letters* **2016,** *1* (1), 260-265.

31. Sun, B.; Huang, X.; Chen, S.; Munroe, P.; Wang, G., Porous Graphene Nanoarchitectures: An Efficient Catalyst for Low Charge-Overpotential, Long Life, and High Capacity Lithium–Oxygen Batteries. *Nano Lett.* **2014,** *14* (6), 3145-3152.

32. Zhao, C.; Yu, C.; Liu, S.; Yang, J.; Fan, X.; Huang, H.; Qiu, J., 3D Porous N-Doped Graphene Frameworks Made of Interconnected Nanocages for Ultrahigh-Rate and Long-Life Li-O2Batteries. *Adv. Funct. Mater.* **2015,** *25* (44), 6913-6920.

33. Wang, D.-W.; Li, F.; Liu, M.; Lu, G. Q.; Cheng, H.-M., 3D Aperiodic Hierarchical Porous Graphitic Carbon Material for High-Rate Electrochemical Capacitive Energy Storage. *Angew. Chem. Int. Ed.* **2008,** *47* (2), 373-376.

34. Li, B.; Yang, X.; Xia, L.; Majeed, M. I.; Tan, B., Hollow Microporous Organic Capsules. **2013,** *3*, 2128.

35. Sing, K. S. W. e. a., Reporting Physisorption Data for Gas/Solid Systems with Special Reference to the Determination of Surface Area and Porosity. *Pure & Appl. Chem* **1985,** (57), 603-619.

36. Ferrari, A. C.; Meyer, J. C.; Scardaci, V.; Casiraghi, C.; Lazzeri, M.; Mauri, F.; Piscanec, S.; Jiang, D.; Novoselov, K. S.; Roth, S.; Geim, A. K., Raman Spectrum of Graphene and Graphene Layers. *Phys. Rev. Lett.* **2006,** *97* (18), 187401.

37. Zhang, C.; Fu, L.; Liu, N.; Liu, M.; Wang, Y.; Liu, Z., Synthesis of Nitrogen-Doped

Graphene Using Embedded Carbon and Nitrogen Sources. *Adv. Mater.* **2011,** *23* (8), 1020-1024.

38. Liu, X.; Amiinu, I. S.; Liu, S.; Cheng, K.; Mu, S., Transition metal/nitrogen dual-doped mesoporous graphene-like carbon nanosheets for the oxygen reduction and evolution reactions. *Nanoscale* **2016,** *8* (27), 13311-13320.

39. Susi, T.; Pichler, T.; Ayala, P., X-ray photoelectron spectroscopy of graphitic carbon nanomaterials doped with heteroatoms. *Beilstein Journal of Nanotechnology* **2015,** *6*, 177-192.

40. Xue, Y.; Liu, J.; Chen, H.; Wang, R.; Li, D.; Qu, J.; Dai, L., Nitrogen-Doped Graphene Foams as Metal-Free Counter Electrodes in High-Performance Dye-Sensitized Solar Cells. *Angew. Chem. Int. Ed.* **2012,** *51* (48), 12124-12127.

41. Zhang, C.; Hao, R.; Liao, H.; Hou, Y., Synthesis of amino-functionalized graphene as metal-free catalyst and exploration of the roles of various nitrogen states in oxygen reduction reaction. *Nano Energy* **2013,** *2* (1), 88-97.

42. Liu, G.; Li, X.; Lee, J.-W.; Popov, B. N., A review of the development of nitrogen-modified carbon-based catalysts for oxygen reduction at USC. *Catalysis Science & Technology* **2011,** *1* (2), 207-217.

43. Liu, G. X.; Chen, H. B.; Xia, L.; Wang, S. Q.; Ding, L. X.; Li, D. D.; Xiao, K.; Dai, S.; Wang, H. H., Hierarchical Mesoporous/Macroporous Perovskite La0.5Sr0.5CoO3-x Nanotubes: A Bifunctional Catalyst with Enhanced Activity and Cycle Stability for Rechargeable Lithium Oxygen Batteries. *Acs Applied Materials & Interfaces* **2015,** *7* (40), 22478-22486.

44. Li, Z.; Jiang, Q.; Ma, Z.; Liu, Q.; Wu, Z.; Wang, S., Oxygen plasma modified separator for lithium sulfur battery. *RSC Advances* **2015,** *5* (97), 79473-79478.

45. Sennu, P.; Christy, M.; Aravindan, V.; Lee, Y.-G.; Nahm, K. S.; Lee, Y.-S., Two-Dimensional Mesoporous Cobalt Sulfide Nanosheets as a Superior Anode for a Li-Ion Battery and a Bifunctional Electrocatalyst for the Li–O2 System. *Chem. Mater.* **2015,** *27* (16), 5726-5735.

46. Zhang, J.; Li, P.; Wang, Z.; Qiao, J.; Rooney, D.; Sun, W.; Sun, K., Three-dimensional graphene-Co3O4 cathodes for rechargeable Li-O2 batteries. *Journal of Materials Chemistry A* **2015,** *3* (4), 1504-1510.

47. Lu, Y.-C.; Shao-Horn, Y., Probing the Reaction Kinetics of the Charge Reactions of Nonaqueous Li–O2 Batteries. *The Journal of Physical Chemistry Letters* **2013,** *4* (1), 93-99.

48. Yang, J.; Zhai, D.; Wang, H.-H.; Lau, K. C.; Schlueter, J. A.; Du, P.; Myers, D. J.; Sun, Y.-K.; Curtiss, L. A.; Amine, K., Evidence for lithium superoxide-like species in the discharge product of a Li-O2 battery. *PCCP* **2013,** *15* (11), 3764-3771.

49. Galiote, N. A.; Jeong, S.; Morais, W. G.; Passerini, S.; Huguenin, F., The Role of Ionic Liquid in Oxygen Reduction Reaction for Lithium-air Batteries. *Electrochim. Acta* **2017,** *247*

(Supplement C), 610-616.

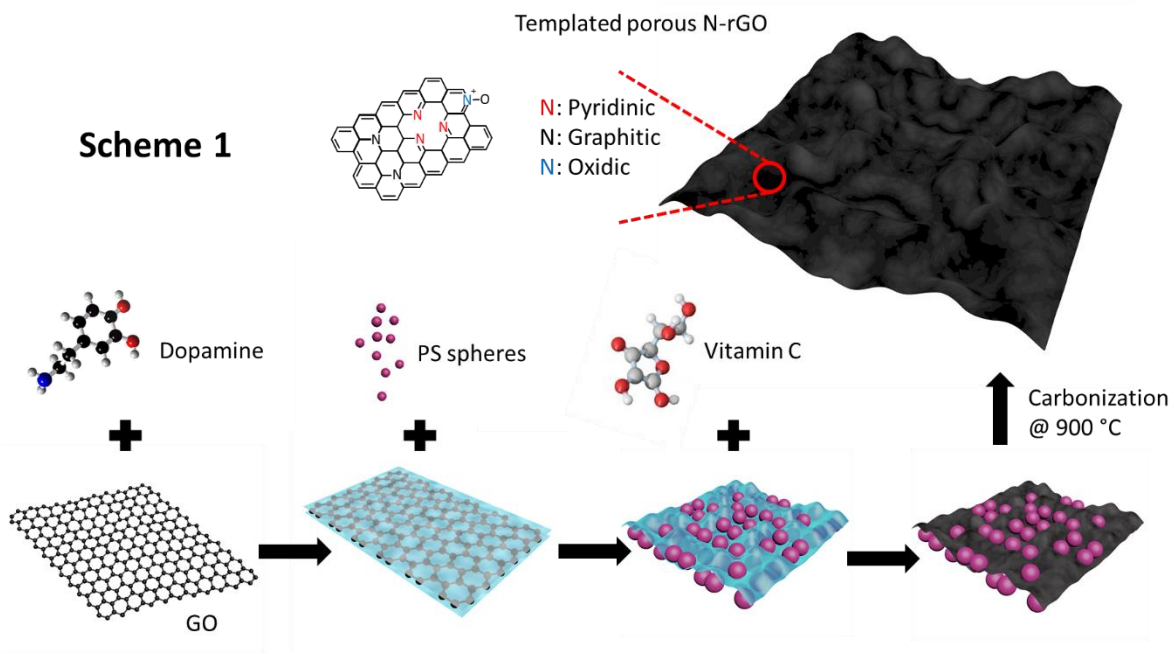

Scheme 1. Synthesis of polydopamine derived N doped reduce graphene oxide with controlled pores.

Supporting Information

Polydopamine Derived N-doped Graphene Electrodes with Controlled Pores for High-Capacity Rechargeable Li-O_2 Batteries

Qi Bi,[1] Guoxue Liu,[2] Heng Wang,[1] Yanting Yin,[3] Gunther Andersson,[3] Haihui Wang, *[, 1, 2]

and Sheng Dai*[, 1, 4]

[1] School of Chemical Engineering and Advanced Materials, The University of Adelaide, South Australia 5005, Australia

[2] School of Chemistry & Chemical Engineering, South China University of Technology, 381 Wushan Road, Guangzhou 510640, China

[3] School of Chemical and Physical Sciences, Flinders University, Adelaide SA 5001, Australia

[4] Department of Chemical Engineering, Brunel University London, Uxbridge, UB8 3PH, United Kingdom

*Corresponding authors

Email: hhwang@scut.edu.cn; s.dai@adelaide.edu.au

Experimental Section

Preparation of Reduced Graphene Oxide (rGO): Graphite flakes were oxidized using an improved Hummer's method. 3 g graphite was added to a mixture of concentrated H_2SO_4/H_3PO_4 (360:40 ml), followed by the addition of 18 g $KMnO_4$. The reaction mixture was heated to 50 °C and stirred for 12 h. The reaction mixture was cooled to room temperature and poured into 400 ml ice water with the addition of H_2O_2 (30%, 10 ml). The mixture was then filtered over a 0.45 µm PTFE membrane and washed with 200 ml of 30 % HCl and 1 L water to obtain graphite oxide. Exfoliation of the above graphite oxide was achieved by ultrasonication of diluted graphite oxide dispersion for 30 min, followed by freeze drying to obtain graphene oxide (GO) powder.

Reduced graphene oxide (rGO) was obtained by reducing GO powder in a temperature programmable tube furnace under N_2 environment at 800 °C for 3 h with a heating rate of 5 °C min^{-1}.

Preparation of monodisperse polystyrene spheres: In a typical synthesis for 170 nm PS spheres, 35 g Milli-Q water was mixed with 0.05 g sodium dodecyl sulphate (SDS) and 5 g styrene monomer, the mixture was degassed for 30 min and then heated to 70 °C. 0.05 g potassium peroxydisulfate (KPS) in 10 g water were added to the mixture to initiate polymerization. The reaction was lasted overnight to get polystyrene spheres, and purified by dialysis again water at room temperature. The 230 and 410 nm PS spheres were prepared according to the same procedure but changing the SDS amount to 0.03 and 0.01 g.

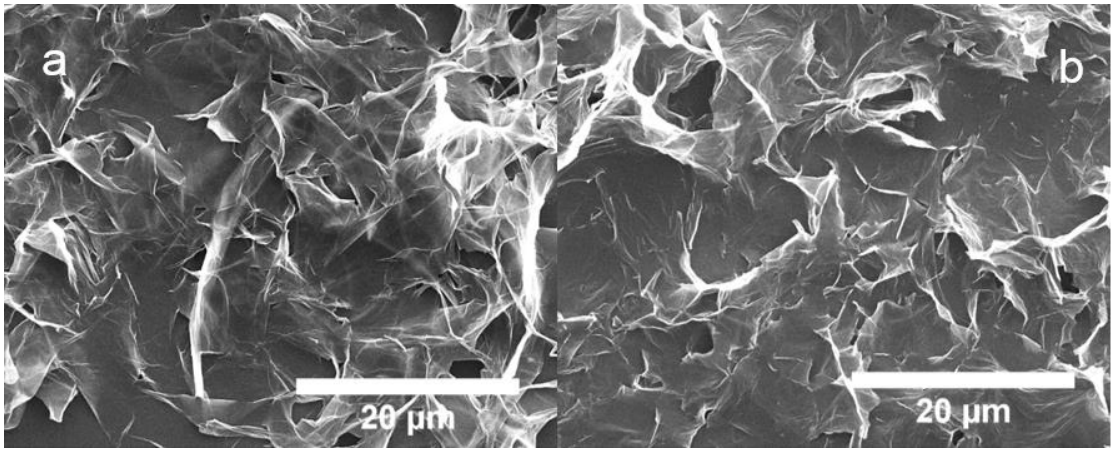

Figure 3.S1. SEM images of (a) rGO, (b) N-rGO.

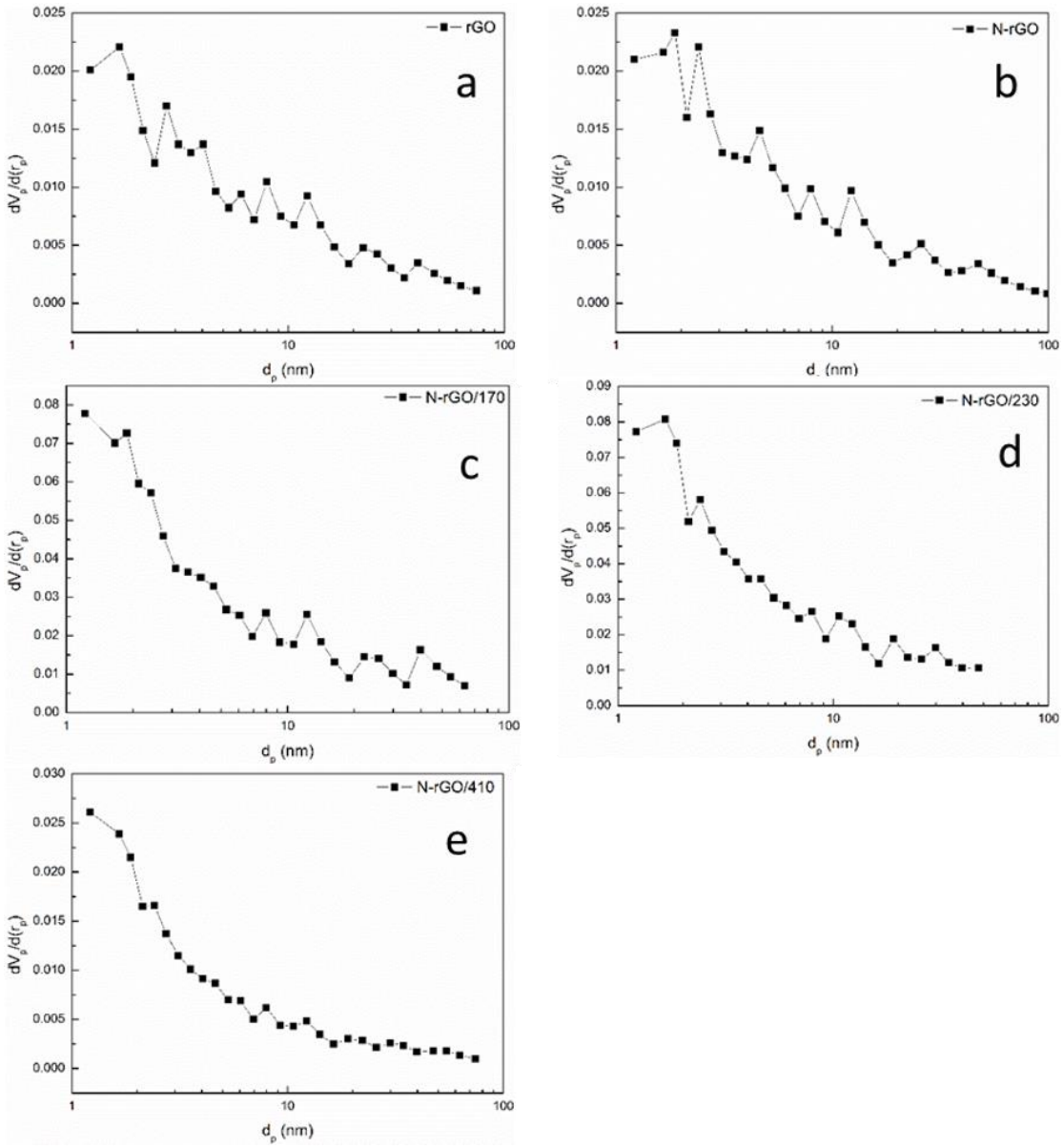

Figure 3.S2. Pore size distributions of (a) rGO, (b) N-rGO, (c) N-rGO/170, (d) N-rGO/230 and (e) N-rGO/410.

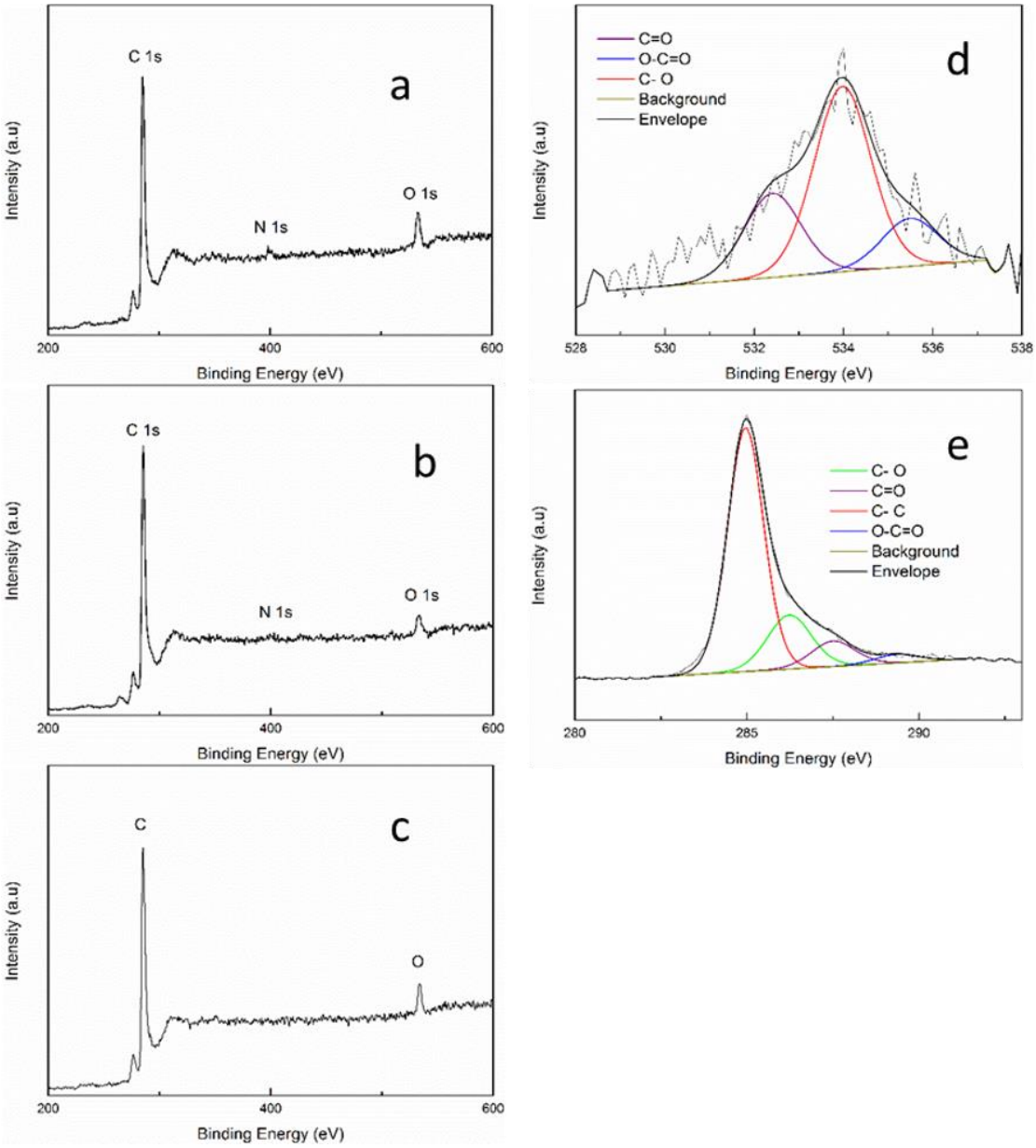

Figure 3.S3. XPS elemental survey of (a) N-rGO, (b) N-rGO/170 and (c) rGO. XPS spectra of (d) O 1s of rGO and (e) C 1s of rGO.

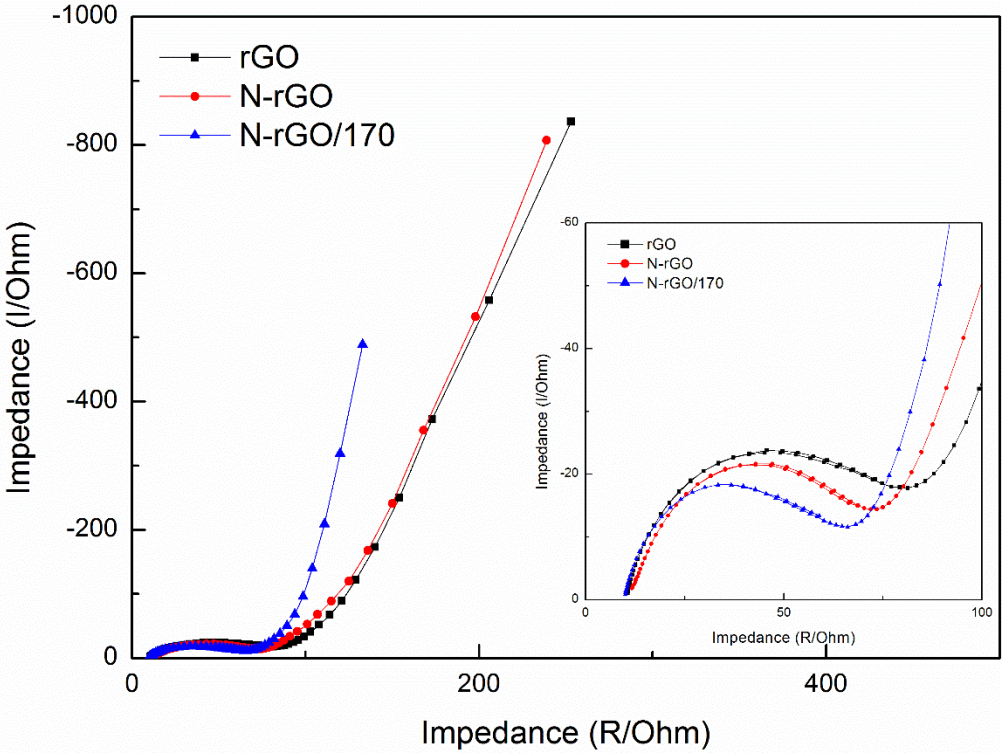

Figure 3.S4. EIS plots of rGO, N-rGO and N-rGO/170.

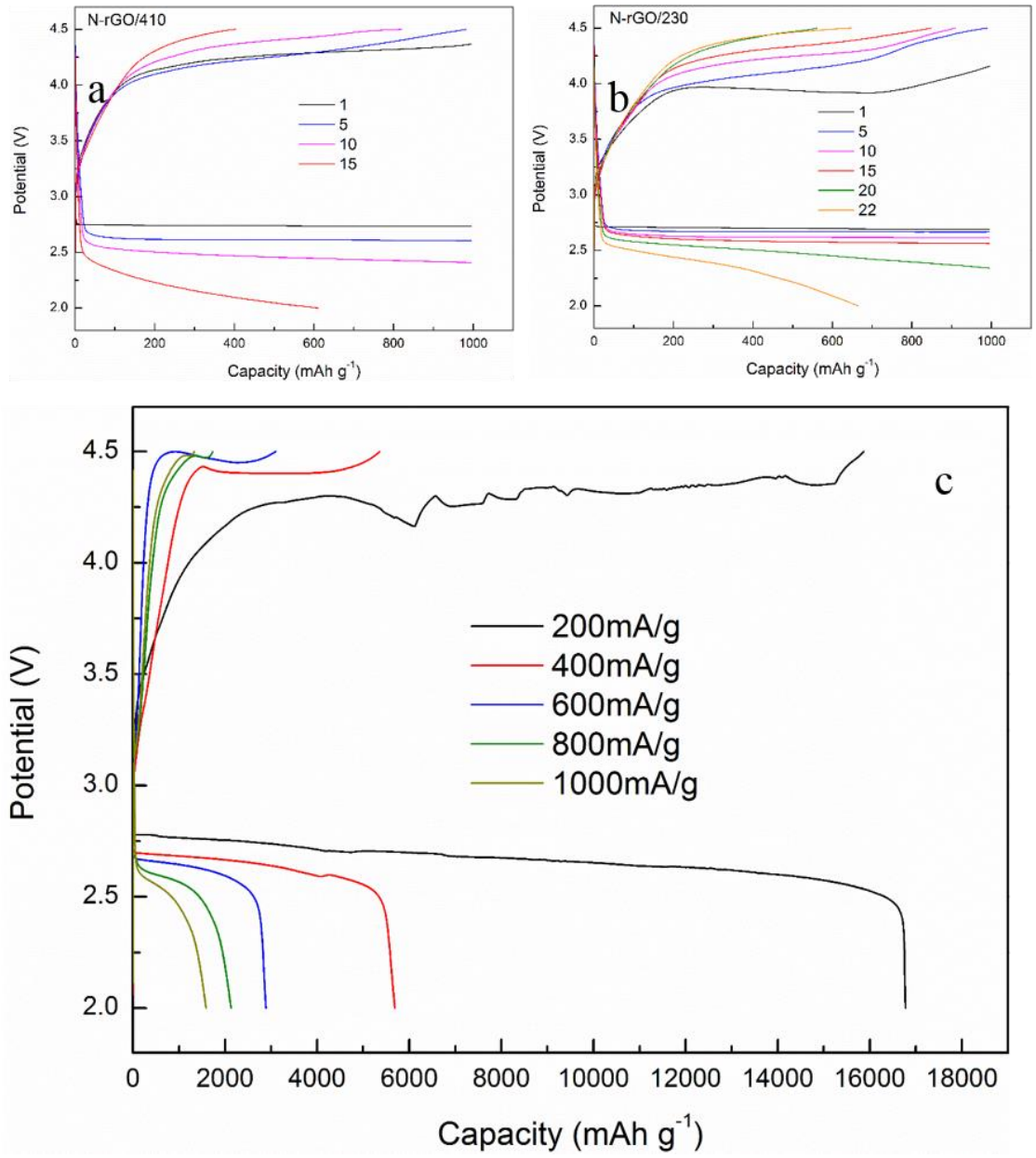

Figure 3.S5. Cycle performance of (a) N-rGO/410 and (b) N-rGO/230 at a current density of 200 mA g^{-1} with an upper-limit capacity of 1000 mA h g^{-1}. (c) The Galvanostatic discharge/charge curves of Li-O2 batteries with the N-rGO/170 electrode at various current densities.

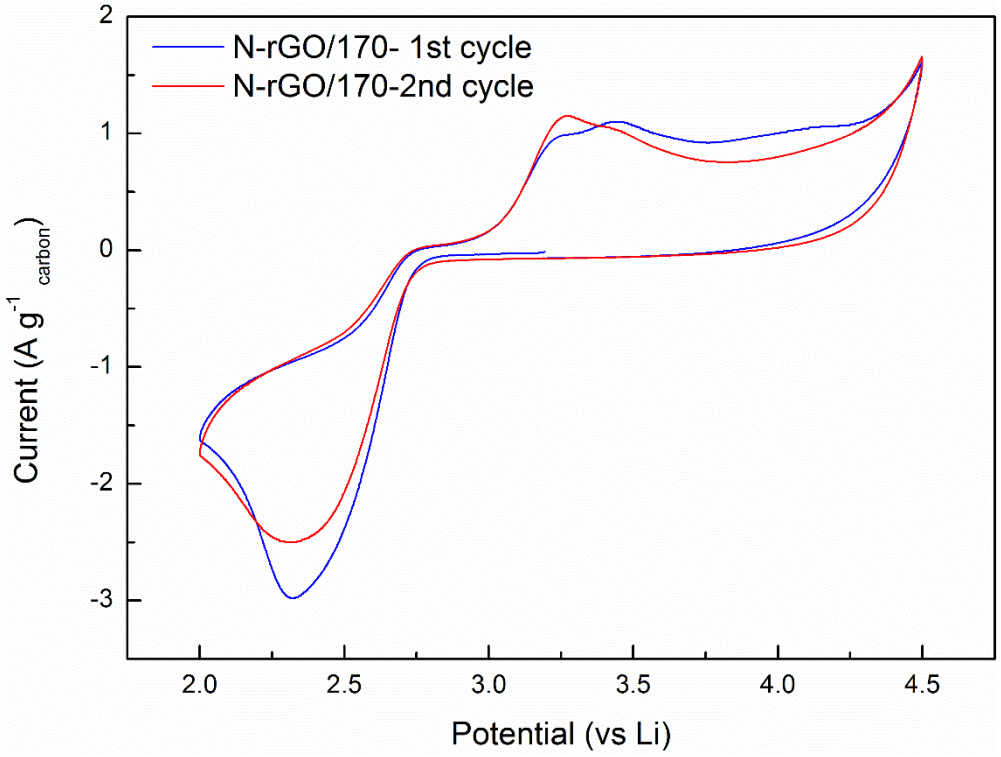

Figure 3.S6. Comparison on the CV curves of the N-rGO/170 (first and second cycle operation) at a scanning rate of 1 mV s^{-1}.

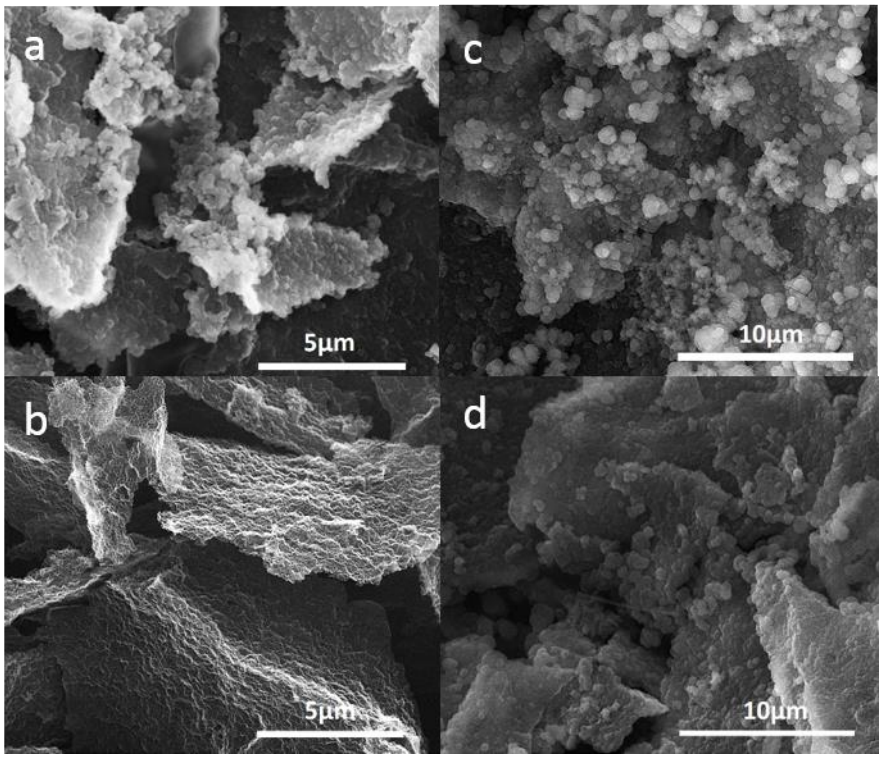

Figure 3.S7. (a, b) N-rGO/170 after 1st cycle discharge, and recharge with 1000 mA h g^{-1} at 200 mA g^{-1}; (c, d) N-rGO/170 after 20th cycle discharge, and recharge with 1000 mA h g^{-1} at 200 mA g^{-1}.

Table 3.S1. Comparison on the electrochemical performance of recently reported N doped carbon electrodes for Li-O2 batteries.

Cathode Materials	Electrolyte	BET surface area ($m^2 g^{-1}$)/ Pore volume ($cm^3 g^{-1}$)	Current Density	Maximum Capacity (mA h g^{-1})	Upper-limit Capacity (mA h g^{-1})	Cyclic Performance	Reference
N-rGO/170	LiTFSI/TEGDME	449/1.00	200 mA g^{-1}	16777	1000	26 cycles at 200 mA g^{-1}	This work
N-CNTs (3.92% N)	$LiPF_6$/DMSO	- /-	0.1 mA cm^{-2}	7906	About 2300	26 cycles at 0.3 mA cm^{-2}	S1
NPGAs	LiTFSI/TEGDME	344/-	200 mA g^{-1}	10081	1000	72 cycles at 300 mA g^{-1}	S2
BMP_yKB	LiTFSI/TEGDME	642/1.30	25 mA g^{-1}	12370	-	-	S3
Hierarchical porous N-3D-G	$LiCF_3SO_3$/TEGDME	137/0.42	50 mA g^{-1}	7300	500	21 cycles at 100 mA g^{-1}	S4
N-onion like carbon	LiTFSI/TEGDME	358/-	0.15 mA cm^{-2}	12180	1000	194 cycles at 0.3 mA cm^{-2}	S5
N-holey graphene	$LiCF_3SO_3$/TEGDME	-/-	100 mA g^{-1}	17000	800	100 cycles @40 mA g^{-1}	S6
N-G/CNT	LiTFSI/TEGDME	452/-	500 mA g^{-1}	Over 8000	1000	400 cycles at 500 mA g^{-1}	S7
Nanoporous NG	LiTFSI/TEGDME	772/-	200 mA g^{-1}	10400	1000	100 cycles at 300 mA g^{-1}	S8

S1. R. Mi, S. Li, X. Liu, L. Liu, Y. Li, J. Mei, Y. Chen, H. Liu, H. Wang, H. Yana and W. M. Lau, J Mater Chem A, 2014, 2, 18746-18753.

S2. C. Zhao, C. Yu, S. Liu, J. Yang, X. Fan, H. Huang and J. Qiu, Adv Funct Mater, 2015, 25, 6913-6920.

S3. H. Lin, Z. X. Liu, Y. Mao, X. J. Liu, Y. Q. Fang, Y. Liu, D. Y. Wang and J. Y. Xie, Carbon, 2016, 96, 965-971.

S4. M. He, P. Zhang, L. Liu, B. Liu and S. Xu, Electrochim Acta, 2016, 191, 90-97.

S5. C. Shu, Y. Lin and D. Su, J. Mater. Chem. A, 2016, 4, 2128-2136.

S6. J. Shui, Y. Lin, J. W. Connell, J. Xu, X. Fan and L. Dai, ACS Energy Letters, 2016, 1, 260-265.

S7. C. Shu, B. Li, B. Zhang and D. Su, Chemsuschem, 2015, 8, 3973-3976.

S8. J. Han, X. Guo, Y. Ito, P. Liu, D. Hojo, T. Aida, A. Hirata, T. Fujita, T. Adschiri, H. Zhou and M. Chen, Adv. Energy Mater., 2016, 6, 1501870

Chapter 4 Phase-Controlled Synthesis of Cobalt Sulfide as an Effective Bifunctional Catalyst for Long Cycle Life Li-O_2 Batteries

4.1 Introduction and Significance

Cobalt sulfides are effective catalysts towards oxygen reduction reaction (ORR) and oxygen evolution reaction (OER) with various phases available. However, they are rarely applied as cathode materials in Li-O_2 batteries. On the other hand, the morphologies of discharge product Li_2O_2 have been found to determine the ORR and OER pathways of Li-O_2 batteries. The crystalline Li_2O_2 is favourable in discharge process for large capacity, while amorphous Li_2O_2 is preferred during charge for fast decomposition and cycling stability. In this work, we boosted both discharge specific capacity and cycling stability of Li-O_2 batteries by exploring the influence of cobalt sulfides at different phases on the morphologies of Li_2O_2. The highlights of this work include:

(a) For the first time, control-phased cobalt sulfides were prepared and mixed with N-rGO as cathode materials for Li-O_2 batteries.

(b) This work systematically investigated the battery performance of different phases of cobalt sulfides, including single and dual-phase cobalt sulfides.

(c) Both crystalline and amorphous Li_2O_2 were formed on a dual-phase cobalt sulfide cathode contains both CoS and Co_9S_8, which was proved to improve the Li-O_2 battery performance in both discharge and charge processes.

4.2 Phase-Controlled Synthesis of Cobalt Sulfide as an Effective Bifunctional Catalyst for Long Cycle Life Li-O_2 Batteries

This section is included as an un-submitted manuscript by Qi Bi, Heng Wang, Haihui Wang and Sheng Dai.

Statement of Authorship

Title of Paper	Phase-Controlled Synthesis of Cobalt Sulfide as an Effective Bifunctional Catalyst for Long Cycle Life Li-O2 Batteries
Publication Status	☐ Published ☐ Accepted for Publication ☐ Submitted for Publication ☑ Unpublished and Unsubmitted work written in manuscript style
Publication Details	To be submitted.

Principal Author

Name of Principal Author (Candidate)	Qi Bi
Contribution to the Paper	Designed research plan; performed experiments, material characterizations, and battery performance evaluations; analysed data; wrote and edited manuscript.
Overall percentage (%)	85%
Certification:	This paper reports on original research I conducted during the period of my Higher Degree by Research candidature and is not subject to any obligations or contractual agreements with a third party that would constrain its inclusion in this thesis. I am the primary author of this paper.
Signature	Date 15/10/2019

Co-Author Contributions

By signing the Statement of Authorship, each author certifies that:

i. the candidate's stated contribution to the publication is accurate (as detailed above);

ii. permission is granted for the candidate in include the publication in the thesis; and

iii. the sum of all co-author contributions is equal to 100% less the candidate's stated contribution.

Name of Co-Author	Heng Wang
Contribution to the Paper	Discussed the research plan.
Signature	Date 15/10/2019

Name of Co-Author	Haihui Wang
Contribution to the Paper	Co-supervised the research.
Signature	Date 18/10/2019

Name of Co-Author	Sheng Dai		
Contribution to the Paper	Supervised the research and revised the manuscript.		
Signature		Date	15/10/2019

Please cut and paste additional co-author panels here as required.

Phase-Controlled Synthesis of Cobalt Sulfide as an Effective Bifunctional Catalyst for Long Cycle Life Li-O_2 Batteries

Qi Bi, Heng Wang, Haihui Wang, and Sheng Dai**

Q. Bi, H. Wang, Prof. H. Wang, Prof. S. Dai
School of Chemical Engineering
The University of Adelaide
Adelaide SA 5005 Australia

Prof. H. Wang
School of Chemistry & Chemical Engineering
South China University of Technology
Guangzhou 510640 China

Prof. S. Dai
Department of Chemical Engineering
Brunel University London
Uxbridge UB8 3PH United Kingdom

* Corresponding author

E-mail: hhwang@scut.edu.cn

sheng.dai@brunel.ac.uk

Abstract

As one of the most promising next generation energy storage systems, the implementation of lithium-oxygen (Li-O_2) batteries is strongly hindered by limited capacity and poor cycle ability caused by sluggish oxygen redox kinetics, inferior Li_2O_2/cathode contact interface, and difficult oxygen transport. In this study, we present an approach to prepare cobalt sulfides with different phases by simply tuning the decomposition temperature of cobalt thiourea complex. Single phase and dual phase of cobalt sulfides contain both CoS and Co_9S_8 (CoS-900) were synthesized and then mixed with N doped graphene as oxygen cathodes for Li-O_2 batteries. The excellent catalytic activity and stability for oxygen redox as well as the presence of both crystalline and amorphous Li_2O_2 significantly improve the electrochemical performance of Li-O_2 batteries. As a result, the Li-O_2 battery with CoS-900@NG catalyst can deliver a high discharge capacity of 7410 mA h g^{-1} at 200 mA g^{-1} with 100 % recovery of charge capacity and a super long cycle life for 108 cycles under a cut-off capacity of 500 mA h g^{-1}, outperforming most current cobalt-sulfide-based cathodes.

Keywords: dual-phase cobalt sulfides, lithium oxygen batteries, long cycle life, film-like Li_2O_2

Introduction

Non-aqueous rechargeable Li-O_2 batteries have been considered as an attractive storage system for next generation electric vehicles and portable devices due to their super high theoretical gravimetric energy densities.[1-2] However, practical implementation of these Li-O_2 batteries is hindered by their low energy efficiency and poor battery cycle life. As one of the most important components in Li-O_2 batteries, an oxygen electrode can influence battery performance in two ways, the catalytic performance and the storage of discharge products. The sluggish oxygen reduction reaction (ORR) during the discharge process limits discharge capacity, while the inactive oxygen evolution reaction (OER) during the charge process not only increases overpotential but also results in poor cycle performance.[2] Meanwhile, the accumulation of insoluble discharge products of Li_2O_2 and other by-products on oxygen electrode also gradually decays battery performance by obstructing active catalytic sites and diffusion pathways for oxygen and electrolyte.[3] These factors are interrelated and interplayed which can be explained by the mechanism of the Li-O_2 batteries.

$$2Li^+ + O_2 + 2e^- \leftrightarrow Li_2O_2 \quad (4.1)$$

$$O_2\,(g) + Li^+ + e^- \rightarrow LiO_2 \quad (4.2)$$

$$2LiO_2 \rightarrow Li_2O_2\,(s) + O_2 \quad (4.3)$$

$$LiO_2 + Li^+ + e^- \rightarrow Li_2O_2\,(s) \quad (4.4)$$

Though the ORR process can be simply defined in Reaction 4.1, the high entropic barriers makes it unlikely to occur. During discharge, several possible reactions occur at the oxygen electrode via ORR. At the beginning, oxygen is reduced on electrode surface and combines with the Li^+ that dissolved in electrolyte to from LiO_2 (Reaction 4.2). Then, LiO_2 may undergo two different pathways to form Li_2O_2: either to form Li_2O_2 crystalline through the solution pathway by a disproportionation reaction due to the instability of LiO_2 (Reaction 4.3), or to form amorphous Li_2O_2 films through the surface pathway by one electron transfer electrochemical process (Reaction 4.4) [4-5]. The OER mechanism of Li-O_2 batteries undergoes

different pathways according to the morphologies of Li_2O_2.

High electronic conductivity of amorphous Li_2O_2 accelerates the electrochemical decomposition of Li_2O_2 and improves OER polarization [6-7]. The large contact areas between electrode and film-like Li_2O_2 also effectively promote the OER kinetics and therefore to achieve a low charge voltage [8]. During charge, the decomposition of Li_2O_2 film on oxygen electrode can create voids at interface. The voids would be then filled by the collapse of Li_2O_2 particles, and the reaction continued to full decomposition [9]. However, crystalline Li_2O_2 (toroidal, red-blood-like, and spherical Li_2O_2) potentially hinders charge transport due to its poor electronic conductivity [10]. The decomposition of large crystalline Li_2O_2 particles is difficult due to the slow charge transfer caused by the electrical insulation of crystalline Li_2O_2 [6, 11-12], which further results in a high charge overpotential and an inferior OER performance [13-14].

Due to the good electrical conductivity and low-cost, lightweight graphene-based materials are widely used as cathode materials in Li-O_2 systems [15-18]. Particularly, the N doped graphene exhibits great catalytic activity towards ORR and notably improves the discharge capacity of Li-O_2 batteries, though the instability during the oxidation of Li_2O_2 leads to an inferior OER performance.[19-25] Apart from expensive precious metals, transition metal compounds have also been widely investigated as cost-effective electrocatalysts and shown excellent electrocatalytic abilities towards ORR/ OER [26-30]. Transition metal sulfides, compared with oxides, can increase the intrinsic electro-conductivity of materials besides keeping their superb OER activities [31]. Among them, cobalt sulfides with various phases of CoS, CoS_2, Co_3S_4 and Co_9S_8 have been found to be efficient as the electrocatalysts for fuel cells, [32] supercapacitors, [33-34] solar cells,[35-36] and lithium ion batteries [37-42]. However, the exploration of cobalt sulfide as the catalysts in Li-O_2 batteries is limited to very few reports, and all of the reported cobalt sulfides are in single phase [43-46]. Among previous studies, Co_9S_8 is one of the most investigated cobalt sulfides. Both structured Co_9S_8 matrix and Co_9S_8@carbon porous nanocages demonstrated great cycle performance in Li-O_2 battery [43, 45]. A Co_3S_4–nanosheet composite, on the other hand, presented better performance on specific capacity [46].

Herein, inspired by the various catalytic activities of cobalt sulfides in different phases, we successfully synthesized control-phase cobalt sulfide through a thermal decomposition method. The prepared cobalt sulfide was mixed with N-rGO to systematically explore the electrocatalytic performance of cobalt sulfide with different phases in Li-O_2 systems. One of the dual-phase cobalt sulfide cathode material CoS-900@NG presented significant battery performance improvement in both specific capacity and cycle stability, compared with single phase cobalt sulfide cathode materials. We further studied the Li_2O_2 morphologies of CoS-900@NG, the existence of both Li_2O_2 crystalline and film is proven to interact with the ORR/OER catalytic nature of CoS-900@NG to achieve excellent battery performance.

Experimental section

Materials: Cobalt nitrate ($Co(NO_3)_2 \cdot 6H_2O$), thiourea, graphite flake (100 mesh), potassium permanganate ($KMnO_4$), phosphoric acid (H_3PO_4 85%), polydopamine, n-butanol and N-methyl-2-pyrrolidone (NMP) were purchased from Sigma-Aldrich. Sulfuric acid (H_2SO_4, 98%), hydrogen peroxide (H_2O_2, 30%), and polyvinylidene fluoride (PVDF) were supplied by Chem-Supply. Glass fiber membrane (Grade GF/F) was from Whatman. Lithium foil was supplied by China Energy Lithium Co., Ltd. 1 M lithium bis(trifluoromethanesulfonyl)imide (LiTFSI) in tetraethylene glycol dimethyl ether (TEGDME) was from Suzhou Qianmin Chemical Reagent Co., Ltd. Ultra-high purity (99.999%) O_2 was acquired from Coregas, Australia.

Synthesis of cobalt sulfides: Cobalt nitrate ($Co(NO_3)_2 \cdot 6H_2O$, 0.01 M) was dissolved in 25 mL of hot n-butanol. Thiourea (0.04 M) was added, and the mixture was heated to reach boiling until all solids dissolved, associated with the solution change from red to blue. On cooling, blue solids of $Co(TU)_4(NO_3)_2$ were separated out. The blue solid was suction filtered, washed with diethyl ether and dried under vacuum at 30 °C. The cobalt thiourea complex was calcined in a tube furnace under N_2 atmosphere for 2 h at 400 °C, 600 °C, 900 °C, 1000 °C, respectively to form various cobalt sulfides marked as CoS-400, CoS-600, CoS-900, and CoS-1000.

Microstructural and chemical characterization: The field emission scanning electron

microscope (FESEM) images and mappings were obtained on a FEI Quanta 450, the transmission electron microscopy (TEM) images were acquired on a Tecnai G2 Spirit. X-ray diffraction (XRD) patterns were obtained on a Rigaku Miniflex 600 instrument using a Cu Kα radiation source.

Li-O_2 battery measurements: The oxygen electrodes were fabricated by coating the homogeneous slurry contained N-rGO, cobalt sulfide and polyvinylidene fluoride (PVDF) (weight ratio 6:3:1) in N-methyl-2-pyrrolidone (NMP) onto the Ni foam and dried at 80 °C overnight. The typical loading of the oxygen electrode is about 0.5 $mg_{(carbon)}$ cm^{-2}. The Li-O_2 batteries were assembled with 2032-type coin cells in an Ar filled glove box with a water and oxygen level less than 0.5 ppm. The Li-O_2 cells are established using a Li metal foil as the counter electrode and the anode, a glass fiber membrane separator, the as-prepared oxygen cathode, and 1 M LiTFSI in tetra (ethylene) glycol dimethyl ether (TEGDME) electrolyte. All measurements were conducted at 1 atm dry oxygen atmosphere. Galvanostatic discharge/recharge was tested on a Neware battery testing system within a voltage window of 2.0 – 4.5 V (Li/Li^+) after resting for 10 h at room temperature. Cyclic voltammetry (CV) tests were measured at a rate of 0.1 mV s^{-1} within the potential range of 2.0 to 4.5 V (Li/Li^+) by a CHI600 electrochemical workstation. Electrochemical impedance spectroscopy (EIS) were performed by a Zahner IM6 Electrochemical workstation in the frequency range of 0.1 Hz to 100 kHz.

Results and discussion

Cobalt sulfides at different phases were synthesized by the thermal decomposition of as-prepared cobalt thiourea complex in a tube furnace under N_2 atmosphere at 400, 600, 900 and 1000 °C for 2 h, and the resulting cobalt sulfides were named as the CoS-400, CoS-600, CoS-900 and CoS-1000. These cobalt sulfides were analyzed by X-ray diffraction (XRD) to elucidate their crystalline structures. For the CoS-400, the well-defined diffraction peaks at 2θ of 29.7°, 32.3°, 36.2°, 39.8°, 46.3°, 54.9°, 60.1°, 62.7° (Figure 4.1a) can be assigned to the

cubic phase CoS_2 with the space group $Pa\bar{3}$ (JCPDS, card No.41-1471). When the decomposition temperature increases to 600 °C (Figure 4.1b), the new peaks observed at 2θ of 30.5°, 35.2°, 46.9° and 54.2° indicate the presence of hexagonal CoS phase (space group $P6_3/mmc$) (JCPDS, card No.75-0605) along with CoS_2. When the temperature further increases to 900 °C, obvious phase changes are found in the XRD patterns of CoS-900 (Figure 4.1c), where the diffraction peaks indicating CoS_2 disappear and new peaks at 2θ of 31.1°, 39.5°, 47.6° and 51.9° can be assigned to Co_9S_8 (JCPDS, card No. 19-0364), which demonstrates the co-existence of Co_9S_8 with CoS phases. At 1000 °C (Figure 4.1d), the CoS peaks disappear and all the diffraction peaks are in good agreement with the crystalline data of pure Co_9S_8 with a cubic structure in space group $Fm\bar{3}m$ (JCPDS, card No. 19-0364).

The corresponding morphologies of cobalt sulfides in different phases were observed by a scanning electron microscopy (SEM) as shown in Figure 4.2, and obvious difference of particles as increasing decomposition temperatures can be observed. CoS-400 (Figure 4.2a) and CoS-600 (Figure 4.2b) present significant aggregation which is merged by spheroidal particles of ~2 and ~0.5 µm, respectively. While CoS-900 (Figure 4.2c) exhibits irregular morphology that is adhered by grain-like cobalt sulfide crystals with all average size of ~ 10 µm. In the case of CoS-1000 (Figure 4.2b), particles grow freely under high temperature and the average size can be more than 50 µm. The crystallite information reveals that the increment of particle size is associated with phase changes [47]. According to the XRD results, CoS-400 exhibits cubic structure CoS_2 with lattice parameter value of a = 5.538 Å (JCPDS, card No.41-1471), while the presence of hexagonal CoS phase with lattice parameter value of a = 3.38 Å and c = 5.16 Å (JCPDS, card No.75-0605) decreases the crystallite size of CoS-600. For CoS-900 and CoS-1000, the existence of cubic Co_9S_8 phase with a = 9.94 Å (JCPDS, card No. 19-0364) contributes to the increase sizes of these particles.

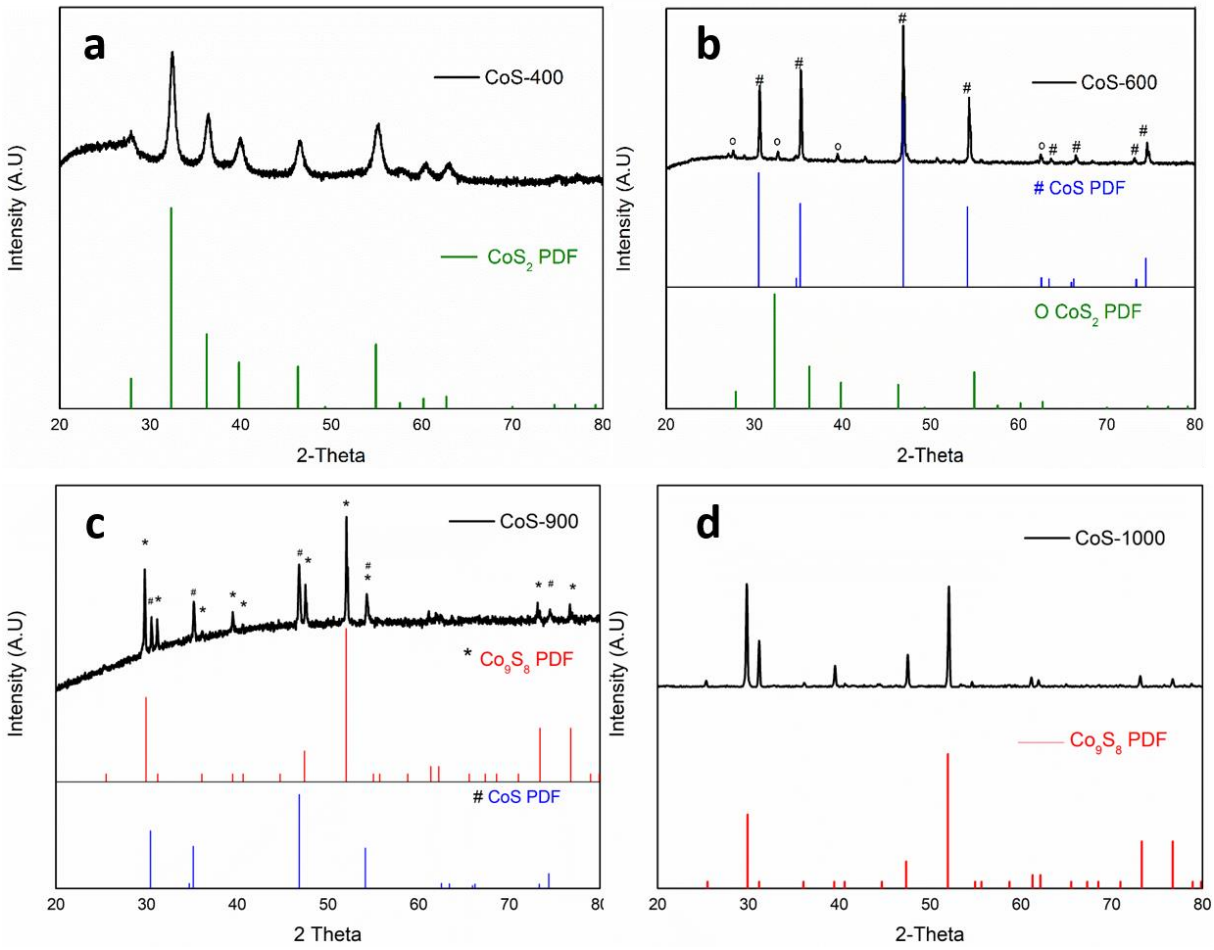

Figure 4.1. XRD patterns of (a) CoS-400, (b) CoS-600, (c) CoS-900 and (d) CoS-1000.

In the case of cobalt sulfide phases in CoS-900, high-resolution transmission electron microscopy (HRTEM) and Fast Fourier Transform (FFT) analysis were also used to elucidate the crystallite structure. As shown in Figure 4.3a, obvious fringes with interplanar spacing of 0.293 and 0.300 nm were observed, attributing to the (100) plane to CoS and the (311) plane to Co_9S_8, which further confirms the co-existence of both phases in CoS-900. The different growth directions in the diffraction area (marked in a red square) implies the existence of a mixture of crystalline structure of CoS-900, which is also proved by the corresponding FFT image shown in Figure 4.3b, where the (100) and (110) planes of CoS (marked in white) and the (440) plane of Co_9S_8 (marked in yellow) can be observed. Areas in the yellow square display the atom arrays of monocrystalline structure, as shown in the corresponding FFT image (Figure 4.3c), a cubic structure with d spacing of 0.287, 0.300 and 0.168 nm corresponding to the (222), (311) and (531) planes of Co_9S_8 phase.

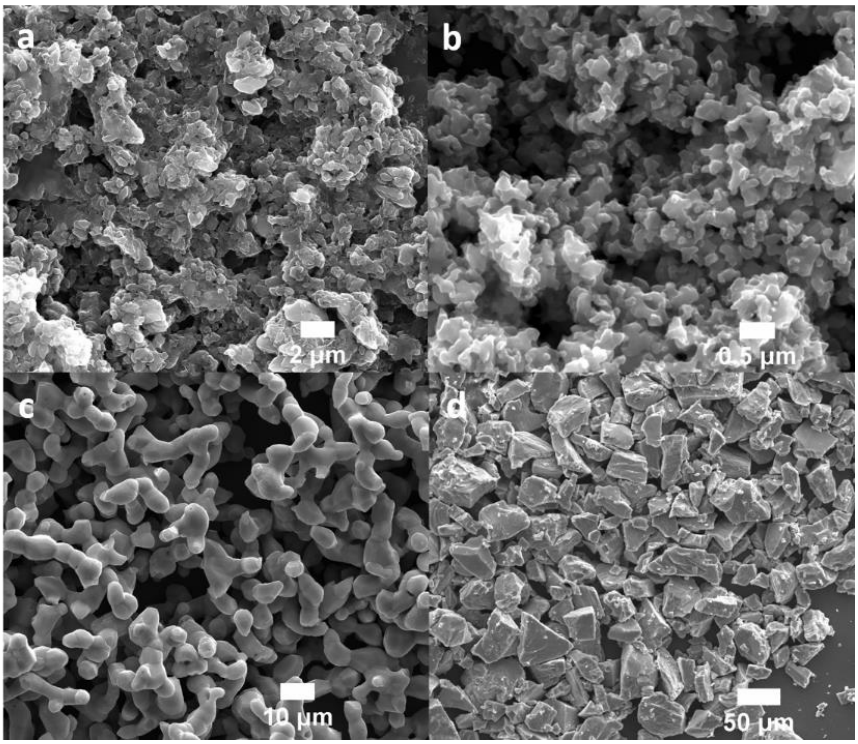

Figure 4.2. SEM images of (a) CoS-400, (b) CoS-600, (c) CoS-900, and (d) CoS-1000.

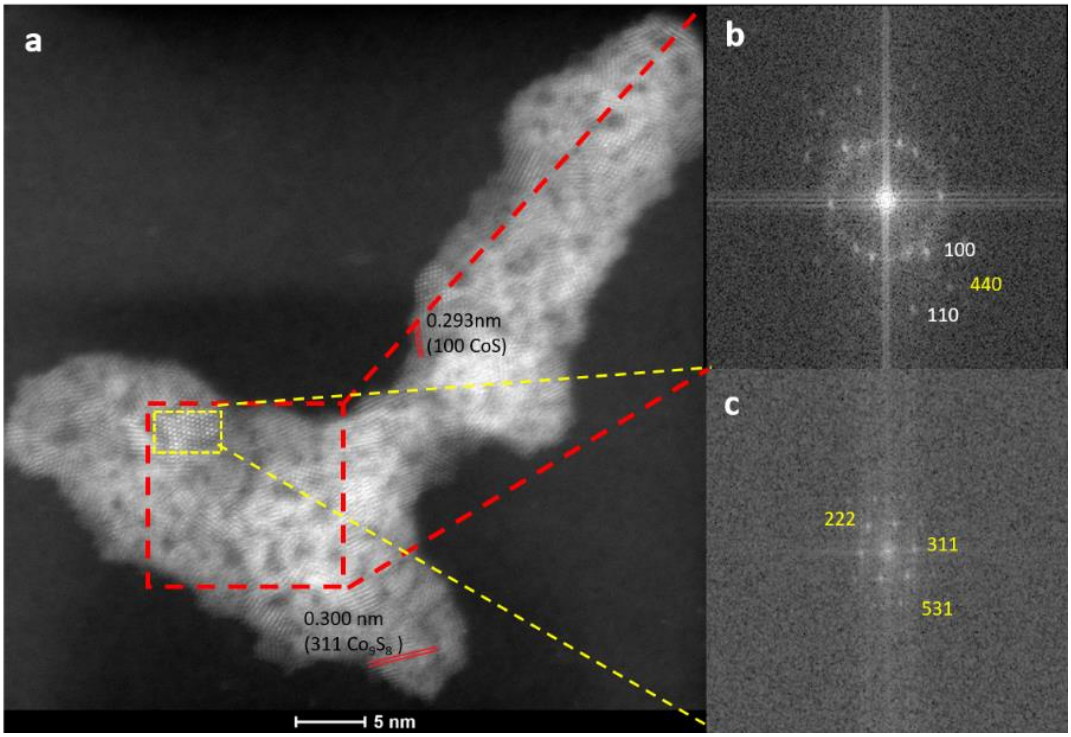

Figure 4.3. HRSTEM image of the (a) CoS-900; the Fast Fourier transform (FFT) analysis of (b) selected red square area and (c) selected yellow square area.

The as-prepared cobalt sulfides were used as the catalysts to be physically mixed with N-rGO and PVDF at a mass ratio of 3:6:1 and employed as oxygen cathodes in Li-O_2 coin cells to test

their electrochemical performance. The corresponding cathodes are noted as CoS-400@NG, CoS-600@NG, CoS-900@NG and CoS-1000@NG. The morphology and composition of oxygen cathodes were investigated by SEM and energy-dispersive X-ray (EDX) mapping. The mapping of corresponding carbon, sulfur, and cobalt are given in Figure 4.S1. The consistency of sulfur and cobalt identifies the spread of cobalt sulfide catalysts on N-rGO for all cathodes. Figure 4.4a compares the electrocatalytic activity of CoS-400@NG, CoS-600@NG, CoS-900@NG, and CoS-1000@NG in Li-O_2 batteries using cyclic voltammetry (CV) measurement. The operation potential window is within 2.0 - 4.5 V at a scan rate of 0.1 mV s^{-1}. For all these cathodes, the peak at ~ 2.3 V in the forward direction indicates the formation of Li_2O_2 during ORR. The current density at 2.3 V are in the following order: CoS-900@GN (-2.23 A $g^{-1}_{(carbon)}$) > CoS-400@GN (-1.55 A $g^{-1}_{(carbon)}$) > CoS-1000@GN (-0.89 A $g^{-1}_{(carbon)}$) > CoS 600@GN (-0.50 A $g^{-1}_{(carbon)}$). On the backward direction of CV curve, two obvious oxidation peaks at ~ 3.2 and ~3.4 V are the indication of the oxidation of LiO_2 and Li_2O_2 during OER [48]. The current density at these two oxidation peaks are in the following order: CoS-900@GN (0.79, 0.75 A $g^{-1}_{(carbon)}$) > CoS-400@GN (0.58, 0.58 A $g^{-1}_{(carbon)}$) > CoS-600@GN (0.32, 0.32 A $g^{-1}_{(carbon)}$) > CoS 1000@GN (0.16, 0.13 A $g^{-1}_{(carbon)}$). These results confirm CoS-900@NG the most active bi-functional catalytic performance towards both ORR and OER among all cathodes. Meanwhile, the good electrocatalytic ability of CoS-400@NG can be attributed to the S_2^{2-} pyrite structure within CoS_2, which is believed to be stable and favorable towards to ORR. Moreover, the sulfur rich surface is necessary to enhance the stability of CoS-400@NG by protecting the underlying material from dissolution to enhance both ORR and OER[49]. It is interesting to notice that CoS-600@NG exhibits the lowest current density among all the cathodes during ORR, but shows an improvement in the oxidation during OER process, which can be attributed to the fact that CoS-600 contains CoS phase, and Co^{4+} is viewed as the actually active sites participating in the OER process [50].

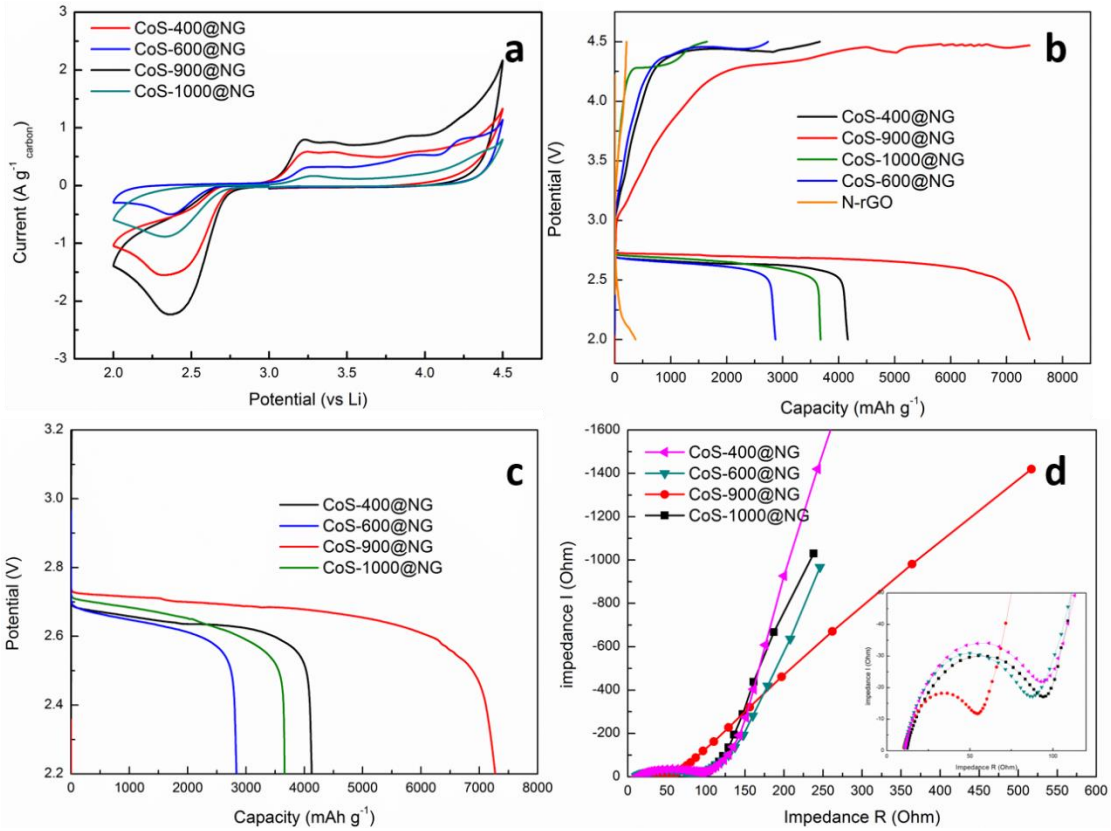

Figure 4.4. (a) CV curves of CoS-400@NG, CoS-600@NG, CoS-900@NG, and CoS-1000@NG at a constant scan rate of 1 mV s^{-1}; (b) Discharge-charge curves of Li-O_2 batteries with CoS-400@NG, CoS-600@NG, CoS-900@NG, CoS-1000@NG and N-rGO at a current density of 200 mA g^{-1}; (c) Discharge potential plateau after 1st full discharge, and (d) EIS before 1st discharge (d) of CoS-400@NG, CoS-600@NG, CoS-900@NG, and CoS-1000@NG.

The galvanostatic discharge – charge profiles of the N-rGO, CoS-400@NG, CoS-600@NG, CoS-900@NG and CoS-1000@NG cathodes is shown in Figure 4.4b. The specific capacity of each cell was calculated based on the mass of N-rGO in each cathode. When conducted within the voltage window of 2.0 – 4.5 V and a current density of 200 mA g^{-1}, the discharge capacity of N-rGO barely reaches 500 mA h g^{-1}, while cathodes with cobalt sulfide as catalysts show much larger specific capacity at 2870 (CoS-600@NG), 3678 (CoS-1000@NG), 4163 (CoS-400@NG), and 7410 mA h g^{-1} (CoS-900@NG), respectively. Compared with pure N-rGO cathode, the presence of cobalt sulfide catalysts lead to an obvious increase in both the specific capacity and discharge potential plateau, suggesting the superior ORR activity of cobalt sulfides. Figure 4.4c compares the full discharge curve among CoS-400@NG, CoS-600@NG, CoS-900@NG, and CoS-1000@NG for the first cycle. The discharge potential of CoS-900@NG starts at 2.73 V and keeps above 2.60 V before the slowly capacity degradation at ~ 7000 mA

h g^{-1}. CoS-1000@NG possesses a similar discharge potential starts at 2.72 V but experiences a quick drop to 2.50 V when capacity reach ~ 3500 mA h g^{-1}. For CoS-600@NG and CoS-400@NG, the discharge potential both start at 2.70 V and keep flat before decade to 2.50 V at capacity of ~ 2700 and ~ 4000 mA h g^{-1} respectively. The comparison demonstrates the ORR catalytic performance in the non-aqueous Li-O_2 system among cobalt sulfides in different phases. As one of the most important criteria of catalyst, CoS-900@NG presents the advanced stability toward ORR activity than other cathode materials. During charge (Figure 4.4b), pure N-rGO cathode fails to charge stable at a potential plateau before the cut – off potential at 4.5 V, indicating an inferior OER performance compared with cobalt sulfide catalysts. CoS-900@NG and CoS-600@NG achieve 100% recycle of their discharge capacity, while CoS-1000@NG and CoS-400@NG are only able to reverse 44.8% and 88.0% of their discharge capacity at the cut – off potential of 4.5 V. The results suggest that although the full reverse of CoS-900@NG capacity at charge can be associated with the outstanding OER catalytic activity as demonstrated in CV curve, it is not the only factor that governs the charge mechanism of Li-O_2 battery. The electrical charge transport plays an important role in determining the electrochemical mechanism of charge process in Li-O_2 batteries, as the accumulation of discharge products caused by the low charge transport can severely decay the charge process. The electrochemical impedance spectroscopy (EIS) is an effective method to investigate charge transport behavior of batteries. As shown in Figure 4.4d, the EIS curve of pristine CoS-400@NG, CoS-600@NG, CoS-900@NG, and CoS-1000@NG cathodes were tested to characterize their charge transport properties under O_2 atmosphere. The impedance of CoS-900@NG is much lower than those of other cathodes, suggesting a higher conductivity and faster charge transfer of the cathode. In addition, CoS-900@NG exhibits excellent rate performance with specific capacity at 7410, 2636, and 2409 mA h g^{-1} at current densities of 200, 500 and 1000 mA g^{-1} (Figure 4.S2). Though experiences a quick drop of capacity when the current density increase from 200 to 500 mA g^{-1}, CoS-900@NG delivers stable capacity at ~ 2500 mA h g^{-1} as the current density increase to 1000 mA h g^{-1}, with 100% reverse of its

discharge capacity. The results demonstrate the electrocatalytic performance of COS-900@NG are stable at high current density towards to both ORR and OER processes.

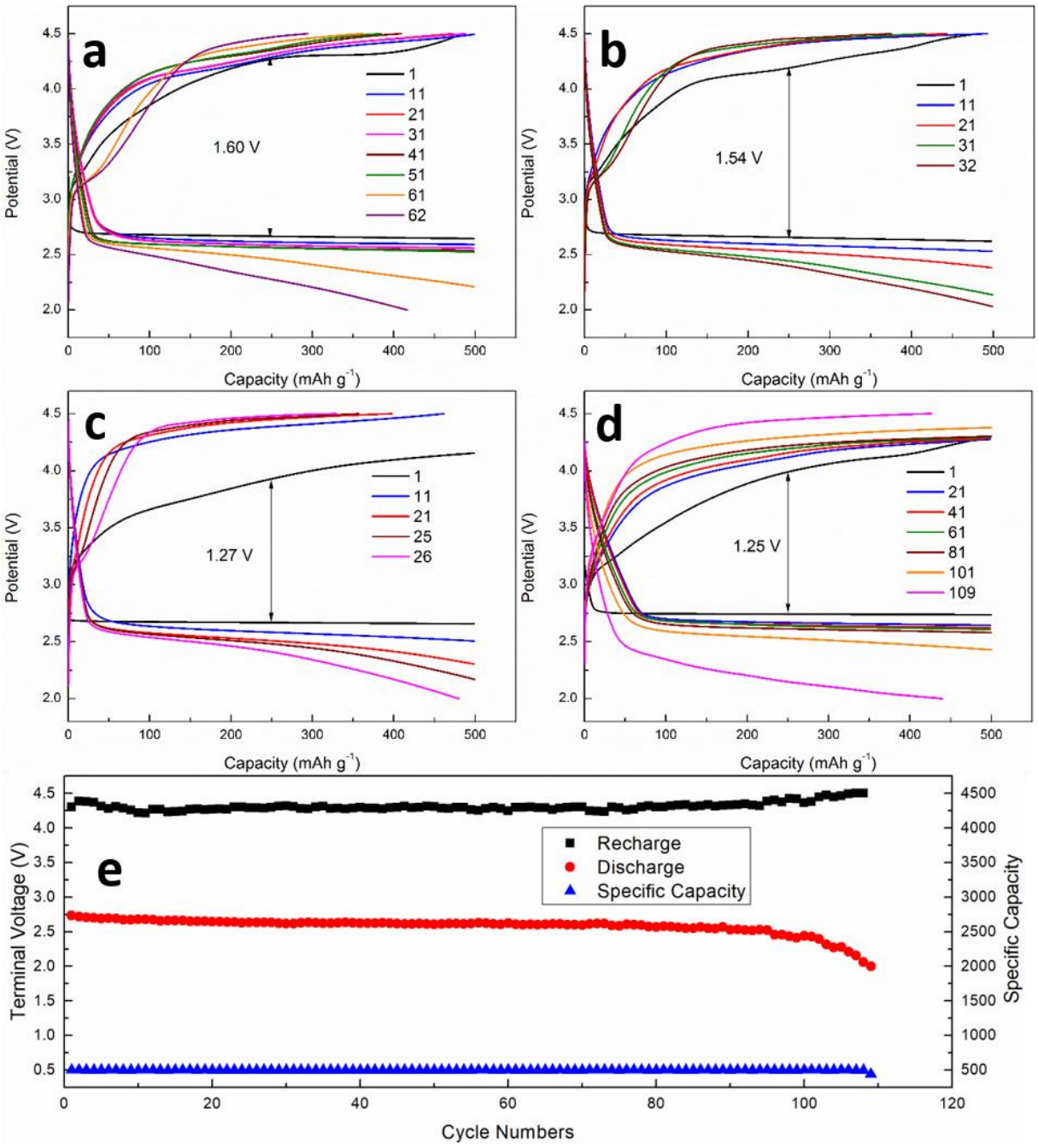

Figure 4.5. Cycling performance of the Li-O_2 batteries with (a) CoS-400@NG; (b) CoS-600@NG (c) CoS-1000@NG and (d) CoS-900@NG at 200 mA g^{-1} and a cut-off capacity of 500 mA h g^{-1}. (e) Cycling stability and terminal discharge and recharge voltages of CoS-900@NG at 200 mA g^{-1} and a cut-off capacity of 500 mA h g^{-1}.

Cycling performance of Li-O_2 batteries with different cathode materials were tested at a current density of 200 mA g^{-1} and a cut-off capacity of 500 mA h g^{-1} to investigate the stability (Figure

4.5a-d). For the initial cycle, the overpotential for each cathode material is 1.60 V for CoS-400@NG, 1.54 V for CoS-600@NG, 1.25 V for CoS-900@NG, 1.27 V for CoS-1000@NG. The comparisons between CoS-400@NG with CoS-600@NG and CoS-900@NG with CoS-1000@NG indicate the improvement of catalytic performance by introducing CoS phase to CoS_2 and Co_9S_8 respectively. However, when the batteries keep running to the 21st cycle, the overpotential grows to 1.69 V for CoS-400@NG, 1.74 V for CoS-600@NG, 1.47 V for CoS-900@NG, and 1.99 V for CoS-1000@NG. The increment of overpotential is 0.09, 0.20, 0.22, and 0.72 V respectively. The results imply that CoS-400@GN shows the best electrocatalytic stability during cycling, and CoS-600@NG presents slightly better stability than that of CoS-900@NG, while the electrocatalytic stability of CoS-1000@NG is the worst among all the cathode materials. As a combination of activity and stability of catalysts, the CoS-900@NG cathode can sustain long cycle life for 108 cycles (Figure 4.5d), while CoS-400@NG (Figure 4.5a), CoS-600@NG (Figure 4.5b) and CoS-1000@NG cathode (Figure 4.5c) can last for 61, 32, and 26 cycles respectively before failed to achieve the cut – off capacity at 500 mA h g^{-1}. In addition, the discharge terminal voltage of the battery with CoS-900@NG is plotted as shown in Figure 4.5e, it reveals the discharge terminal voltage can stay above 2.5 V for ~ 100 cycles before notable degradation observed, and remarkably, CoS-900@NG cathode can be fully recovered even after more than 100 cycles of recharge, which is a significant improvement compared with the early charge capacity decay at less than 30 cycles of batteries with CoS-400@NG, CoS-600@NG and CoS-1000@NG cathodes. Comparison of the battery performance of this dual-phase cathode CoS-900@NG and previous reported cobalt sulfide based catalysts in Li-O_2 batteries is listed in Table 4.S1. The CoS-900@NG exhibits high capacity performance and outstanding cyclic performance at higher current density.

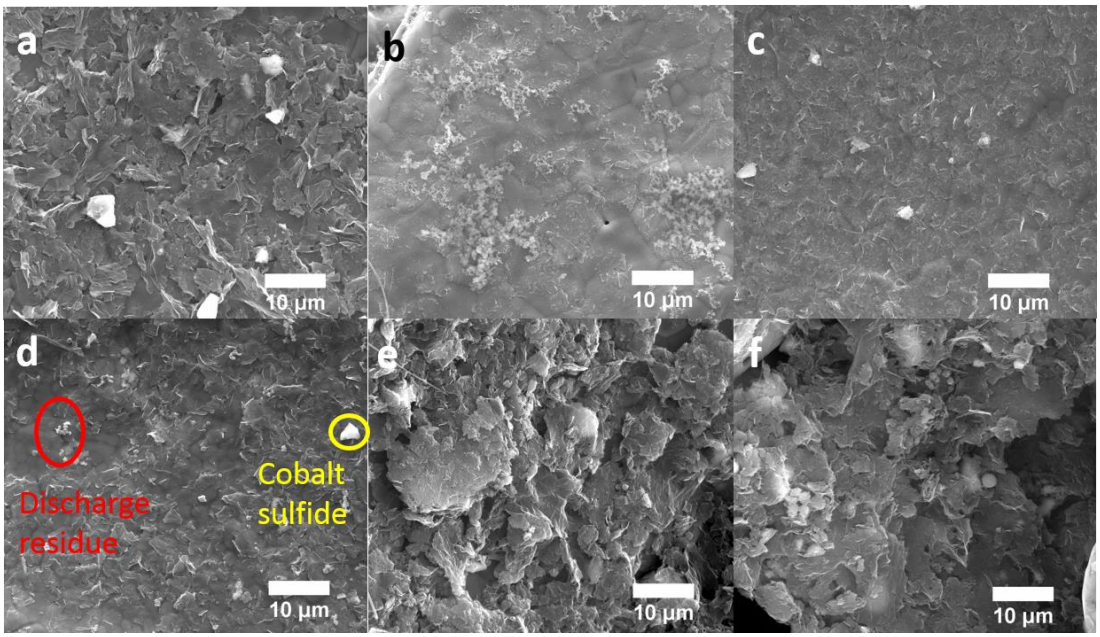

Figure 4.6. SEM images of (a) pristine CoS-900@NG; (b) crystalline Li2O2 morphology and (c) film-like Li2O2 morphology after 1st full discharge; SEM images of CoS-900@NG (d) after 1st full charge; (e) after 1st discharge and (f) recharge at a cut-off capacity of 500 mA h g-1.

To further explore the superior electrochemical performance of CoS-900@NG, the changes in the morphologies of the cathode at different discharge - charge stages were investigated by analyzing SEM images to observe the formation and decomposition of discharge products during Li-O_2 battery operation. Figure 4.6a give the morphology of pristine CoS-900@NG, the particles on the cathode are defined as cobalt sulfide crystalline. Unlike the generation of typical toroidal/ spherical Li_2O_2 crystalline reported in other literatures [43-45], both Li_2O_2 crystalline (Figure 4.6b) and Li_2O_2 film (Figure 4.6c) are observed homogeneously deposited on CoS-900@NG cathode after 1st full discharge. On discharge, the crystalline Li_2O_2 generates through the solution growth pathway by disproportionation reaction (Reaction 4.3), while the amorphous Li_2O_2 film grows through surface growth pathway by one electron transfer electrochemical process (Reaction 4.4) [4-5]. The formation of film-like Li_2O_2 can be attributed to the strong O_2 adsorption affinity of CoS-900@NG cathode. Given the fact that detected facets Co_9S_8 (440), Co_9S_8 (111), and Co_9S_8 (311) on CoS-900@NG have been proved to possess strong intrinsic O_2 adsorption ability, LiO_2 can be absorbed onto the cathode surface and reduced to film like Li_2O_2 [4, 45]. Li_2O_2 morphologies strongly relate to the performance of Li-O_2

battery through the Li_2O_2 formation and decomposition mechanism[5]. On discharge, the Li_2O_2 toroids which grow through disproportionation of the soluble intermediate LiO_2 are believed to lead high capacity because of their high Li_2O_2 production [5]. The amorphous Li_2O_2 film formed on CoS-900@NG possesses considerable higher electronic conductivity than that of crystalline Li_2O_2 [51-52], therefore, during charge, the electrochemical decomposition of Li_2O_2 can be faster and the OER polarization can be smaller when the charge transport occurred via election tunneling through the film [6-7]. Moreover, the large contact areas between cathode and film-like Li_2O_2 can create voids during the decomposition of Li_2O_2 film, and the voids then be filled by the collapse of Li_2O_2 particles till the full decomposition, which has been proven to effectively promote the OER kinetics and therefore to reduce overpotential and improve the long-term cycle-ability of the battery [8]. On the other hand, crystalline Li_2O_2 potentially hinders the charge transport due to its poor electronic conductivity, the sluggish charge transport can result in an incompletion of Li_2O_2 decomposition during charge [10]. As shown in Figure 4.6d, the Li_2O_2 film disappears after charge and CoS-900@NG is exposed with obvious discharge residue caused by the incomplete decomposition of Li_2O_2 crystalline. These insulated discharge residue can increases impedance and reduce catalytic performance in the OER process. The EIS curve shows (Figure 4.S3a) that the impedance of CoS-900@NG raises dramatically after discharge because of the formation of non-conducive discharge products and fails to recover its initial value after 1st charge due to the presence of discharge residue. This can also be observed from the cycling CV curves of CoS-900@NG cathode (Figure 4.S3b) where an obvious drop of the peak at 3.4 V occurs on the second cycle because of the incomplete oxidation of Li_2O_2, which further leads to the capacity fading of Li-O_2 system. To compare with, the morphology of CoS-900@NG after the 1st discharge and charge at a cut-off capacity of 500 mA h g^{-1} has also been studied. Compared with its original morphology, the discharge morphology of CoS-900@NG (Figure 4.6e) can be barely seen any change, which can be attributed to the very thin film-like Li_2O_2 generated at low discharge capacity. After charge (Figure 4.6f), no obvious discharge residue is observed, indicating the full decomposition of Li_2O_2 during charge.

Conclusion

Controlled-phase cobalt sulfides were synthesized via the thermal decomposition of $Co(TU)_4(NO_3)_2$ at different temperatures. Pure phase catalysts CoS-400 (CoS_2) and CoS-1000 (Co_9S_8) together with dual-phase catalysts CoS-600 (CoS and CoS_2) and CoS-900 (CoS and Co_9S_8) were physically mixed with N doped graphene as the cathode in Li-O_2 batteries. The designed CoS-900@NG cathode exhibits excellent ORR/OER catalytic activities and achieved high discharge capacity at 7410 mA h g^{-1} with 100% charge capacity recovery as well as a super long cycle life for 108 cycles in Li-O_2 system, which is superior than any reported cobalt sulfide catalyzed Li-O_2 system. The cathode morphologies after discharge and charge were investigated by SEM with the observation of both Li_2O_2 crystalline and amorphous film-like Li_2O_2, which was proved to improve the Li-O_2 battery performance in both discharge and charge processes. This work for the first time investigated the phase impact of cobalt sulfides in Li-O_2 battery, which provided a new perspective for the development of novel ORR/OER catalyst for Li-O_2 batteries.

References

1. Bruce, P. G.; Freunberger, S. A.; Hardwick, L. J.; Tarascon, J. M., Li-O-2 and Li-S batteries with high energy storage. *Nature Materials* **2012,** *11* (1), 19-29.
2. Aurbach, D.; McCloskey, B. D.; Nazar, L. F.; Bruce, P. G., Advances in understanding mechanisms underpinning lithium-air batteries. *Nature Energy* **2016,** *1*.
3. Li, L.; Shen, L.; Nie, P.; Pang, G.; Wang, J.; Li, H.; Dong, S.; Zhang, X., Porous NiCo2O4 nanotubes as a noble-metal-free effective bifunctional catalyst for rechargeable Li–O2 batteries. *Journal of Materials Chemistry A* **2015,** *3* (48), 24309-24314.
4. Lim, H. D.; Lee, B.; Bae, Y.; Park, H.; Ko, Y.; Kim, H.; Kim, J.; Kang, K., Reaction chemistry in rechargeable Li-O-2 batteries. *Chem. Soc. Rev.* **2017,** *46* (10), 2873-2888.
5. Lyu, Z.; Zhou, Y.; Dai, W.; Cui, X.; Lai, M.; Wang, L.; Huo, F.; Huang, W.; Hu, Z.; Chen, W., Recent advances in understanding of the mechanism and control of Li2O2 formation in aprotic Li–O2 batteries. *Chem. Soc. Rev.* **2017,** *46* (19), 6046-6072.

6. Wang, J.; Zhang, Y.; Guo, L.; Wang, E.; Peng, Z., Identifying Reactive Sites and Transport Limitations of Oxygen Reactions in Aprotic Lithium-O2 Batteries at the Stage of Sudden Death. *Angew. Chem. Int. Ed.* **2016,** *55* (17), 5201-5205.

7. Luntz, A. C.; Viswanathan, V.; Voss, J.; Varley, J. B.; Nørskov, J. K.; Scheffler, R.; Speidel, A., Tunneling and Polaron Charge Transport through Li2O2 in Li–O2 Batteries. *The Journal of Physical Chemistry Letters* **2013,** *4* (20), 3494-3499.

8. Zhang, Y.; Cui, Q.; Zhang, X.; McKee, W. C.; Xu, Y.; Ling, S.; Li, H.; Zhong, G.; Yang, Y.; Peng, Z., Amorphous Li2 O2 : Chemical Synthesis and Electrochemical Properties. *Angewandte Chemie (International ed. in English)* **2016,** *55* (36), 10717-10721.

9. Kushima, A.; Koido, T.; Fujiwara, Y.; Kuriyama, N.; Kusumi, N.; Li, J., Charging/Discharging Nanomorphology Asymmetry and Rate-Dependent Capacity Degradation in Li–Oxygen Battery. *Nano Lett.* **2015,** *15* (12), 8260-8265.

10. Johnson, L.; Li, C.; Liu, Z.; Chen, Y.; Freunberger, S. A.; Ashok, P. C.; Praveen, B. B.; Dholakia, K.; Tarascon, J. M.; Bruce, P. G., The role of LiO2 solubility in O2 reduction in aprotic solvents and its consequences for Li-O2 batteries. *Nat. Chem.* **2014,** *6* (12), 1091-9.

11. Lee, B.; Kim, J.; Yoon, G.; Lim, H.-D.; Choi, I.-S.; Kang, K., Theoretical Evidence for Low Charging Overpotentials of Superoxide Discharge Products in Metal–Oxygen Batteries. *Chem. Mater.* **2015,** *27* (24), 8406-8413.

12. Varley, J. B.; Viswanathan, V.; Nørskov, J. K.; Luntz, A. C., Lithium and oxygen vacancies and their role in Li2O2 charge transport in Li–O2 batteries. *Energy Environ. Sci.* **2014,** *7* (2), 720-727.

13. Girishkumar, G.; McCloskey, B.; Luntz, A. C.; Swanson, S.; Wilcke, W., Lithium−Air Battery: Promise and Challenges. *The Journal of Physical Chemistry Letters* **2010,** *1* (14), 2193-2203.

14. Lim, H.-D.; Song, H.; Kim, J.; Gwon, H.; Bae, Y.; Park, K.-Y.; Hong, J.; Kim, H.; Kim, T.; Kim, Y. H.; Lepró, X.; Ovalle-Robles, R.; Baughman, R. H.; Kang, K., Superior Rechargeability and Efficiency of Lithium–Oxygen Batteries: Hierarchical Air Electrode Architecture Combined with a Soluble Catalyst. *Angew. Chem.* **2014,** *126* (15), 4007-4012.

15. Fei, B.; Qian, B.; Yang, Z.; Wang, R.; Liu, W. C.; Mak, C. L.; Xin, J. H., Coating carbon nanotubes by spontaneous oxidative polymerization of dopamine. *Carbon* **2008,** *46* (13), 1795-1797.

16. Wang, D.-W.; Li, F.; Liu, M.; Lu, G. Q.; Cheng, H.-M., 3D Aperiodic Hierarchical Porous Graphitic Carbon Material for High-Rate Electrochemical Capacitive Energy Storage. *Angew. Chem. Int. Ed.* **2008,** *47* (2), 373-376.

17. Wang, Z. L.; Xu, D.; Xu, J. J.; Zhang, L. L.; Zhang, X. B., Graphene Oxide Gel-Derived, Free-Standing, Hierarchically Porous Carbon for High-Capacity and High-Rate Rechargeable Li-O2 Batteries. *Adv. Funct. Mater.* **2012,** *22* (17), 3699-3705.

18. Sun, B.; Huang, X.; Chen, S.; Munroe, P.; Wang, G., Porous Graphene Nanoarchitectures: An Efficient Catalyst for Low Charge-Overpotential, Long Life, and High Capacity Lithium–Oxygen Batteries. *Nano Lett.* **2014,** *14* (6), 3145-3152.

19. Kichambare, P.; Rodrigues, S.; Kumar, J., Mesoporous Nitrogen-Doped Carbon-Glass Ceramic Cathodes for Solid-State Lithium–Oxygen Batteries. *ACS Applied Materials & Interfaces* **2012,** *4* (1), 49-52.

20. Li, Y.; Wang, J.; Li, X.; Geng, D.; Banis, M. N.; Li, R.; Sun, X., Nitrogen-doped graphene nanosheets as cathode materials with excellent electrocatalytic activity for high capacity lithium-oxygen batteries. *Electrochem. Commun.* **2012,** *18*, 12-15.

21. Shu, C.; Li, B.; Zhang, B.; Su, D., Hierarchical Nitrogen-Doped Graphene/Carbon Nanotube Composite Cathode for Lithium–Oxygen Batteries. *ChemSusChem* **2015,** *8* (23), 3973-3976.

22. Wu, J.; Ma, L.; Yadav, R. M.; Yang, Y.; Zhang, X.; Vajtai, R.; Lou, J.; Ajayan, P. M., Nitrogen-Doped Graphene with Pyridinic Dominance as a Highly Active and Stable Electrocatalyst for Oxygen Reduction. *ACS Applied Materials & Interfaces* **2015,** *7* (27), 14763-14769.

23. Zhao, C.; Yu, C.; Liu, S.; Yang, J.; Fan, X.; Huang, H.; Qiu, J., 3D Porous N-Doped Graphene Frameworks Made of Interconnected Nanocages for Ultrahigh-Rate and Long-Life Li-O2Batteries. *Adv. Funct. Mater.* **2015,** *25* (44), 6913-6920.

24. Han, J.; Guo, X.; Ito, Y.; Liu, P.; Hojo, D.; Aida, T.; Hirata, A.; Fujita, T.; Adschiri, T.; Zhou, H.; Chen, M., Effect of Chemical Doping on Cathodic Performance of Bicontinuous Nanoporous Graphene for Li-O2 Batteries. *Advanced Energy Materials* **2016,** *6* (3), 1501870.

25. Qu, K.; Zheng, Y.; Dai, S.; Qiao, S. Z., Graphene oxide-polydopamine derived N, S-codoped carbon nanosheets as superior bifunctional electrocatalysts for oxygen reduction and evolution. *Nano Energy* **2016,** *19*, 373-381.

26. Liang, Y. Y.; Li, Y. G.; Wang, H. L.; Zhou, J. G.; Wang, J.; Regier, T.; Dai, H. J., Co3O4 nanocrystals on graphene as a synergistic catalyst for oxygen reduction reaction. *Nature Materials* **2011,** *10* (10), 780-786.

27. Yeo, B. S.; Bell, A. T., Enhanced Activity of Gold-Supported Cobalt Oxide for the Electrochemical Evolution of Oxygen. *J. Am. Chem. Soc.* **2011,** *133* (14), 5587-5593.

28. Chen, S.; Duan, J.; Han, W.; Qiao, S. Z., A graphene-MnO2 framework as a new generation of three-dimensional oxygen evolution promoter. *Chem. Commun.* **2014,** *50* (2), 207-209.

29. Ma, T. Y.; Dai, S.; Jaroniec, M.; Qiao, S. Z., Metal–Organic Framework Derived Hybrid Co3O4-Carbon Porous Nanowire Arrays as Reversible Oxygen Evolution Electrodes. *J. Am. Chem. Soc.* **2014,** *136* (39), 13925-13931.

30. Liu, G.; Chen, H.; Xia, L.; Wang, S.; Ding, L.-X.; Li, D.; Xiao, K.; Dai, S.; Wang, H., Hierarchical Mesoporous/Macroporous Perovskite La0.5Sr0.5CoO3–x Nanotubes: A Bifunctional Catalyst with Enhanced Activity and Cycle Stability for Rechargeable Lithium Oxygen Batteries. *ACS Applied Materials & Interfaces* **2015,** *7* (40), 22478-22486.

31. Suen, N.-T.; Hung, S.-F.; Quan, Q.; Zhang, N.; Xu, Y.-J.; Chen, H. M., Electrocatalysis for the oxygen evolution reaction: recent development and future perspectives. *Chem. Soc. Rev.* **2017,** *46* (2), 337-365.

32. Li, R.; Dai, Y.; Chen, B.; Zou, J.; Jiang, B.; Fu, H., Nitrogen-doped Co/Co9S8/partly-graphitized carbon as durable catalysts for oxygen reduction in microbial fuel cells. *J. Power Sources* **2016,** *307*, 1-10.

33. Jiang, D.; Liang, H.; Liu, Y.; Zheng, Y.; Li, C.; Yang, W.; Barrow, C. J.; Liu, J., In situ generation of CoS1.097 nanoparticles on S/N co-doped graphene/carbonized foam for mechanically tough and flexible all solid-state supercapacitors. *Journal of Materials Chemistry A* **2018,** *6* (25), 11966-11977.

34. Jin, M.; Lu, S.-Y.; Ma, L.; Gan, M.-Y.; Lei, Y.; Zhang, X.-L.; Fu, G.; Yang, P.-S.; Yan, M.-F., *Different distribution of in-situ thin carbon layer in hollow cobalt sulfide nanocages and their application for supercapacitors*. **2017**; Vol. 341, p 294-301.

35. Yang, Z. S.; Chen, C. Y.; Liu, C. W.; Chang, H. T., Electrocatalytic sulfur electrodes for CdS/CdSe quantum dot-sensitized solar cells. *Chem. Commun.* **2010,** *46* (30), 5485-5487.

36. Kung, C. W.; Chen, H. W.; Lin, C. Y.; Huang, K. C.; Vittal, R.; Ho, K. C., CoS Acicular Nanorod Arrays for the Counter Electrode of an Efficient Dye-Sensitized Solar Cell. *Acs Nano* **2012,** *6* (8), 7016-7025.

37. Jin, R.; Yang, L.; Li, G.; Chen, G., Hierarchical worm-like CoS2 composed of ultrathin nanosheets as an anode material for lithium-ion batteries. *Journal of Materials Chemistry A* **2015,** *3* (20), 10677-10680.

38. Gu, Y.; Xu, Y.; Wang, Y., Graphene-Wrapped CoS Nanoparticles for High-Capacity Lithium-Ion Storage. *Acs Applied Materials & Interfaces* **2013,** *5* (3), 801-806.

39. Mahmood, N.; Zhang, C. Z.; Jiang, J.; Liu, F.; Hou, Y. L., Multifunctional Co3S4/Graphene Composites for Lithium Ion Batteries and Oxygen Reduction Reaction. *Chemistry-a European Journal* **2013,** *19* (16), 5183-5190.

40. Wang, Q. F.; Zou, R. Q.; Xia, W.; Ma, J.; Qiu, B.; Mahmood, A.; Zhao, R.; Yang, Y. Y. C.; Xia, D. G.; Xu, Q., Facile Synthesis of Ultrasmall CoS2 Nanoparticles within Thin N-

Doped Porous Carbon Shell for High Performance Lithium-Ion Batteries. *Small* **2015,** *11* (21), 2511-2517.

41. Zhou, Y. L.; Yan, D.; Xu, H. Y.; Feng, J. K.; Jiang, X. L.; Yue, J.; Yang, J.; Qian, Y. T., Hollow nanospheres of mesoporous Co9S8 as a high-capacity and long-life anode for advanced lithium ion batteries. *Nano Energy* **2015,** *12*, 528-537.

42. Liu, J.; Wu, C.; Xiao, D. D.; Kopold, P.; Gu, L.; van Aken, P. A.; Maier, J.; Yu, Y., MOF-Derived Hollow Co9S8 Nanoparticles Embedded in Graphitic Carbon Nanocages with Superior Li-Ion Storage. *Small* **2016,** *12* (17), 2354-2364.

43. Dou, Y.; Lian, R.; Zhang, Y.; Zhao, Y.; Chen, G.; Wei, Y.; Peng, Z., Co9S8@carbon porous nanocages derived from a metal–organic framework: a highly efficient bifunctional catalyst for aprotic Li–O2 batteries. *Journal of Materials Chemistry A* **2018,** *6* (18), 8595-8603.

44. Lyu, Z.; Zhang, J.; Wang, L.; Yuan, K.; Luan, Y.; Xiao, P.; Chen, W., CoS2 nanoparticles–graphene hybrid as a cathode catalyst for aprotic Li–O2 batteries. *RSC Advances* **2016,** *6* (38), 31739-31743.

45. Lin, X.; Yuan, R.; Cai, S.; Jiang, Y.; Lei, J.; Liu, S.-G.; Wu, Q.-H.; Liao, H.-G.; Zheng, M.; Dong, Q., An Open-Structured Matrix as Oxygen Cathode with High Catalytic Activity and Large Li2O2 Accommodations for Lithium–Oxygen Batteries. *Advanced Energy Materials* **2018,** *8* (18), 1800089.

46. Sennu, P.; Christy, M.; Aravindan, V.; Lee, Y.-G.; Nahm, K. S.; Lee, Y.-S., Two-Dimensional Mesoporous Cobalt Sulfide Nanosheets as a Superior Anode for a Li-Ion Battery and a Bifunctional Electrocatalyst for the Li–O2 System. *Chem. Mater.* **2015,** *27* (16), 5726-5735.

47. Ganesan, P.; Prabu, M.; Sanetuntikul, J.; Shanmugam, S., Cobalt Sulfide Nanoparticles Grown on Nitrogen and Sulfur Codoped Graphene Oxide: An Efficient Electrocatalyst for Oxygen Reduction and Evolution Reactions. *ACS Catalysis* **2015,** *5* (6), 3625-3637.

48. Galiote, N. A.; Jeong, S.; Morais, W. G.; Passerini, S.; Huguenin, F., The Role of Ionic Liquid in Oxygen Reduction Reaction for Lithium-air Batteries. *Electrochim. Acta* **2017,** *247* (Supplement C), 610-616.

49. Zhang, J., *PEM Fuel Cell Electrocatalysts and Catalyst Layers: Fundamentals and Applications*. Springer London: **2008**.

50. Chou, N. H.; Ross, P. N.; Bell, A. T.; Tilley, T. D., Comparison of Cobalt-based Nanoparticles as Electrocatalysts for Water Oxidation. *ChemSusChem* **2011,** *4* (11), 1566-1569.

51. Tian, F.; Radin, M.; Siegel, D., *Enhanced Charge Transport in Amorphous Li2O2*. **2014**; Vol. 26.

52. Jung, H.-G.; Kim, H.-S.; Park, J.-B.; Oh, I.-H.; Hassoun, J.; Yoon, C. S.; Scrosati, B.; Sun, Y.-K., A Transmission Electron Microscopy Study of the Electrochemical Process of Lithium–Oxygen Cells. *Nano Lett.* **2012,** *12* (8), 4333-4335.

Supporting Information

Phase-Controlled Synthesis of Cobalt Sulfide as an Effective Bifunctional Catalyst for Long Cycle Life Li-O_2 Batteries

Qi Bi,† Heng Wang,† Haihui Wang,*†‡ and Sheng Dai*†§

† School of Chemical Engineering and Advanced Materials, The University of Adelaide, South Australia 5005, Australia

‡ School of Chemistry & Chemical Engineering, South China University of Technology, 381 Wushan Road, Guangzhou 510640, China

§ Department of Chemical Engineering, Brunel University London, Uxbridge, UB8 3PH, United Kingdom

Corresponding authors

*E-mail: hhwang@scut.edu.cn; sheng.dai@brunel.ac.uk

Synthesis of graphene oxide: Graphite flakes were prepared using an improved Hummer's method. 3 g natural graphite flakes were added into a mixture of concentrated H_2SO_4 and H_3PO_4 (360:40 mL), followed by the addition of 18 g $KMnO_4$. The mixture was heated and stirred at 50 °C for 12 h. After cooling down to room temperature, it was poured into 400 ml ice-water with addition of H_2O_2 (30 %, 10 mL). The mixture was then filtered over a 0.45 µm PTFE membrane and washed with 200 ml of 3 0% HCl and 1 L water to obtain graphite oxide. Exfoliation of the above prepared graphite oxide was achieved by ultrasonication of the diluted graphite oxide dispersion for 30 min, followed by freeze drying the above solution to achieve graphene oxide (GO) powder.

Synthesis of nitrogen doped graphene oxide (N-rGO): 160 mg as-prepared GO was dispersed in 80 ml MilliQ water to get a 2 mg ml^{-1} GO dispersion. To the dispersion, 125 mg polydopamine being dissolved in 10 ml water was charged. The mixture then diluted with another 130 ml Milli-Q water and sonicated for 5 min before 25 ml PBS buffer (0.4 M, pH = 8.5) was added. The mixture was continuously stirred at room temperature for 24 h to get the N-GO dispersion. After washed for three times with Milli-Q water, the N-GO dispersion was frozen dry. The N-rGO was prepared through the carbonization of free-dried N-GO in a temperature programmable tube furnace under N_2 atmosphere at 400 °C for 2 h with a heating rate of 1 °C min^{-1}, then followed by further treatment at 900 °C for 3 h with a heating rate of 5 °C min^{-1}.

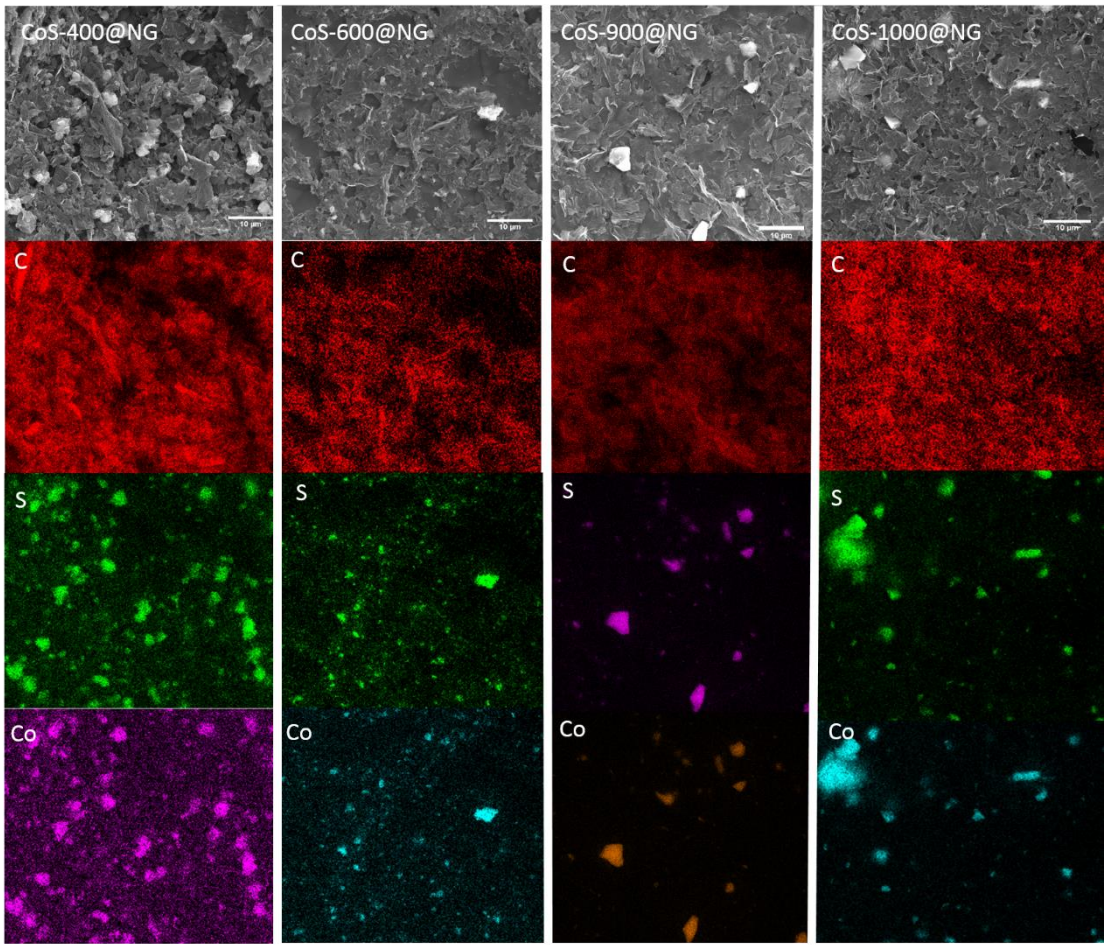

Figure 4.S1. SEM images and corresponding EDX mappings of CoS-400@NG, CoS-600@NG, CoS-900@NG, and CoS-1000@NG.

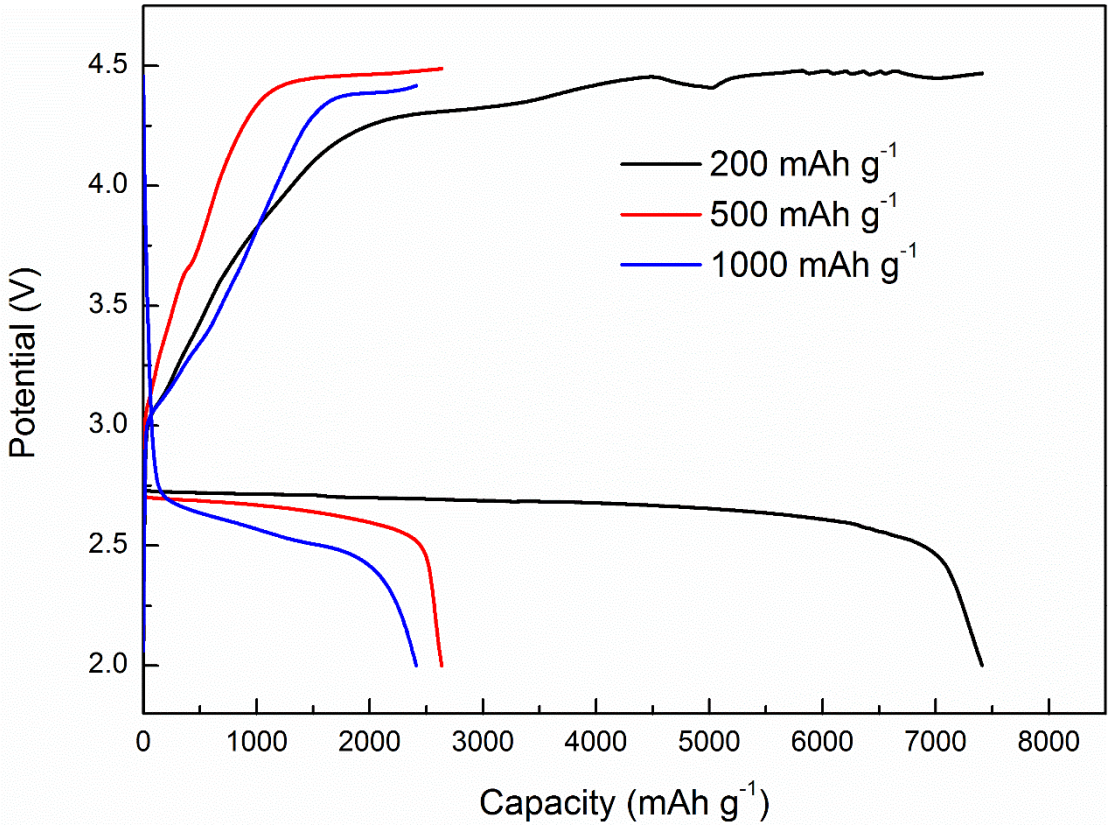

Figure 4.S2. The Galvanostatic discharge/charge curves of CoS-900@NG at various current densities.

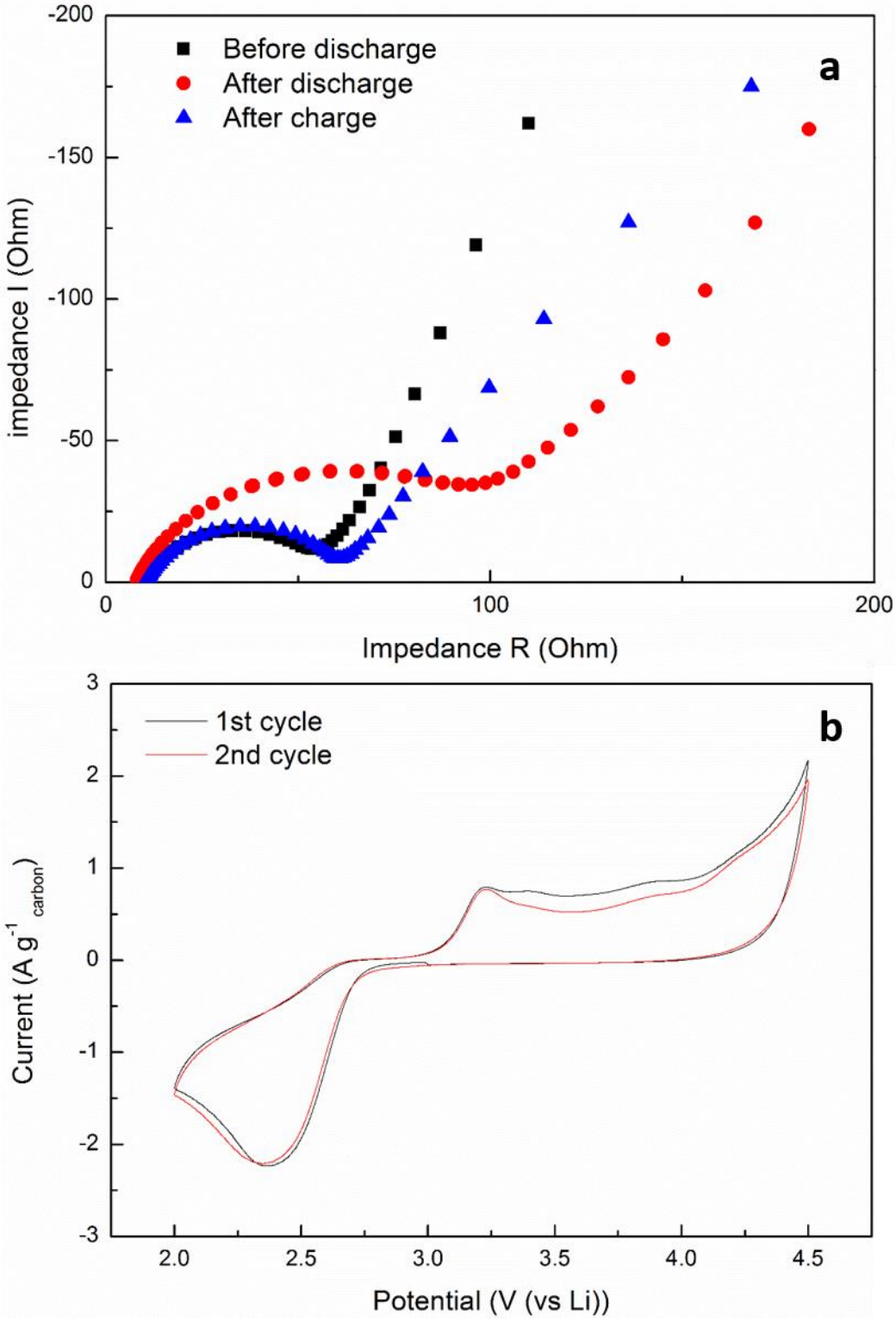

Figure 4.S3. (a) EIS spectra CoS-900@NG electrode before/after first discharge and after first charge; (b) Comparison on the CV curves of CoS-900@NG electrode (first and second cycle operation) at a scanning rate of 1 mV s^{-1}.

Table 4.S1. Comparison on the Li-O_2 battery performance with cobalt sulfide based cathodes

Cathode Materials	Electrolyte	Current Density (mA g^{-1})	Maximum Capacity (mA h g^{-1})	Cut – off Capacity (mA h g^{-1})	Cyclic Performance	Reference
CoS-900@NG	LiTFSI/TEGDME	200	7410	500	108 cycles at 200 mA g^{-1}	This work
Co_9S_8-PCF	$LiClO_4$/DMSO	200	4767	500	105 cycles at 100 mA g^{-1}	S1
Co_9S_8@CPNs	LiTFSI/TEGDME	200	4773	500	110 cycles at 100 mA g^{-1}	S2
CoS_2/RGO	$LiClO_4$/DMSO	100	~ 2500	500	18 cycles at 100 mA g^{-1}	S3
Co_3S_4–NS	LiTFSI/TEGDME	200	6990	500	25 cycles at 100 mA g^{-1}	S4

S1. Lin, X.; Yuan, R.; Cai, S.; Jiang, Y.; Lei, J.; Liu, S.-G.; Wu, Q.-H.; Liao, H.-G.; Zheng, M.; Dong, Q., An Open-Structured Matrix as Oxygen Cathode with High Catalytic Activity and Large Li2O2 Accommodations for Lithium–Oxygen Batteries. *Advanced Energy Materials* **2018,** *8* (18), 1800089.S2. Dou, Y.; Lian, R.; Zhang, Y.; Zhao, Y.; Chen, G.; Wei, Y.; Peng, Z., Co9S8@carbon porous nanocages derived from a metal–organic framework: a highly efficient bifunctional catalyst for aprotic Li–O2 batteries. *Journal of Materials Chemistry A* **2018,** *6* (18), 8595-8603.

S3. Lyu, Z.; Zhang, J.; Wang, L.; Yuan, K.; Luan, Y.; Xiao, P.; Chen, W., CoS2 nanoparticles–graphene hybrid as a cathode catalyst for aprotic Li–O2 batteries. *RSC Advances* **2016,** *6* (38), 31739-31743.

S4. Sennu, P.; Christy, M.; Aravindan, V.; Lee, Y.-G.; Nahm, K. S.; Lee, Y.-S., Two-Dimensional Mesoporous Cobalt Sulfide Nanosheets as a Superior Anode for a Li-Ion Battery and a Bifunctional Electrocatalyst for the Li–O2 System. *Chem. Mater.* **2015,** *27* (16), 5726-5735.

Chapter 5 Development of Co_9S_8 Hybridised N, S-GO Nanosheets as High-performance Cathodes for Li-O_2 Batteries

5.1 Introduction and Significance

Co_9S_8 is an effective electrocatalyst for non-aqueous Li-O_2 batteries, but their low conductivity and large volume variation during lithiation and delithiation processes hinder the improvement of battery performance. N, S co-doped graphene is highly conductive and possesses excellent activity towards oxygen reduction reaction (ORR) and oxygen evolution reaction (OER), which can act as substrate to immobilize Co_9S_8 nanoparticles. In this work, we explore the synergistic effect between Co_9S_8 and N, S co-doped graphene through the investigation of a series of nanocomposites of Co_9S_8 and N, S co-doped graphene. The highlights of this work include:

(a) We synthesized a series of novel nanocomposites of Co_9S_8 nanoparticles and N, S co-doped graphene through 2 different approaches to distinguish the crystallinity of Co_9S_8 nanoparticles.

(b) The synergistic effect between Co_9S_8 and N, S co-doped graphene was found to be regulated by both of Co_9S_8 crystallinity and the amounts of Co_9S_8 spread on N, S co-doped graphene nanosheets.

(c) The large surface areas and pore volumes provided by the anchoring of Co_9S_8 nanoparticles attribute to the excellent battery performance.

5.2 Development of Co_9S_8 Hybridised N, S-GO Nanosheets as High-performance Cathodes for Li-O_2 Batteries

This section is included as an un-submitted manuscript by Qi Bi, Heng Wang, Haihui Wang and Sheng Dai.

Statement of Authorship

Title of Paper	Development of Co9S8 hybridised N, S-GO nanosheets as high performance cathodes for Li-O2 batteries
Publication Status	☐ Published ☐ Accepted for Publication ☐ Submitted for Publication ☑ Unpublished and Unsubmitted work written in manuscript style
Publication Details	To be submitted.

Principal Author

Name of Principal Author (Candidate)	Qi Bi		
Contribution to the Paper	Designed research plan; performed experiments, material characterizations, and battery performance evaluations; analysed data; wrote and edited manuscript.		
Overall percentage (%)	85%		
Certification:	This paper reports on original research I conducted during the period of my Higher Degree by Research candidature and is not subject to any obligations or contractual agreements with a third party that would constrain its inclusion in this thesis. I am the primary author of this paper.		
Signature		Date	15/10/2019

Co-Author Contributions

By signing the Statement of Authorship, each author certifies that:

i. the candidate's stated contribution to the publication is accurate (as detailed above);

ii. permission is granted for the candidate in include the publication in the thesis; and

iii. the sum of all co-author contributions is equal to 100% less the candidate's stated contribution.

Name of Co-Author	Heng Wang		
Contribution to the Paper	Discussed the research plan.		
Signature		Date	15/10/2019

Name of Co-Author	Haihui Wang		
Contribution to the Paper	Co-supervised the research.		
Signature		Date	18/10/2019

Name of Co-Author	Sheng Dai		
Contribution to the Paper	Supervised the research and revised the manuscript.		
Signature		Date	15/10/2019

Please cut and paste additional co-author panels here as required.

Development of Co_9S_8 Hybridised N, S-GO Nanosheets as High-Performance Cathodes for Li-O_2 Batteries

Qi Bi, Heng Wang, Haihui Wang, and Sheng Dai**

Q. Bi, H. Wang, Prof. H. Wang, Prof. S. Dai
School of Chemical Engineering
The University of Adelaide
Adelaide SA 5005 Australia

Prof. H. Wang
School of Chemistry & Chemical Engineering
South China University of Technology
Guangzhou 510640 China

Prof. S. Dai
Department of Chemical Engineering
Brunel University London
Uxbridge UB8 3PH United Kingdom

*Corresponding author

Email: hhwang@scut.edu.cn

s.dai@adelaide.edu.au

Abstract

Due to its high theoretical energy density, non-aqueous lithium-oxygen (Li-O_2) battery has been considered to possess great potential as next generation energy storage system to resolve global energy shortage problems. Efficient cathode catalysts towards both electrochemical oxygen reduction and evolution reactions (ORR and OER) are the key challenges for practical implementation of Li-O_2 batteries associated with high discharge capacity and long cycle life. In this study, Co_9S_8 nanoparticles were anchored to N, S co-doped graphene to form leaves-like Co_9S_8/N, S-GO composites through hydrothermal treatment. The composites were further optimized by adjusting cobalt sulfide precursor amounts to achieve an improved battery performance due to its excellent O_2 adsorption, large Li_2O_2 storage space, and good Li_2O_2/cathode interface to accelerate oxygen redox kinetics. As a result, the Li-O_2 battery with Co_9S_8/N, S-GO composite can achieve a 100 % recoverable high discharge capacity at 4884 mA h g^{-1} and a stable cycle life.

Keywords: cobalt sulfide, graphene, composites, lithium oxygen batteries, ORR/OER, cycle life.

Introduction

As one of the most attractive next generation energy storage systems, it is urging to improve the electrochemical performance of Li-O_2 batteries in both energy efficiency and cycle stability to achieve practical implementation. The electrochemical performance of Li-O_2 batteries is largely influenced by the efficiency of oxygen reduction reaction (ORR) and oxygen evolution reaction (OER) associated with various factors including surface structure and heteroatom doping of the electrochemical catalysts. Though these factors are interrelated and interplayed, the catalyst structure mainly limits the O_2 diffusion and the storage of discharge products on oxygen electrode, while the heteroatom doping determines the oxygen redox kinetics associated with ORR/OER reactions [1]. Therefore, it is highly desirable to explore highly effective cathode catalysts towards both ORR and OER with all the above factors well compromised to enhance overall electrocatalytic performance of Li-O_2 batteries.

Recently, transition-metal sulfides have aroused great interests as they are widely considered as electrochemically active for ORR and OER. Particularly, cobalt sulfides with various stoichiometric compositions including CoS, CoS_2, Co_3S_4, and Co_9S_8 have been identified as effective ORR and OER catalysts for fuel cells, supercapacitors, solar cells, and lithium ion batteries [2-7]. Their low costs, high chemical kinetic stability and outstanding electrocatalytic performance make them to be promising in lithium storage among different non-precious and transition metal chalcogenide catalysts [8]. Dong and co-workers reported an open – structured Co_9S_8 matrix with sisal morphology as the oxygen cathode for Li-O_2 batteries and successfully improved the specific capacity and round-trip efficiency to prove the great electrochemical catalytic activity of Co_9S_8 in Li-O_2 batteries[1]. However, without the complex open structure, the electrochemical catalytic activity of Co_9S_8 particles is usually hindered by its large volume variation during the lithiation and delithiation processes [8]. Along with the low electrical conductivity as well as the limit surface areas caused by aggregation, the application of Co_9S_8 particles is seriously restricted by unsatisfactory catalytic durability [9-10]. To solve these problems, carbon materials (including graphene, carbon nanosheet, and carbon nanotube) have

been considered to combine with Co_9S_8 in the form of cobalt sulfide/carbon composites to increase structural stability, improve electrical conductivity as well as maximize cathodic surface areas. Among them, graphene exhibited great advantages by offering high capability for heteroatom doping to tailor material properties and improve catalytic performance. It has been proved that N-doped graphene improves ORR activity and S-doped graphene facilitates OER activity in Li-O_2 batteries [11-13]. Composites contain Co_9S_8 and heteroatom doped graphene have been proved to demonstrate advanced electrocatalytic performance towards both ORR and OER in alkaline solution [14], exhibited excellent ORR catalytic performance in microbial fuel cell [5], as well as performed as efficient anode material for sodium-ion batteries [6]. Shanmugam and co-workers proposed a temperature controlled method to prepare composites of cobalt sulfides in different phases (CoS_2 and Co_9S_8) anchored onto nitrogen and sulfur co-doped graphene oxide, which exhibited great ORR/OER catalytic potential in alkaline solution [15]. However, the electrocatalytic performance of catalytic materials varies from different electrochemical systems. To the best of our knowledge, most ORR and OER electrochemical tests of Co_9S_8/graphene composites were evaluated in alkaline electrochemical systems and has not been tested in non-aqueous Li-O_2 system. To explore the possibility of these composites as catalytic oxygen cathode in Li-O_2 system can provide a hint to apply Co_9S_8/graphene composites in neutral electrolytes for future researchers.

Herein, the composites of nanostructured Co_9S_8 on N, S co-doped graphene oxide (CNSG composites) were synthesized using two different methods with a variety of Co_9S_8 loadings. These obtained composites were applied as novel cathode materials to conduct electrochemical tests for Li-O_2 batteries to elucidate the best composites presented outstanding ORR and OER activity as well as excellent stability for high capacity and cycling stable Li-O_2 batteries.

Experiment Section

Materials: Cobalt nitrate ($Co(NO_3)_2 \cdot 6H_2O$), thiourea, graphite flake (100 mesh), potassium permanganate ($KMnO_4$), phosphoric acid (H_3PO_4 85%), polydopamine, h-butanol and N-

methyl-2-pyrrolidone (NMP) were purchased from Sigma-Aldrich. Sulfuric acid (H_2SO_4, 98%), hydrogen peroxide (H_2O_2, 30%), and polyvinylidene fluoride (PVDF) were supplied by Chem-Supply. Glass fiber membrane (Grade GF/F) was from Whatman. Lithium foil was supplied by China Energy Lithium Co., Ltd. 1 M lithium bis(trifluoromethanesulfonyl)imide (LiTFSI) intetraethylene glycol dimethyl ether (TEGDME) was from Suzhou Qianmin Chemical Reagent Co., Ltd. Ultra-high purity (99.999%) O_2 was acquired from Coregas, Australia.

Synthesis of CNSG composites: Graphene oxide (GO) was synthesized from natural graphite flakes by an improved Hummer's method. 160 mg as-prepared GO was dispersed in 80 ml Milli-Q water to get a 2 mg ml^{-1} GO dispersion. To the dispersion, 125 mg polydopamine being dissolved in 10 ml water was charged. The mixture then diluted with another 130 ml Milli-Q water and sonicated for 5 min before 25 ml phosphate-buffered saline (PBS) (0.4 M, pH = 8.5) was added. The mixture was continuously stirred at room temperature for 24 h before 170 mg cobalt thiourea complex was added to the mixture. The mixture was then stirred for 15 min and ultrasonicate for 30 min. Then two approaches were applied separately: (1) for hydrothermal treated CNSG composites (CNSG-HT2), 50 ml mixture was transferred to a 100 ml Teflon-lined autoclave and heated at 120 °C for 12 h. Keep other procedure unchanged, the loading of cobalt thiourea complex for CNSG-HT1 and CNSG-HT3 are 85 mg and 340 mg, respectively. (2) For non-hydrothermal treated composite (CNSG-NHT), the mixture was stirred at room temperature for 12 h. After the above approaches, the precipitate was collected by centrifugation, washed with deionized water for three times, and freeze-dried. The collected particles were further calcined in a temperature programmable tube furnace under N_2 atmosphere at 400 °C for 2 h with a heating rate of 1 °C min^{-1}, and then 900 °C for 3 h with a heating rate of 5 °C min^{-1}.

Synthesis of nitrogen and sulfide co-doped graphene oxide (NSG). 160 mg as-prepared GO was dispersed in 80 ml Milli-Q water to get a 2 mg ml^{-1} GO dispersion. To this dispersion, 125 mg polydopamine being dissolved in 10 ml water was charged. The mixture then diluted with another 130 ml Milli-Q water and sonicated for 5 min before 25 ml PBS buffer (0.4 M, pH =

8.5) was added. The mixture was continuously stirred at room temperature for 24 h. After that, 125 mg 2-mercaptoethanol was added and stirred continually for another 12 h. The NSGO was collected by centrifugation and washed for three times with Milli-Q water and then frozen dried. The NSG was prepared through the carbonization of NSGO in a temperature programmable tube furnace under N_2 atmosphere at 400 °C for 2 h with a heating rate of 1 °C min^{-1}, which was followed by a further treatment at 900 °C for 3 h with a heating rate of 5 °C min^{-1}.

Materials Characterization: Field emission scanning electron microscope (FESEM) images and mappings were obtained on a FEI Quanta 450. Transmission electron microscopy (TEM) images were acquired on a Tecnai G2 Spirit. X-ray diffraction (XRD) patterns were obtained on a Rigaku Miniflex 600 instrument using a Cu Kα radiation source. X-ray photoelectron spectroscopy (XPS) was conducted on a Thermo Fisher Scientific K-Alpha+ Spectrometer using a monochromatic Al Kα radiation operating at 12 kV.

Li-O_2 battery measurements: The oxygen electrodes were fabricated by coating the homogeneous slurry containing CNSG composites and polyvinylidene fluoride (PVDF) (weight ratio 9:1) in N-methyl-2-pyrrolidone (NMP) onto a Ni foam and dried at 80 °C overnight. The typical loading of the oxygen electrode is about 0.5 mg cm^{-2}. The Li-O_2 batteries were assembled with 2032-type coin cells in an Ar filled glove box with a water and oxygen level less than 0.5 ppm. The Li-O_2 cells were established using a Li metal foil as the counter electrode and the anode, a glass fiber membrane separator, the as-prepared oxygen cathode, and 1 M LiTFSI in tetra (ethylene) glycol dimethyl ether (TEGDME) as electrolyte. All measurements were conducted at 1 atm dry oxygen atmosphere. Galvanostatic discharge/recharge was tested on a Neware battery testing system within a voltage window of 2.0 – 4.5 V (Li/Li^+) after resting for 10 h at room temperature. Cyclic voltammetry (CV) tests were measured at a rate of 0.1 mV s^{-1} within the potential range of 2.0 to 4.5 V (Li/Li^+) by a CHI600 electrochemical workstation. Electrochemical impedance spectroscopy (EIS) were performed by a Zahner IM6 Electrochemical workstation in the frequency range of 0.1 Hz to 100 kHz.

Results and discussion

The synthesis of Co_9S_8/N, S-GO composite (CNSG) used polydopamine as N source, cobalt thiourea complex ($Co(TU)_4(NO_3)_2$) as Co_9S_8 precursor and S source. The anchor process of Co_9S_8 onto graphene oxide nanosheets followed two different approaches, hydrothermal treatment and non-hydrothermal treatment. During hydrothermal process, mixtures contain GO, polydopamine and various amount of cobalt thiourea complex were reacted in a Teflon-lined autoclave for 12 h. For non-hydrothermal treatment, the mixture was stirred for 12 h at room temperature.

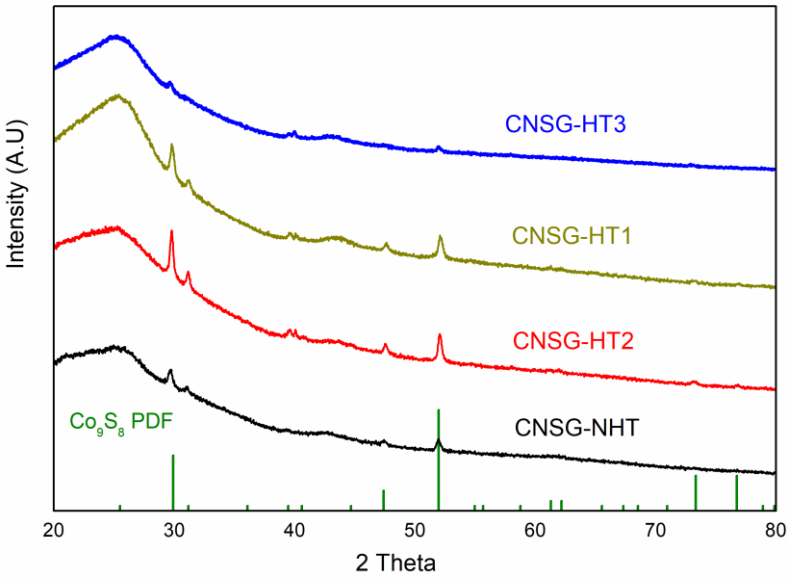

Figure 5.1. XRD patterns of CNSG-NHT, CNSG-HT1, CNSG-HT2 and CNSG-HT3.

Figure 5.1 shows the XRD pattern of various Co_9S_8/N, S-GO composites (CNSG) synthesized without hydrothermal process (CNSG-NHT) compared with hydrothermal treated CNSG composites (CNSG-HT). The CNSG-HT with a $Co(TU)_4(NO_3)_2$ and GO feed ratio of 1:2, 1:1, and 2:1 (w/w) were marked as CNSG-HT1, CNSG-HT2, and CNSG-HT3. The $Co(TU)_4(NO_3)_2$ and GO feed ratio of CNSG-NHT is 1:1. Diffraction peaks at 29.8, 31.2, 39.5, 47.6 and 51.2 were observed on all XRD patterns of CNSG-HT1, CNSG-HT2, CNSG-HT3, and CNSG-NHT, which correspond to the (311), (222), (331), (511) and (440) lattice planes of Co_9S_8 (JCPDS, card No. 02-1459). The XRD results demonstrate the successful synthesis of Co_9S_8 in all CNSG

composites. Compared with CNSG-NHT, diffraction peaks of CNSG-HT2 is much sharper and clearer, the obvious differences at 2-theta of 39.5 indicate a better crystallinity of Co_9S_8 on CNSG-HT2. The weak XRD diffraction peaks of CNSG-HT3 indicate a lower crystallinity of Co_9S_8.

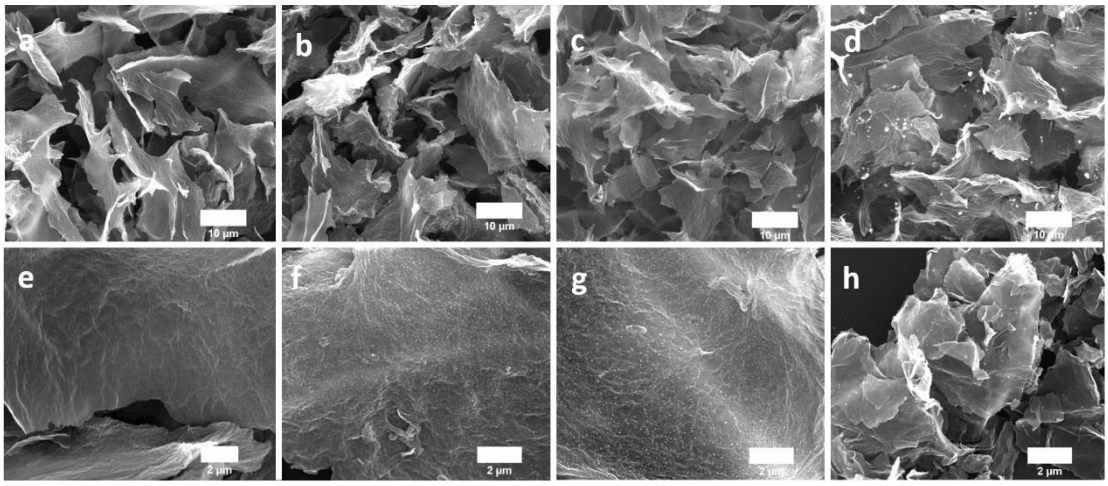

Figure 5.2. SEM morphologies of CNSG composites at different magnification. SEM images of (a, e) CNSG-HT1; (b, f) CNSG-HT2; (c, g) CNSG-HT3; (d, h) CNSG-NHT.

The morphologies of as-prepared samples are shown in Figure 5.2. All samples present leaves-like nanosheets structure with identical size despite the method of synthesis. However, the nanosheets of CNSG-NHT show obvious aggregation due to different synthesis approach. Co_9S_8 particles up to 1 µm can be clearly observed on CNSG-NHT, and nanoparticles sized up to 100 nm are found spreading on N, S-GO nanosheets homogeneously and densely for those hydrothermal treated samples (Figure 5.2f-h). For CNSG-NHT, the density of particles on N, S-GO sheet is obviously lower than that of CNSG-HT2. The results indicate that hydrothermal treatment helps to decrease the size of Co_9S_8 nanoparticles and facilitates the dispersion of Co_9S_8 to form homogeneously Co_9S_8/N-GO composite. Among CNSG-HT composites, the density of Co_9S_8 nanoparticles can be observed slightly increasing as the increase amounts of Co_9S_8 precursor. To further characterize the composition of Co_9S_8/N, S-GO composites, energy dispersive X-ray (EDX) mapping for CNSG-HT2 composite have been performed as shown in Figure 5.S1. Elemental mapping of C, N, Co, and S matches the SEM image well, implying a

homogeneous distribution of C, N, Co, and S throughout the CNSG-HT2.

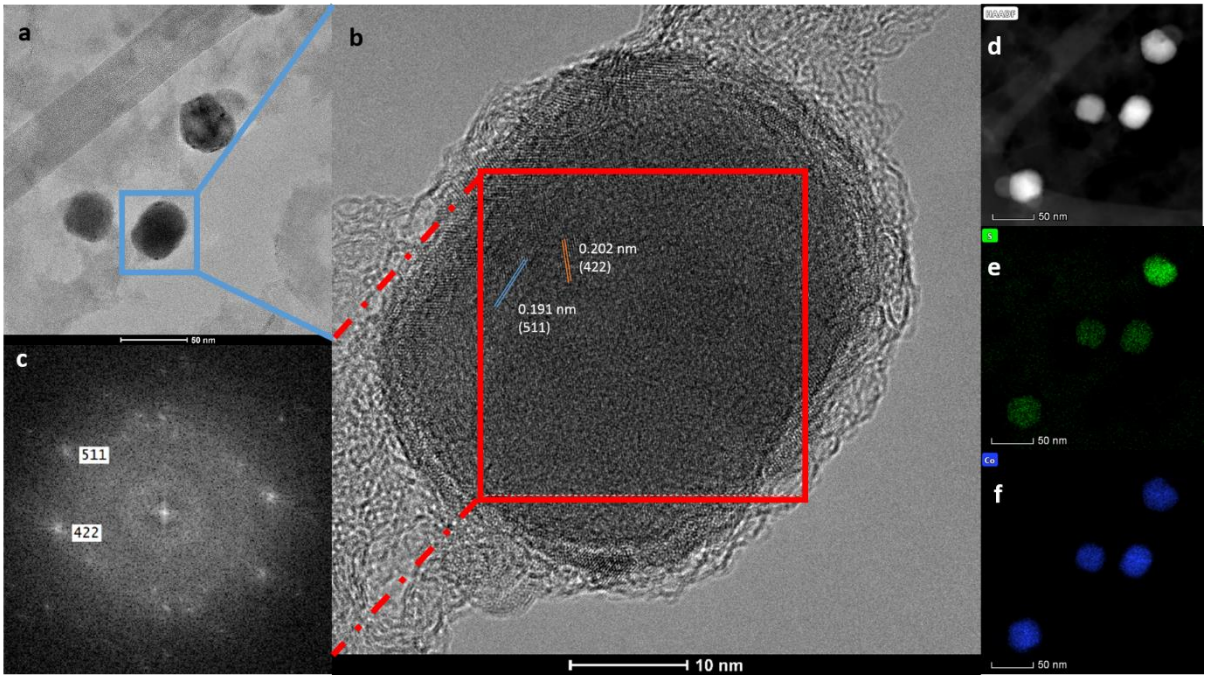

Figure 5.3. (a) TEM image of CNSG-HT2; (b) HRTEM image of the Co_9S_8 nanoparticle in CNSG-HT2; (c) Fast Fourier transform (FFT) pattern of selected area in (b); High angle annular dark field scanning TEM (HAADF-STEM) image of (d) Co_9S_8 nanoparticles, (e) S, and (f) Co on CNSG-HT2.

High resolution transmission electron microscopy (HRTEM) and the Fast Fourier transform (FFT) were further used to investigate the presence of cobalt sulfide in CNSG-HT composites. Figure 5.3a shows Co_9S_8 particle size is around 40 – 50 nm in CNSG-HT2. From the HRTEM image of Figure 5.3b, the irregular diffraction pattern of graphene can be seen in the fringe of the Co_9S_8 particles. The lattice planes with a d-spacing of 0.202 and 0.191 nm can be indexed to the Co_9S_8 (422) and (511) crystal planes. FFT pattern (Figure 5.3c) corresponds to the (422) and (511) planes of Co_9S_8 nanocrystal in selecting areas. In addition, the high angle annular dark field scanning TEM (HAADF-STEM) images demonstrate the uniform distribution and consistency of Co and S in the cobalt sulfide nanoparticle (Figure 5.3d-f). Similar to CNSG-HT2, HRTEM and FFT were also performed to exam the structures of CNSG-HT1 and CNSG-HT3 as shown in Figure 5.S2. Anchored on graphene sheets, particles in both CNSG-HT1 and CNSG-HT3 can be indexed as Co_9S_8. Particularly, the lattice planes with a d- spacing of 0.287

nm are indexed to (222) crystal planes of Co_9S_8 in CNSG-HT3, and HRTEM image of CNSG-HT1 shows d- spacing of 0.228 and 0.168 nm which are corresponding to Co_9S_8 (331) and (531) crystal planes respectively. The FFT images of both samples are consistence with the HRTEM images to further confirmed the existence of Co_9S_8 phase on CNSG-HTs.

X-ray photoelectron spectroscopy (XPS) measurements were also conducted to probe the chemical components and Co, S bonding configurations of the as-prepared composites. As shown in Figure 5.4a, the XPS element survey clearly suggests the presence of Co, S, C, N and O in CNSG-HT2. The high-resolution N 1s XPS spectrum (Figure 5.4b) reveals that nitrogen atoms in CNSG-HT2 present in the forms of graphitic (c. a. 401.2 eV), pyridinic (c.a 398.4 eV) and oxidic (c.a. 403.2 eV) nitrogen types, indicating the successfully doping of N on CNSG-HT2. The spectrum of Co 2p (Figure 5.4c) for the sample CNSG-HT2 has two group of peaks, Co $2p_{3/2}$ at 780.0 eV and Co $2p_{1/2}$ peaks at 795.0 eV [16]. These peaks are deconvoluted into six components, the peaks at 778.6, 781.4, 793.6 and 797.4 eV are assigned to Co^{3+} $2p_{3/2}$, Co^{2+} $2p_{3/2}$, Co $^{3+}$ $2p_{1/2,}$ and Co^{2+} $2p_{1/2}$ respectively, suggesting the coexistence of both Co^{3+} and Co^{2+} [17]. The presence of the Co^{3+} $2p_{3/2}$ and Co $^{3+}$ $2p_{1/2}$ confirmed Co – S bonds in Co_9S_8 [18], while Co^{2+} $2p_{1/2}$ and Co^{2+} $2p_{3/2}$ can be aligned to Co-OH bond, due to the strong affinity between cobalt ions and atmospheric oxygen and graphene, which implies the interaction between Co_9S_8 and graphene [19-20]. The shake-up satellite peaks at 786.5 and 802.8 eV are fingerprints indication of Co^{3+} cations [21]. In the S 2p spectrum (Figure 5.4d), the first peak locates at 162.2 eV is due to the spin-orbit coupling of Co-S, while the peaks at 163.8 and 164.9 eV are attributed to $2p_{3/2}$ and $2p_{1/2}$ caused by the existence of -C- S- C bonds, indicating the successful doping of sulfur on CNSG-HT2 surface and the interaction between Co_9S_8 and graphene [22], which is consistent with the EDS mapping results. For CNSG-HT1 and CNSG-HT3 composites, the same conclusion can be achieved according to the XPS spectra as shown in Figure 5.S3. The strongly coupled Co_9S_8 on CNSG surface for these samples can facilitate electrocatalytic activity towards ORR and OER [15].

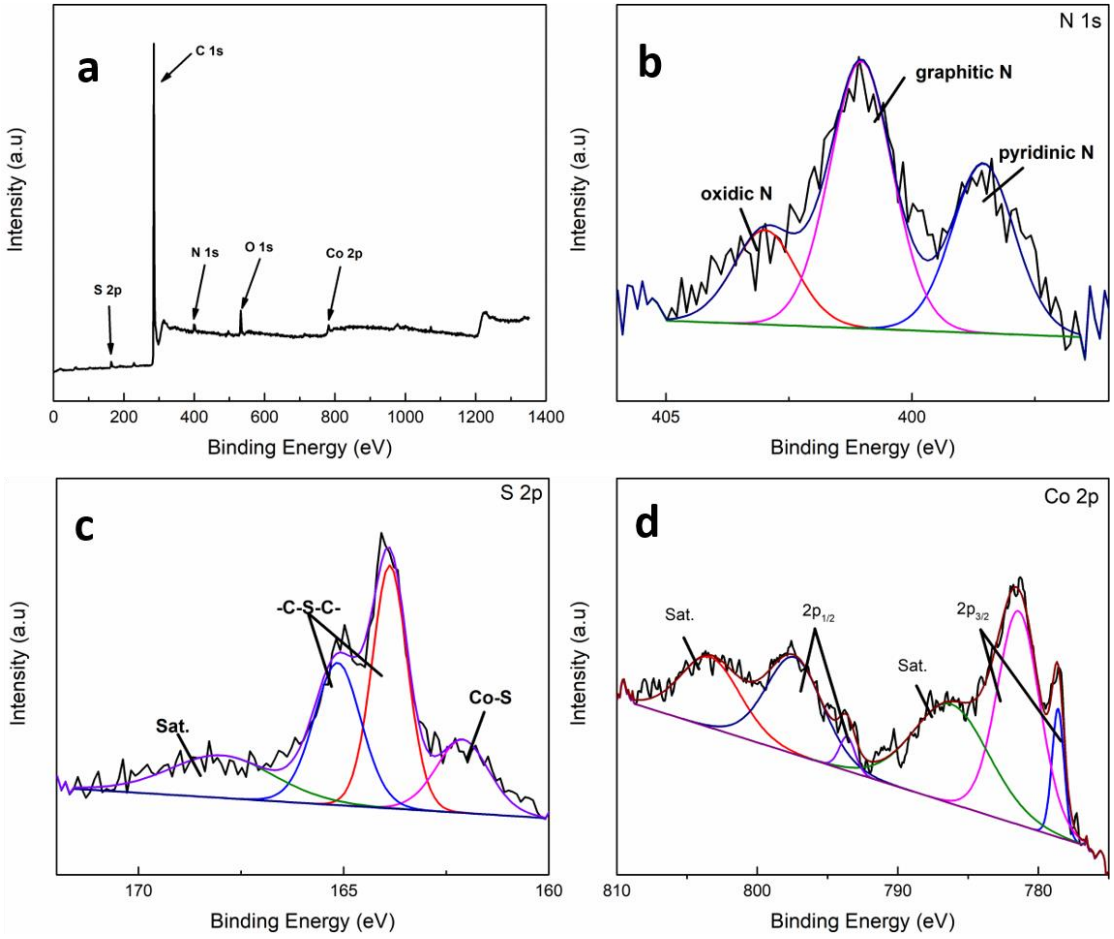

Figure 5.4. (a) XPS survey of CNSG-HT2, and high resolution XPS spectra of (b) N 1s, (c) S 2p, and (d) Co 2p of CNSG-HT2.

The structural characteristics of composites were further evaluated by nitrogen adsorption–desorption isotherm measurements (Figure 5.5). The isotherms for all materials prepared via the hydrothermal method (CNSG-HT) exhibit type IV characteristics that indicates various distribution of porous structures including both micro and meso-pores [23-24]. The steep rise at low relative pressure ($P/P_0 < 0.001$) reflects the presence of small pores or microporous structure [25]. For the CNSG-NHT composite, the adsorption isotherm shows type V characteristics that suggests the presence of mesoporous [26]. In addition, H2 hysteresis loops in adsorption-desorption isotherms for CNSG-HT2 and CNSG-HT3 are often associated to the disordered pore shape or size and bottleneck constrictions. H3 hysteresis loops are seen on isotherms for CNSG-HT1 and CNSG-NHT composites, suggesting the presence of slit-shaped pores [26]. Brunauer-Emmett-Teller (BET) method was used to calculate the surface areas and pore volumes for CNSG-HT3 (493 $m^2 g^{-1}$, 0.43 $cm^3 g^{-1}$), CNSG-HT2(439 $m^2 g^{-1}$, 0.40 $cm^3 g^{-1}$),

CNSG-HT1(34 m^2 g^{-1}, 0.09 cm^3 g^{-1}) and CNSG-NHT (38 m^2 g^{-1}, 0.08 cm^3 g^{-1}), which are significantly higher than previous reported cobalt sulphide/GO composites [15]. The different pores and surface areas in these samples can be attributed to the variance of synthesis methods and loading amount of Co_9S_8 precursors. Specifically, the mesoporous structure can be introduced by the doped Co_9S_8 nanoparticles on CNSG sheets. As a result, an increase of loading amount of Co_9S_8 precursor grows the pore volume as well as the surface area of Co_9S_8/N, S-GO composites. Meanwhile, as discussed above, hydrothermal method helps to reduce the size of Co_9S_8 as well as to facilitate doping process, accordingly, more mesoporous structure can be observed on hydrothermal method synthesized composites than non-hydrothermal composite when added the same amount of precursors.

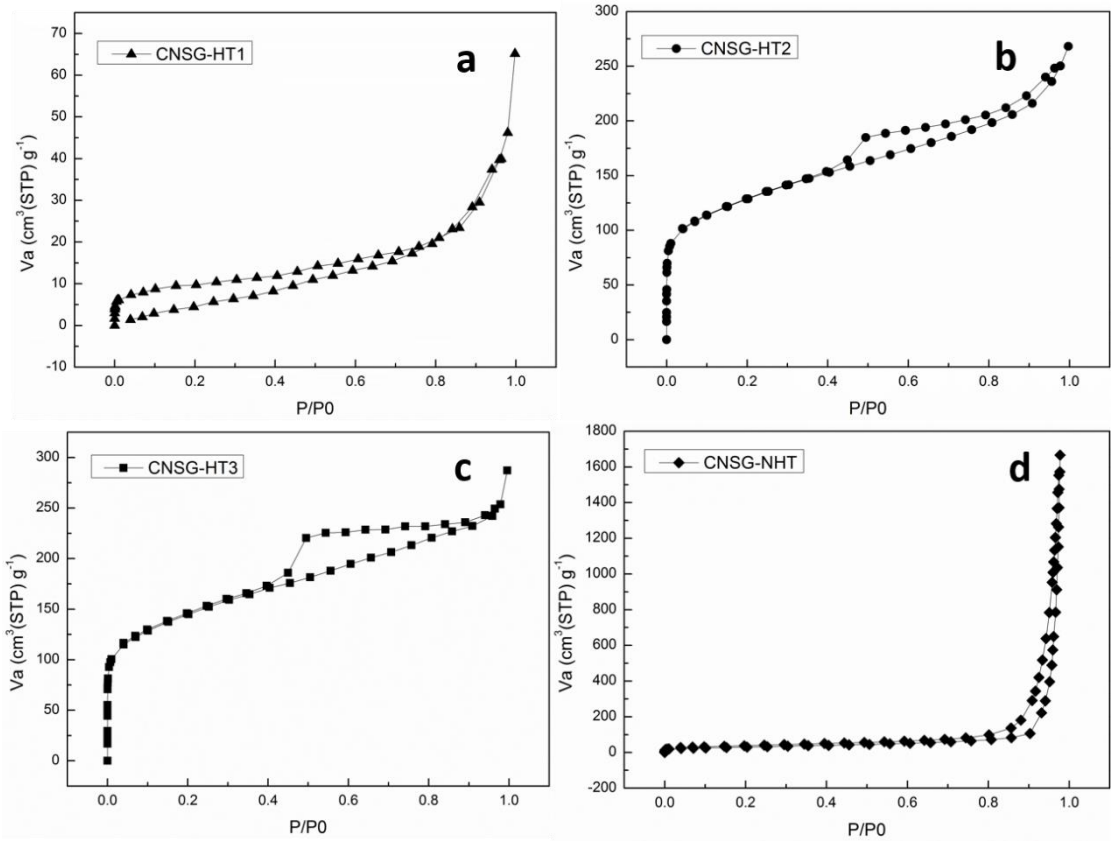

Figure 5.5. N_2 adsorption-desorption isotherms for (a) CNSG-HT1; (b) CNSG-HT2; (c) CNSG-HT3; and (d) CNSG-NHT.

The as-prepared CNSG composites were employed as the oxygen cathodes for Li-O_2 cells to test the electrochemical performance together with fresh Li metal foil as anode and 1 M LiTFSI

in tetraethylene glycol dimethyl ether (TEGDME) as electrolyte. The electrocatalytic activities of these oxygen cathodes were investigated with cyclic voltammetry (CV) study within 2.0 – 4.5 V at a scan rate of 0.1 mV s^{-1} (Figure 5.6a). Compared with other cathode materials, the Li-O_2 battery with CNSG-HT2 as cathode presents the largest cathodic current at a reduction peak around 2.5 V, and the highest ORR onset potential at the discharge direction, which demonstrates its superior ORR catalytic performance. Despite the large varieties of ORR performance, it is interesting to discover that the OER performance of those cathode materials shares more commons. Specifically, the OER onset potential for all samples are around 2.95 V, the oxidation peaks at around 3.2 V for CNSG-HT2 and CNSG-HT3 are slightly higher than those of CNSG-HT1 and CNSG-NHT. According to the ORR mechanism of Li-O_2 batteries, the results indicate that ORR is more sensitive to the structural change of cathode materials than OER. CNSG-HT2 composite possesses the best electrochemical activity towards both ORR and OER. Moreover, CNSG-HT2 also exhibits significant improvement towards both ORR and OER performance on CV tests with higher reduction peak potential and lower oxidation peak potential when compared with previous reported Co_9S_8 porous carbon cage and N, S co-doped graphene [18, 27]. The results indicate the interaction of Co_9S_8 and N, S co-doped graphene promotes catalytic performance towards ORR/OER. Li-O_2 cells using CNSG-NHT, CNSG-HT1, CNSG-HT2, and CNSG-HT3 as cathode were conducted the galvanostatic discharge-charge tests at a current density of 200 mA g^{-1}. To discover the effects on cobalt sulfide in these composites, nitrogen and sulphide co-doped graphene (NSG) was tested as a reference cathode material at the same condition. According to the XPS analysis, the nitrogen and sulphide contents in the composites are similar at about CNSG-HT2 (N: 3.13%, S: 1.58%), and NSG (N: 3.20%, S: 1.45%) respectively. The specific capacity of each cell was calculated based on the total mass of cathode materials. Figure 5.6b shows the first discharge-charge profiles of these batteries under O_2 condition. The discharge capacity of NSG is 391 mA h g^{-1}, while the cathodes with cobalt sulphide as composites show much higher specific capacity at 500 (CNSG-HT1), 1341 (CNSG-NHT), 1498 (CNSG-HT3), and 4887 (CNSG-HT2) mA h g^{-1}. Compare

with NSG, the presence of doped cobalt sulphide nanoparticles lead to an obvious increase in both the specific capacity and discharge potential plateau, indicating the superior ORR activity of CNSG composites. In addition, all CNSG cathodes achieve 100 % recovery for charge capacity, while only ~ 66% of the discharge capacity can be recovered for the Li-O_2 battery with NSG cathode. The results suggested a superior catalytic activity of CNSG composites towards OER. Among all the composites, CNSG-HT2 shows the best specific discharge-charge capacity. The inferior specific discharge capacity of CNSG-HT1 can be attributed to the low loading of Co_9S_8. However, though more cobalt sulphide precursor was loaded onto CSNG-HT3 and CSNG-NHT, inferior discharge capacity was observed for these cathodes. The specific capacity of Li-O_2 batteries is strongly dependent on the formation of Li_2O_2 through ORR process during discharge. As the main reactant, the adsorption of oxygen is one of the key factors to determine the formation of Li_2O_2. Dong and co-workers discovered that oxygen could be strongly adsorbed on the (111), (440), and (311) planes of Co_9S_8. Geometrically, (440) plane possess a fourford hollow site for O_2 adsorption, while (111) and (311) planes provide three and two Co^+ ions to be directly bonded with O_2 respectively [1]. Therefore, as discussed above, though more precursor was loaded on CNSG-HT3 composite, the XRD revealed less crystallinity of Co_9S_8 than that of CNSG-HT2, which results in an inferior O_2 adsorption ability and consequently a lower specific capacity of CNSG-HT3. Additionally, the structure of cathode material is an important factor to the performance difference among these cathode materials. Precisely, CNSG-HT2 presents much higher surface areas and pore volumes than CNSG-NHT does, which provide sufficient space to store discharge products and further to facilitate ORR and OER reactions in discharge and charge process. Moreover, with the size-reduced and homogeneously dispersed Co_9S_8 that synthesized through hydrothermal process, CNSG-HT2 enables more Co_9S_8 to be exposed to provide additional catalytic sites for ORR and OER reactions than CNSG-NHT does. All these structural and catalytic advantages make CNSG-HT2 exhibit highest discharge-charge capacity.

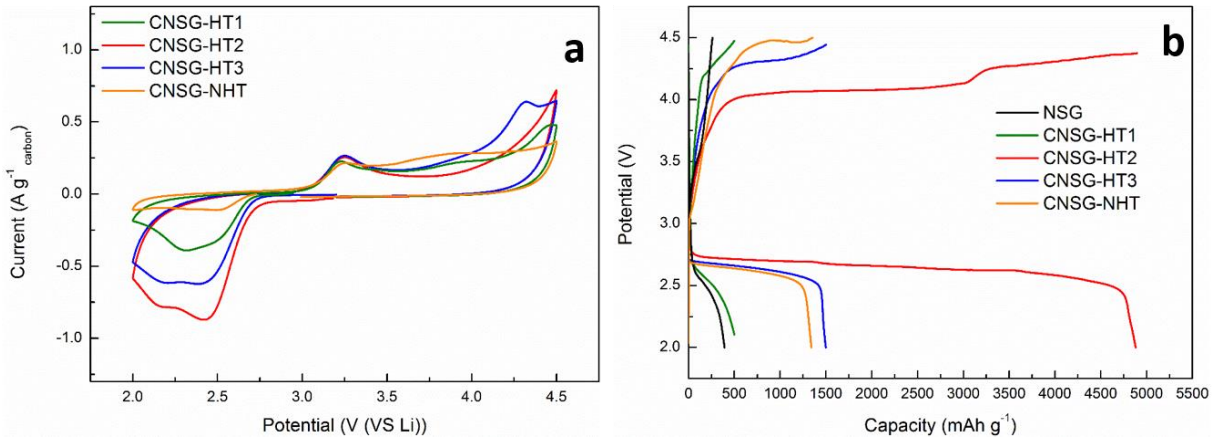

Figure 5.6. (a) CV curves of CNSG-HT1, CNSG-HT2, CNSG-HT3, and CNSG-NHT at a constant scan rate of 1 mV s^{-1}; (b) Discharge-charge curves of Li-O_2 batteries with CNSG-HT1, CNSG-HT2, CNSG-HT3, CNSG-NHT, and NSG at a current density of 200 mA g^{-1}.

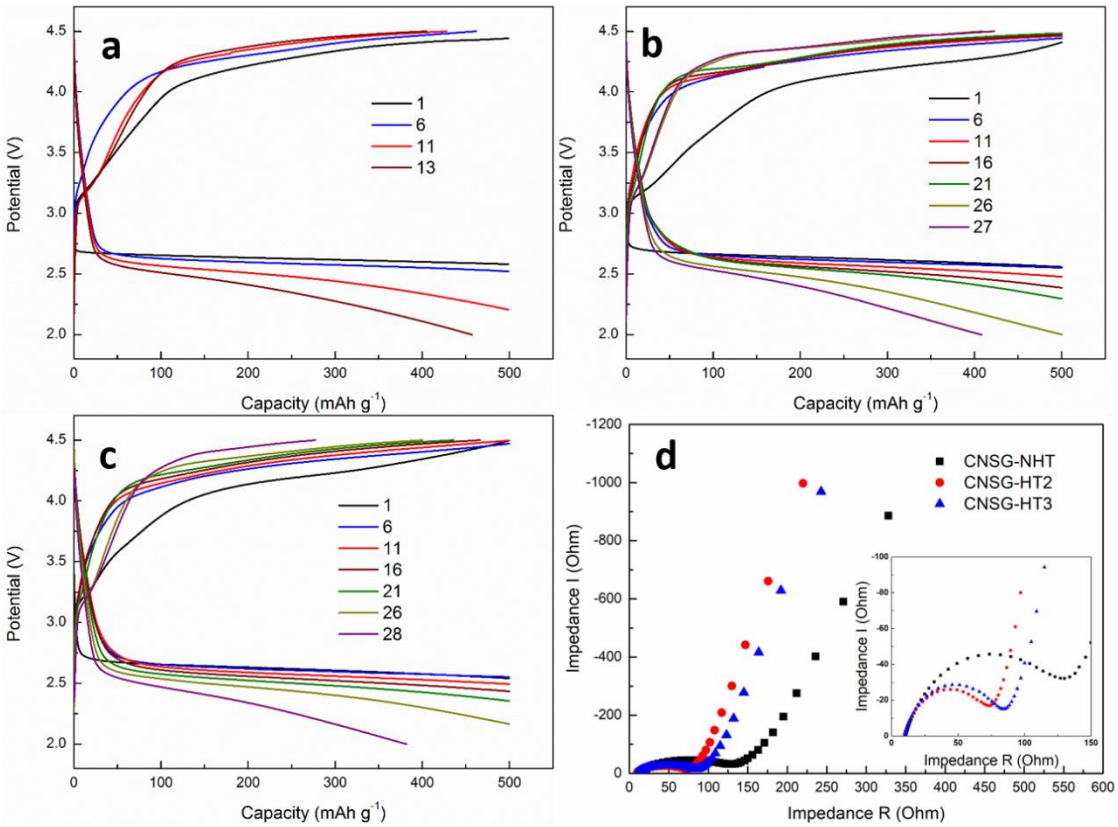

Figure 5.7. Cycling performance of Li-O_2 batteries with (a) CNSG-NHT, (b) CNSG-HT2, and (c) CNSG-HT3 as cathode materials at a controlled capacity of 500 mA h g^{-1}; (d) EIS plot of CNSG-NHT, CNSG-HT2, and CNSG-HT3.

Cycling performance of Li-O_2 batteries were tested with a current density at 200 mA g^{-1} and a cut-off capacity at 500 mA h g^{-1} to further investigate the stability and cycle ability of different cathode materials. As the discharge capacity of both NSG and CSNG-HT1 barely reached 500

mA h g^{-1}, only batteries with CNSG-NHT, CNSG-HT2 and CNSG-HT3 cathodes were tested, as shown in Figure 5.7a-c. Batteries with CNSG-HT2 as cathode can stay stable to the 27th cycles, which is approximately the same with CNSG-HT3 that stayed to 26th cycles. On the other hand, an obvious decay occurred to CNSG-NHT cathode with only 12 stable cycles can be achieved. In addition, the average overpotential of first cycle was calculated for each battery. The results agree with the cycling performance, that the overpential of CNSG-HT2 (1.57 V) and CNSG-HT3 (1.52 V) are lower than that of CNSG-NHT (1.66 V). Notably, the charge voltage platforms can be significantly decreased with the facilitation of the hydrothermal treated catalyst. In detail, the average discharge voltage platform for all the sample are roughly the same at 2.62 V, while the charge voltage platform of CNSG-HT2 (4.19 V) was found to be 90 mV lower than that of CNSG-NHT (4.28 V). The results indicate an inferior OER performance of CNSG-NHT than CNSG-HT2 and CNSG-HT3. The electrochemical impedance spectroscopy (EIS) was then employed for CNSG-HT2, CNSG-HT3, and CNSG-NHT to explore the conductivity and electrical transfer behaviour of these cathode materials. As shown in Figure 5.7d, the EIS curve of initial batteries with CNSG-NHT shows the highest impedance, while the CNSG-HT2 has the lowest impedance in Li-O_2 cells. The low impedance indicating a better conductivity and faster electrical charge transport in Li-O_2 cells, which plays an important role in determining the electrochemical mechanism of charging process, promotes the electrochemical performance and is much favourable for Li-O_2 systems. The cycle performance is largely associated with the decomposition of Li_2O_2 through OER during charge. The insufficient charge transfer caused by the electrical insulating Li_2O_2 hinders the fast decomposition of large particles of Li_2O_2 and results in the serious decay of Li-O_2 battery[28]. However, the introducing of Co^{3+} have been reported to induce Li vacancies through Co^{3+} doping in Li_2O_2 and further to increase the ionic and electronic conductivities of Li_2O_2 by 10 orders of magnitude (~ 10^{-9} S cm^{-1}) [29]. In addition, the strong oxygen affinity of Co_9S_8 can further promote the growth of defective form of $Li_{2-x}O_2$, which is more electronic conductive than crystalline Li_2O_2 [30]. As a result, the CNSG-HT2 composite can enhance the round-trip

efficiency of the Li–O_2 battery and provide a longer cycle life.

Conclusion

Various CNSG composites were successfully synthesized and used as the cathode materials in Li-O_2 systems. Through the electrochemical tests as well as the Li-O_2 batteries performance evaluation, best ORR and OER catalytic activity achieved when Co_9S_8 precursor amount was equal to the GO amount in hydrothermal treated composite, with a 100 % recoverable high discharge capacity at 4884 mA h g^{-1}, and stays for 27 cycles with a cut- off capacity at 500 mA h g^{-1}. The excellent batteries performance can be attributed to the homogeneous dispersed and well crystallized Co_9S_8 nanoparticles on N, S-GO sheet, which providing sufficient and constant active sites for both ORR and OER process. In addition, the high surface areas as well as pore volumes supplied by the composites enabled large space required for discharge products during long capacity discharge process. Therefore, we believe this CNSG composites strategy will open new opportunities to the development of various metal oxide/sulfide-carbon composite for various energy-related applications.

References

1. Lin, X.; Yuan, R.; Cai, S.; Jiang, Y.; Lei, J.; Liu, S.-G.; Wu, Q.-H.; Liao, H.-G.; Zheng, M.; Dong, Q., An Open-Structured Matrix as Oxygen Cathode with High Catalytic Activity and Large Li2O2 Accommodations for Lithium–Oxygen Batteries. *Advanced Energy Materials* **2018,** *8* (18), 1800089.
2. Mahmood, N.; Zhang, C. Z.; Jiang, J.; Liu, F.; Hou, Y. L., Multifunctional Co3S4/Graphene Composites for Lithium Ion Batteries and Oxygen Reduction Reaction. *Chemistry-a European Journal* **2013,** *19* (16), 5183-5190.
3. Wang, Y.; Wu, J.; Tang, Y.; Lü, X.; Yang, C.; Qin, M.; Huang, F.; Li, X.; Zhang, X., Phase-Controlled Synthesis of Cobalt Sulfides for Lithium Ion Batteries. *ACS Applied Materials & Interfaces* **2012,** *4* (8), 4246-4250.
4. Cao, F.; Zhao, M.; Yu, Y.; Chen, B.; Huang, Y.; Yang, J.; Cao, X.; Lu, Q.; Zhang, X.; Zhang, Z.; Tan, C.; Zhang, H., Synthesis of Two-Dimensional CoS1.097/Nitrogen-Doped Carbon Nanocomposites Using Metal–Organic Framework Nanosheets as Precursors for Supercapacitor Application. *J. Am. Chem. Soc.* **2016,** *138* (22), 6924-6927.

5. Li, R.; Dai, Y.; Chen, B.; Zou, J.; Jiang, B.; Fu, H., Nitrogen-doped Co/Co9S8/partly-graphitized carbon as durable catalysts for oxygen reduction in microbial fuel cells. *J. Power Sources* **2016,** *307*, 1-10.

6. Liu, X.; Liu, H.; Zhao, Y.; Dong, Y.; Fan, Q.; Kuang, Q., Synthesis of the Carbon-Coated Nanoparticle Co9S8 and Its Electrochemical Performance as an Anode Material for Sodium-Ion Batteries. *Langmuir* **2016,** *32* (48), 12593-12602.

7. Jiang, D.; Liang, H.; Liu, Y.; Zheng, Y.; Li, C.; Yang, W.; Barrow, C. J.; Liu, J., In situ generation of CoS1.097 nanoparticles on S/N co-doped graphene/carbonized foam for mechanically tough and flexible all solid-state supercapacitors. *Journal of Materials Chemistry A* **2018,** *6* (25), 11966-11977.

8. Jin, R.; Yang, L.; Li, G.; Chen, G., Hierarchical worm-like CoS2 composed of ultrathin nanosheets as an anode material for lithium-ion batteries. *Journal of Materials Chemistry A* **2015,** *3* (20), 10677-10680.

9. Liang, H.; Jiang, D.; Wei, S.; Cao, X.; Chen, T.; Huo, B.; Peng, Z.; Li, C.; Liu, J., 3D cellular CoS1.097/nitrogen doped graphene foam: a durable and self-supported bifunctional electrode for overall water splitting. *Journal of Materials Chemistry A* **2018,** *6* (33), 16235-16245.

10. Chen, B. L.; Li, R.; Ma, G. P.; Gou, X. L.; Zhu, Y. Q.; Xia, Y. D., Cobalt sulfide/N,S codoped porous carbon core-shell nanocomposites as superior bifunctional electrocatalysts for oxygen reduction and evolution reactions. *Nanoscale* **2015,** *7* (48), 20674-20684.

11. Han, J.; Guo, X.; Ito, Y.; Liu, P.; Hojo, D.; Aida, T.; Hirata, A.; Fujita, T.; Adschiri, T.; Zhou, H.; Chen, M., Effect of Chemical Doping on Cathodic Performance of Bicontinuous Nanoporous Graphene for Li-O2 Batteries. *Advanced Energy Materials* **2016,** *6* (3), 1501870.

12. Shu, C.; Li, B.; Zhang, B.; Su, D., Hierarchical Nitrogen-Doped Graphene/Carbon Nanotube Composite Cathode for Lithium–Oxygen Batteries. *ChemSusChem* **2015,** *8* (23), 3973-3976.

13. Zhao, C.; Yu, C.; Liu, S.; Yang, J.; Fan, X.; Huang, H.; Qiu, J., 3D Porous N-Doped Graphene Frameworks Made of Interconnected Nanocages for Ultrahigh-Rate and Long-Life Li-O2Batteries. *Adv. Funct. Mater.* **2015,** *25* (44), 6913-6920.

14. Dou, S.; Tao, L.; Huo, J.; Wang, S. Y.; Dai, L. M., Etched and doped Co9S8/graphene hybrid for oxygen electrocatalysis. *Energy Environ. Sci.* **2016,** *9* (4), 1320-1326.

15. Ganesan, P.; Prabu, M.; Sanetuntikul, J.; Shanmugam, S., Cobalt Sulfide Nanoparticles Grown on Nitrogen and Sulfur Codoped Graphene Oxide: An Efficient Electrocatalyst for Oxygen Reduction and Evolution Reactions. *ACS Catalysis* **2015,** *5* (6), 3625-3637.

16. Chen, Z.; Wang, J.; Chao, D.; Baikie, T.; Bai, L.; Chen, S.; Zhao, Y.; Sum, T. C.; Lin, J.; Shen, Z., Hierarchical Porous LiNi1/3Co1/3Mn1/3O2 Nano-/Micro Spherical Cathode

Material: Minimized Cation Mixing and Improved Li+ Mobility for Enhanced Electrochemical Performance. *Scientific Reports* **2016,** *6*, 25771.

17. Li, S.; Peng, S.; Huang, L.; Cui, X.; Al-Enizi, A. M.; Zheng, G., Carbon-Coated Co3+-Rich Cobalt Selenide Derived from ZIF-67 for Efficient Electrochemical Water Oxidation. *ACS Applied Materials & Interfaces* **2016,** *8* (32), 20534-20539.

18. Dou, Y.; Lian, R.; Zhang, Y.; Zhao, Y.; Chen, G.; Wei, Y.; Peng, Z., Co9S8@carbon porous nanocages derived from a metal–organic framework: a highly efficient bifunctional catalyst for aprotic Li–O2 batteries. *Journal of Materials Chemistry A* **2018,** *6* (18), 8595-8603.

19. Peng, S. J.; Han, X. P.; Li, L. L.; Zhu, Z. Q.; Cheng, F. Y.; Srinivansan, M.; Adams, S.; Ramakrishna, S., Unique Cobalt Sulfide/Reduced Graphene Oxide Composite as an Anode for Sodium-Ion Batteries with Superior Rate Capability and Long Cycling Stability. *Small* **2016,** *12* (10), 1359-1368.

20. Jia, N.; Liu, J.; Gao, Y.; Chen, P.; Chen, X.; An, Z.; Li, X.; Chen, Y., Graphene-Encapsulated Co9S8 Nanoparticles on N,S-Codoped Carbon Nanotubes: An Efficient Bifunctional Oxygen Electrocatalyst. *ChemSusChem* **2019,** *12* (14), 3390-3400.

21. Zhang, S.; Li, D.; Chen, S.; Yang, X.; Zhao, X.; Zhao, Q.; Komarneni, S.; Yang, D., Highly stable supercapacitors with MOF-derived Co9S8/carbon electrodes for high rate electrochemical energy storage. *Journal of Materials Chemistry A* **2017,** *5* (24), 12453-12461.

22. Wu, Y.; Zhu, C.; Shu, L.; Duan, J.; Wei, D.; Xu, J.; Zhu, Z.; Li, L.; Peng, Z.; Chen, Z., Co9S8 confined in bifunctional N/S co-doped carbon/carbon with high electrochemical performance for lithium-ion batteries. *Appl. Surf. Sci.* **2019,** *489*, 528-537.

23. Wang, Z. L.; Xu, D.; Xu, J. J.; Zhang, L. L.; Zhang, X. B., Graphene Oxide Gel-Derived, Free-Standing, Hierarchically Porous Carbon for High-Capacity and High-Rate Rechargeable Li-O2 Batteries. *Adv. Funct. Mater.* **2012,** *22* (17), 3699-3705.

24. Wang, D.-W.; Li, F.; Liu, M.; Lu, G. Q.; Cheng, H.-M., 3D Aperiodic Hierarchical Porous Graphitic Carbon Material for High-Rate Electrochemical Capacitive Energy Storage. *Angew. Chem. Int. Ed.* **2008,** *47* (2), 373-376.

25. Li, B.; Yang, X.; Xia, L.; Majeed, M. I.; Tan, B., Hollow Microporous Organic Capsules. **2013,** *3*, 2128.

26. Alothman, Z., *A Review: Fundamental Aspects of Silicate Mesoporous Materials*. **2012**; Vol. 5, p 2874-2902.

27. Kim, J.-H.; Kannan, A. G.; Woo, H.-S.; Jin, D.-G.; Kim, W.; Ryu, K.; Kim, D.-W., A bi-functional metal-free catalyst composed of dual-doped graphene and mesoporous carbon for rechargeable lithium–oxygen batteries. *Journal of Materials Chemistry A* **2015,** *3* (36), 18456-18465.

28. Wang, J.; Zhang, Y.; Guo, L.; Wang, E.; Peng, Z., Identifying Reactive Sites and

Transport Limitations of Oxygen Reactions in Aprotic Lithium-O2 Batteries at the Stage of Sudden Death. *Angew. Chem. Int. Ed.* **2016,** *55* (17), 5201-5205.

29. Radin, M. D.; Monroe, C. W.; Siegel, D. J., How Dopants Can Enhance Charge Transport in Li2O2. *Chem. Mater.* **2015,** *27* (3), 839-847.

30. Lim, H. D.; Lee, B.; Bae, Y.; Park, H.; Ko, Y.; Kim, H.; Kim, J.; Kang, K., Reaction chemistry in rechargeable Li-O-2 batteries. *Chem. Soc. Rev.* **2017,** *46* (10), 2873-2888.

Supporting Information

Development of Co_9S_8 Hybridised N, S-GO Nanosheets as High-Performance Cathodes for Li-O_2 Batteries

Qi Bi,† Heng Wang,† Haihui Wang,*†‡ and Sheng Dai*†§

† School of Chemical Engineering and Advanced Materials, The Univeristy of Adelaide, South Australia 5005, Australia

‡ School of Chemistry & Chemical Engineering, South China University of Technology, 381 Wushan Road, Guangzhou 510640, China

§ Department of Chemical Engineering, Brunel University London, Uxbridge, UB8 3PH, United Kingdom

Corresponding authors

*E-mail: hhwang@scut.edu.cn; s.dai@adelaide.edu.au

Synthesis of graphene oxide. Graphite flakes were prepared using an improved Hummer's method. 3 g natural graphite flakes were added into a mixture of concentrated H_2SO_4 and H_3PO_4 (360:40 mL), followed by the addition of 18 g $KMnO_4$. The mixture was heated and stirred at 50 °C for 12 h. After cooling down to room temperature, it was poured into 400 ml ice-water with addition of H_2O_2 (30 %, 10 mL). The mixture was then filtered over a 0.45 µm PTFE membrane and washed with 200 ml of 30 % HCl and 1 L water to obtain graphite oxide. Exfoliation of the above prepared graphite oxide was achieved by ultrasonication of the diluted graphite oxide dispersion for 30 min, followed by freeze drying the above solution to achieve graphene oxide (GO) powder.

Synthesis of cobalt thiourea complex ($Co(TU)_4(NO_3)_2$): Cobalt nitrate ($Co(NO_3)_2 \cdot 6H_2O$, 0.01 M) was dissolved in 25 mL of hot butanol. Thiourea (0.04 M) was added, and the mixture was heated to reach boiling until all solids being dissolved, as indicated by the solution colour change from red to blue. On cooling, a blue solid of $Co(TU)_4(NO_3)_2$ was separated out. The cobalt thiourea complex was collected by suction filtered, washed with diethyl ether and dried of the blue solids under vacuum at 30 °C.

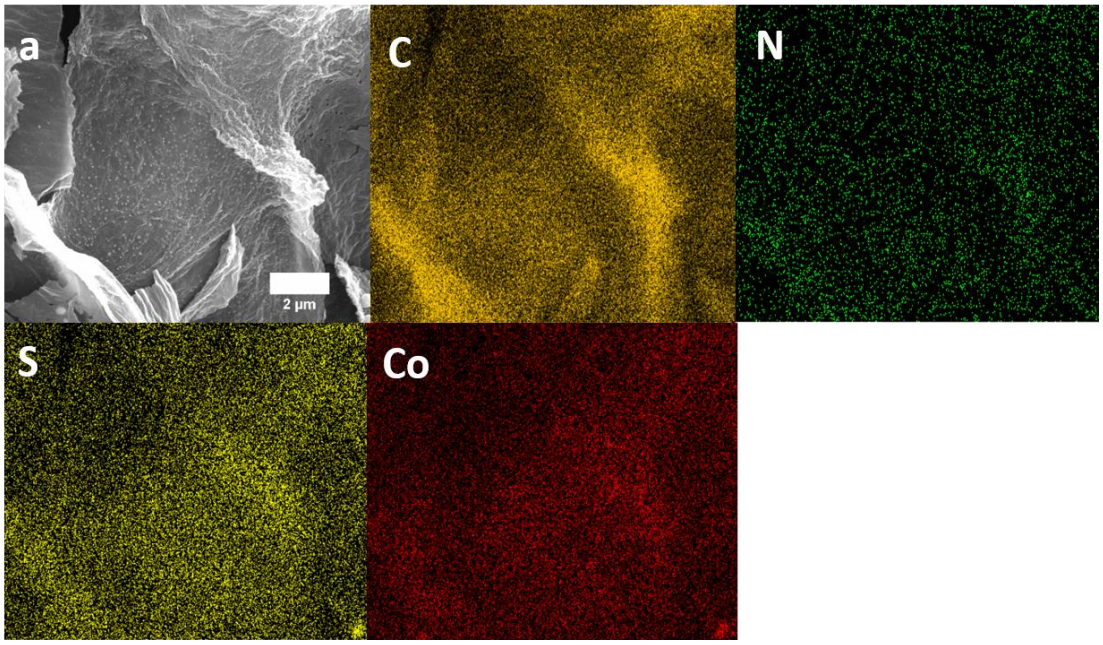

Figure 5.S1. The SEM image and corresponding EDX maps of CNSG-HT2.

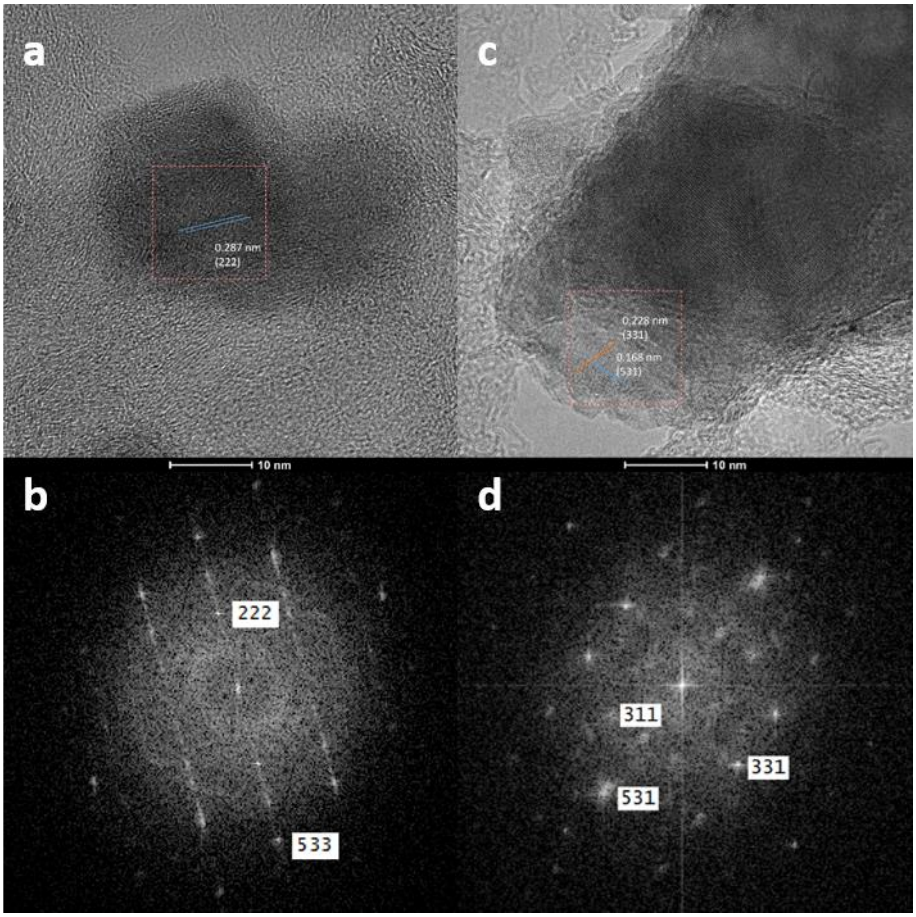

Figure 5.S2. (a) HRTEM image and (b) Fast Fourier transform (FFT) of Co_9S_8 nanoparticle CNSG-HT3; (c) HRTEM image and (d) Fast Fourier transform (FFT) of Co_9S_8 particle on CNSG-HT1.

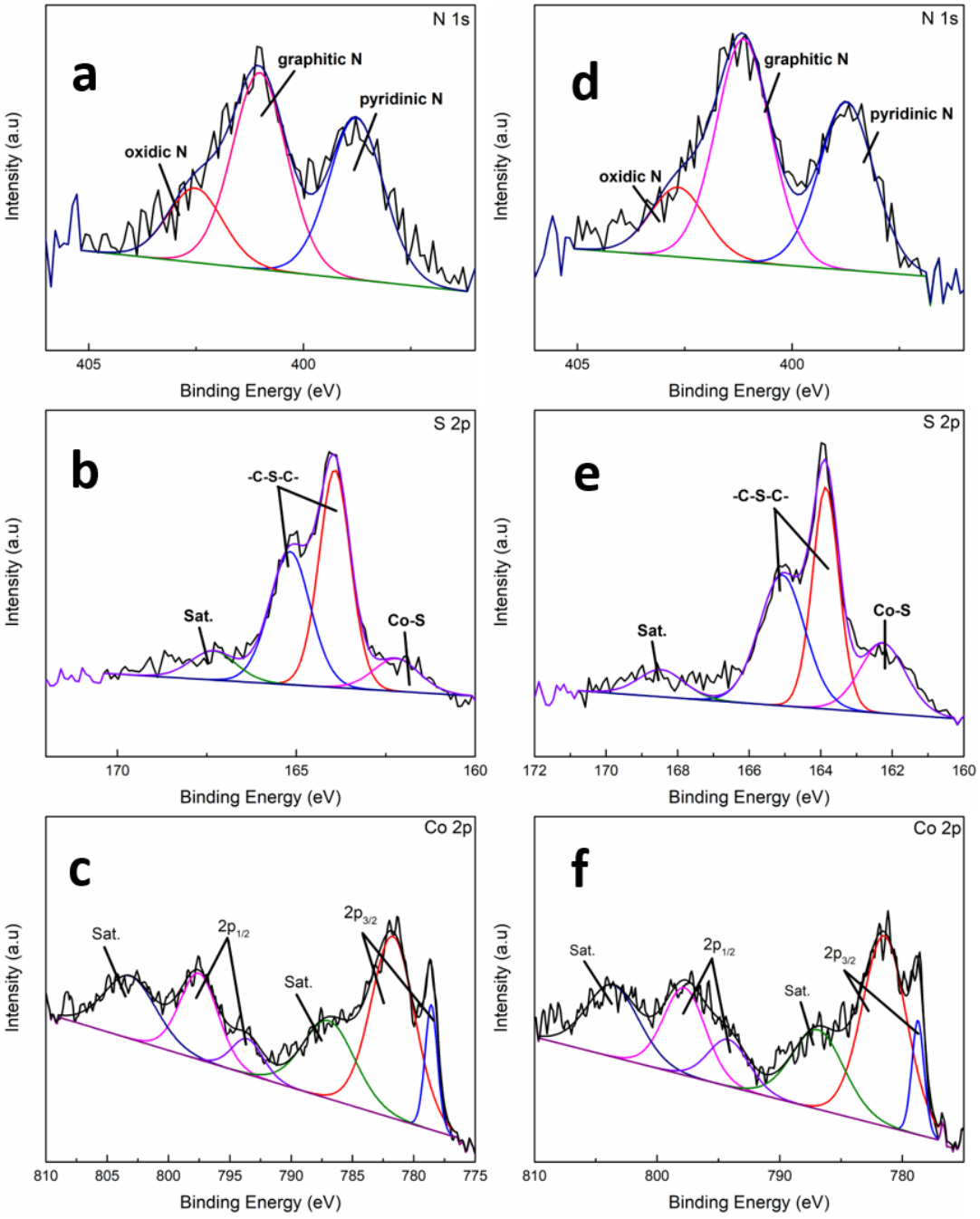

Figure 5.S3. XPS spectra of (a) N 1s, (b) S 2p, and (d) Co 2p of CNSG-HT2 and (d) N 1s, (e) S 2p, and (f) Co 2p of CNSG-HT1.

Chapter 6 Conclusion and Recommendation

6.1 Conclusion

This thesis aims to explore stable bi-functional electrocatalysts towards ORR/OER as the oxygen electrodes to achieve high-performance non-aqueous Li-O_2 batteries. Through the investigation on electrochemical performance of Li-O_2 batteries regarding to porous structures of carbon materials, heteroatom doped graphene, dual-phased cobalt sulfides, and cobalt sulfide/N, S doped graphene composites, the following conclusions can be drawn:

(a) A high discharge specific capacity of 16777 mA h g^{-1} with an efficiency of 94.6 % was achieved from the N-rGO with 170 nm porous structure (N-rGO/170) due to its specific pore structures and large surface areas. The N-rGO/170 electrode also demonstrated superior cycle stability than other electrode materials with up to 34 cycles at a cut-off capacity of 500 mA h g^{-1} and 25 cycles at 1000 mA h g^{-1}. The results proved that porous structures on oxygen electrode plays an important role on improving electrochemical performance of Li-O_2 batteries by providing sufficient space for discharge products and increasing the exposure of active sites of catalysts. The low cycling capability was attributed to the serious distortion of electrode materials and presence of large amount irreversible discharge products on electrode surfaces.

(b) Cobalt sulfides are effective ORR/OER catalysts for Li-O_2 batteries. A dual-phase cobalt sulfide contained CoS and Co_9S_8 (CoS-900) was mixed with N-rGO to be employed as oxygen cathodes and significantly improved electrochemical performance of resulting Li-O_2 battery by promoting the generation of both crystalline and amorphous film-like Li_2O_2. As a result, the designed N-rGO/CoS-900 cathode achieved large discharge capacity at 7410 mA h g^{-1} with 100 % charge capacity recovery as well as a super long cycle life at 108 cycles in Li-O_2 system. To the best of our knowledge, this work for the first time investigated the phase impact of cobalt sulfides in Li-O_2

battery to provide a new perspective for the development of ORR/OER catalyst for Li-O_2 batteries.

(c) Co_9S_8/N, S-GO composites were synthesized via hydrothermal treatment and further optimized by adjusting the loading of Co_9S_8 precursors before being applied as oxygen electrodes for Li-O_2 batteries. The best ORR and OER catalytic activity achieved when the precursor amount was equal to the rGO amount in hydrothermal treated composite, with a 100 % recoverable high discharge capacity at 4884 mA h g^{-1}, and stays for 27 cycles with a cut- off capacity at 500 mA h g^{-1}. The homogeneous dispersed and well crystallized Co_9S_8 nanoparticles provided sufficient and constant active sites for both ORR and OER process to improve battery performance. In addition, high surface areas as well as pore volumes supplied by the leave-like composites enabled the large space required for discharge products during long capacity discharge process.

6.2 Future Recommendation

As one of the promising next generation energy storage systems, the practical implementation of Li-O_2 battery is hindered by many challenges, including inactive cathode materials and instable electrolytes. In this thesis, we have systematically investigated the effects of porous structure on carbon-based cathode materials and explored the approaches to employ cobalt sulfides as efficient catalysts either in the form of nanoparticles or composites for Li-O_2 batteries. The following research aspects can be further explored in the future.

Graphene is widely applied as cathode materials due to its light weight, high conductivity and unique structure that can benefit the operation of Li-O_2 batteries. Recently, phosphorene was developed to have similar single layer structure, and was compared intensively with graphene. Phosphorene is recommended as a promising alternative to graphene, and have been employed in different energy storage systems, such as Li-ion[1], Li-S[2]and Sodium-ion batteries[3]. Therefore, future works can focus on exploring the application of phosphorene in Li-O_2 batteries to replace graphene and achieve better battery performance.

Furthermore, the degradation of electrolyte is one of the main factors to hinder the application of Li-O_2 batteries. Ionic liquids (ILs) have been intensively investigated as electrolytic media in Li-O_2 batteries due to their advanced properties, including negligibly low vapour pressure, non-flammability, low toxicity, stable chemical property and comparable large electrochemical windows. According to previous studies, we have chosen several ionic liquids as the electrolytes for Li-O_2 systems for further investigation, they are PYR_{14}TFSI, PYR_{14}FSI, DEMEFSI, DEMETFSI, $PYR_{1(201)}$TFSI, $PYR_{1(201)}$FSI, $P_{222(201)}$TFSI, and $P_{222(201)}$FSI. The performance of these ILs as electrolytes can be studied in three approaches, namely, the performance of single IL, mixed IL and the mixture of IL and ethers in Li-O_2 batteries. Hopefully, the development of ILs can bring a more stable system for Li-O_2 system, and accelerate the practical application of Li-O_2 batteries.

References

1. Li, W.; Yang, Y.; Zhang, G.; Zhang, Y.-W., Ultrafast and directional diffusion of lithium in phosphorene for high-performance lithium-ion battery. Nano Lett. 2015, 15 (3), 1691.
2. Li, F.; Zhao, J., Atomic Sulfur Anchored on Silicene, Phosphorene, and Borophene for Excellent Cycle Performance of Li-S Batteries. ACS applied materials & interfaces 2017, 9 (49), 42836.
3. Sun, J.; Lee, H.-W.; Pasta, M.; Yuan, H.; Zheng, G.; Sun, Y.; Li, Y.; Cui, Y., A phosphorene-graphene hybrid material as a high-capacity anode for sodium-ion batteries. Nature nanotechnology 2015, 10 (11), 980.